ABSTRACT

THE ROLE OF SEMAPHORINS IN RESPONSE TO INJURY IN *C. ELEGANS* NEURONS

by
Maria Belen Harreguy Alfonso

When neural tissue is injured by trauma, delicate neuronal processes such as axons and dendrites are prone to lesion damage and often disconnect. The molecular, cellular, and circuit mechanisms that underlie the regrowth and reconnection of these processes and the recovery of behavior are major challenges in the fields of neuroscience, regeneration, and resilience. At the molecular and cellular levels, signaling pathways that mediate neuronal growth cone guidance during development can play a role in neuronal regeneration and recovery from injury. One family of signaling proteins involved in this process comprises the highly conserved semaphorins and their receptors, the plexins. Across various species, from *C. elegans* to humans, semaphorins and plexins are crucial for axon pathfinding and synapse formation during development.

In the mammalian nervous system, the semaphorin signaling system is comprised of more than 20 semaphorins and 9 plexins, whereas the *C. elegans* genome only encodes 3 semaphorins and 2 plexin receptors. Among them, the transmembrane semaphorins, SMP-1 and SMP-2, signal through their receptor PLX-1, while the secreted semaphorin MAB-20, signals through PLX-2.

This dissertation explores the role of semaphorin signaling in neuroregeneration *in vivo*, by making use of the experimental advantages of *Caenorhabditis elegans*. Importantly, this versatile model animal has the natural ability to regenerate neuronal processes after injury and optic methods were developed to precisely disconnect single

neurites in otherwise intact animals using laser microsurgery. Moreover, the semaphorin system is relatively simple and genetically amenable, and transgenic, microscopy and behavior analysis methods are well established.

The development and assessment of a new laser microsurgery system as part of this thesis allowed reliable and accurate disconnection of identifiable axons and dendrites. The elucidated expression patterns and involvement of *C. elegans* semaphorins in neural regeneration have shed significant light with regard to the role this pathway plays in *C. elegans* regeneration and added to the field of knowledge of neural regeneration research.

The findings reveal that regrowth and reconnection are more prevalent in the absence of both plexin receptors and the secreted semaphorin MAB-20. This suggests that the semaphorin signaling in this system restricts neural growth, possibly to prevent aberrant reconnection. The membrane-bound SMP-1 and SMP-2 might have a redundant role, signaling through PLX-1. These results align with the inhibitory effects of semaphorin signaling on axonal growth and guidance during development in the mammalian system. Therefore, secreted and membrane-bound semaphorin signaling pathways restrict regeneration using distinct processes, likely involving spatial specificity and recurrent signals.

Findings such as the ones presented in this thesis delve deeper into the mechanisms and factors involved in promoting regeneration and aid to uncover valuable insights that could assist in overcoming the challenges faced by regenerative medicine in treating central nervous system injuries and disorders.

THE ROLE OF SEMAPHORINS IN RESPONSE TO INJURY IN *C. ELEGANS* NEURONS

by
Maria Belen Harreguy Alfonso

A Dissertation
Submitted to the Faculty of
New Jersey Institute of Technology
And Rutgers, The State University of New Jersey, Newark
in Partial Fulfillment of the Requirements for the Degree of
Doctor of Philosophy in Biology

Department of Biological Sciences

December 2023

APPROVAL PAGE

THE ROLE OF SEMAPHORINS IN RESPONSE TO INJURY IN *C. ELEGANS* NEURONS

Maria Belen Harreguy Alfonso

Dr. Farzan Nadim, Dissertation Co-Advisor Date
Professor and Chair, Department of Biological Sciences, NJIT

Dr. Gal Haspel, Dissertation Co-Advisor Date
Assistant Professor, Department of Biological Sciences, NJIT

Dr. Wilma Friedman, Committee Member Date
Professor and Chair, Department of Biological Sciences,
Rutgers University, Newark, NJ

Dr. Tracy Tran, Committee Member Date
Professor, Department of Biological Sciences, Rutgers University, Newark, NJ

Dr. Jennifer Morgan, Committee Member Date
Senior Scientist and Director, Bell Center,
Marine Biological Laboratory, Woods Hole, MA

BIOGRAPHICAL SKETCH

Author: Maria Belen Harreguy Alfonso

Degree: Doctor of Philosophy

Date: December 2023

Undergraduate and Graduate Education:

- Doctor of Philosophy in Biological Sciences,
  New Jersey Institute of Technology, Newark, NJ, 2023

- Master of Science in Biotechnology,
  University of South Florida, Tampa, FL, 2016

- Bachelor of Science in Biotechnology,
  Universidad ORT Uruguay, Montevideo, Uruguay, 2014

Major: Biological Sciences

Publications:

Harreguy, M. B., Tanvir, Z., Shah, E., Simprevil, B., Tran, T. S., & Haspel, G. (2022). Semaphorin signaling restricts neuronal regeneration in C. elegans. Frontiers in Cell and Developmental Biology, 10, 814160.

Harreguy, M. B., Tran, T. S., & Haspel, G. (2022). Neuronal microsurgery with an Yb-doped fiber femtosecond laser. In *C. elegans*: Methods and Applications (pp. 319-328). New York, NY: Springer US.

Gershman, S., Harreguy, M. B., Yatom, S., Raitses, Y., Efthimion, P., & Haspel, G. (2021). A low power flexible dielectric barrier discharge disinfects surfaces and improves the action of hydrogen peroxide. Scientific Reports, 11(1), 1-12.

Harreguy, M. B., Marfil, V., Grooms, N. W. F., Gabel, C. V., Chung, S. H., & Haspel, G. (2020). Ytterbium-doped fibre femtosecond laser offers robust operation with deep and precise microsurgery of *C. elegans* neurons. Scientific Reports, 10(1), 4545.

Haspel, G., Deng, L., Harreguy, M. B., & Tanvir, Z. (2020). Elegantly. In the Neural Control of Movement (pp. 3-29). Cambridge, Massachusetts: Academic Press.

Pagotto, R., Santamaría, C. G., Harreguy, M. B., Abud, J., Zenclussen, M. L., Kass, L., ... & Bollati-Fogolín, M. (2020). Perinatal exposure to Bisphenol A disturbs the early differentiation of male germ cells. Reproductive Toxicology, 98, 117-124.

Santamaria, N., Alhothali, M., Alfonso, M. H., Breydo, L., & Uversky, V. N. (2017). Intrinsic disorder in proteins involved in amyotrophic lateral sclerosis. Cellular and Molecular Life Sciences, 74, 1297-1318.

Porro, V., Pagotto, R., Harreguy, M. B., Ramírez, S., Crispo, M., Santamaría, C., ... & Bollati-Fogolín, M. (2015). Characterization of Oct4-GFP transgenic mice as a model to study the effect of environmental estrogens on the maturation of male germ cells by using flow cytometry. The Journal of Steroid Biochemistry and Molecular Biology, 154, 53-61.

Presentations:

Harreguy, M.B., Tanvir Z., Shah E., Simprevil B., Mohammad A., Shah N., Syed S., Tran T.S., Haspel, G. (2023). Semaphorin signaling pathway restricts neuronal regeneration. [Poster], International *C. elegans* conference, Glasgow, Scotland.

Harreguy, M.B., Tanvir Z., Shah E., Simprevil B., Mohammad A., Shah N., Syed S., Tran T.S., Haspel, G. (2022). *Elegant Signaling: two plexins and 3 semaphorins guide neuronal regeneration in C. elegans.* [Poster], Motor Control Symposium (Salk Institute), San Diego, CA.

Harreguy, M.B., Tanvir Z., Shah E., Simprevil B., Mohammad A., Shah N., Syed S., Tran T.S., Haspel, G. (2022). *Elegant Signaling: two plexins and 3 semaphorins guide neuronal regeneration in C. elegans.* [Poster], Society for Neuroscience meeting, San Diego, CA.

Harreguy, M. B., Tanvir, Z., Shah, E., Simprevil, B., Tran, T. S., & Haspel, G. (2022). *Semaphorin signaling restricts neuronal regeneration in C. elegans.*[Oral presentation], CeNeuro, University of Vienna, Vienna, Austria.

Haspel G., Harreguy M. B., Gershman S. (2022). *Cold atmospheric plasma for neural regeneration.* [Poster], American Physical Society Meeting, Chicago, IL.

Harreguy, M. B., Tran, T. S., & Haspel, G. (2019*). Semaphorin signaling in neuronal regeneration in C. elegans.* [Oral presentation], 8th Annual Small Circuits and behavior meeting, Perelman School of Medicine, University of Pennsylvania. Philadelphia, PA.

“Families are the compass that guides us. They are the inspiration to reach great heights, and our comfort when we occasionally falter.” – Brad Henry

This dissertation is dedicated to my parents Sebastian and Tesy, my grandparents Guillermo, Angeles, Oscar and Teresita, my brother Sebastian, my husband Geoff, and my dogs Loki and Emma.

ACKNOWLEDGMENTS

I thank my Dissertation Advisor, Dr. Gal Haspel, for his dedicated support and mentorship throughout this process. I would also like to thank Dr. Farzan Nadim for his support, help, and input as a co-advisor, Department Chair, and Committee member.

I thank my committee members – Dr. Wilma Friedman, Dr. Tracy Tran, and Dr. Jennifer Morgan – for their guidance and very helpful insight in navigating the path towards graduation.

A huge thank you is due to the NJIT Biology administrators Karen Roach and Sherri Brown for their help with registration, purchasing, great conversations, and the many other issues they helped me resolve throughout my time at NJIT.

I would also like to thank the funding sources, the National Institutes of Health R15 Grant (award 1R15NS125565-01) and NJ Spinal Cord Grant (award CSCR14ERG002) for the research funding. In addition, I would like to thank the NJIT Department of Biological Sciences and the Rutgers Newark Department of Biological Sciences for their financial support, which made this work possible.

I thank my many mentors throughout the years especially the Cell Biology Unit lab members at Institut Pasteur Montevideo, as well as our collaborators and anyone who was kind enough to share their expertise, reagents, and time with me. Haspel Lab members: Zainab Tanvir, Dr. Lan Deng, Dr. Vanessa Marfil, Shareef Syed, Blandine Simprevil, Esha Shah, Naomi Shah, Natalie Ableson, Ishani Patel, Marcella Viola, and Ayman Mohammed. Tran Lab members: Dr. Victor Danelon, Dr. Edward Martinez, Dr. Oday Abushalbaq, Joan Baek, and Dr. Carol Eisenberg.

I would also like to thank the entire group of Central King Building graduate students and postdocs (Christine, Katie, Omar, Will, Smita, Neel, Grant, Jon, Nelly, Haley, and many more) for all the support, good times, and great conversations we shared throughout the last 6 years.

Finally, I would like to thank my amazing family. All I have achieved is due to their endless support and love; to my parents (Sebastian and Tesy) and my brother (Sebi) thanks a million for giving me absolutely everything I needed to succeed. Geoff: thanks for your support and love during this journey. Last but not least, thank you to my canine family members, Emma and Loki for their company and endless emotional support.

TABLE OF CONTENTS

Chapter **Page**

TABLE OF CONTENTS
(Continued)

Chapter

TABLE OF CONTENTS
(Continued)

TABLE OF CONTENTS
(Continued)

Chapter **Page**

TABLE OF CONTENTS
(Continued)

Chapter **Page**

LIST OF FIGURES

LIST OF FIGURES
(Continued)

CHAPTER 1

INTRODUCTION

1.1 Regeneration in the Nervous System

Santiago Ramon y Cajal, the ‘father of neuroscience,’ described in 1930 one of the most significant challenges of regenerative medicine: failure of central fibers to regrow "*derives from external conditions, the presence or absence of auxiliary factors that are indispensable to the regenerative process*" (Ramon y Cajal, 1930). From his work and observations (Figure 1.1), it was clear to him then that the peripheral nervous system (PNS) does have some regenerative abilities (Kang & Lichtman, 2013), while neurons in the central nervous system (CNS) seldom regenerate after injury.

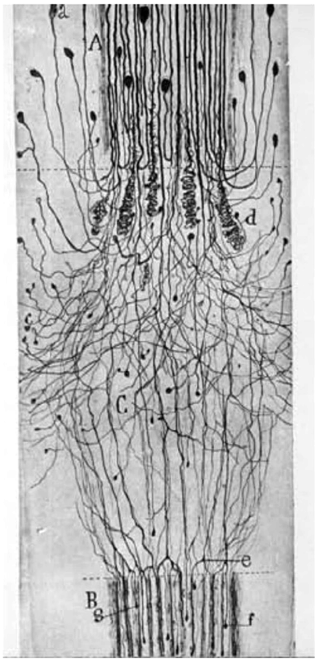

Figure 1.1 Regenerating cat peripheral nerve after sectioning as drawn by Santiago Ramon y Cajal.
Source (Ramon y Cajal, 1930)

Further, axons in the CNS of "lower" vertebrates, such as fish or lampreys, have the ability to regenerate their optic nerves and spinal cords (Ghosh & Hui, 2018; Oliphint et al., 2010; Stone et al., 2022). However, this is not the case in the adult mammalian CNS, resulting in permanent disconnection and loss of function after injury. Therefore, understanding the fundamental mechanisms that impede regeneration in the adult mammalian CNS is central to understanding its response to injury and vital for developing strategies to promote the recovery of circuit connectivity and function.

In the process of neurodevelopment, both CNS and PNS neurons grow and extend their axons and dendrites under the influence of axon guidance cues and growth factors. These factors, however, are only present in small amounts in adults (Giger et al., 2010). This inspired an approach that aims to recreate the growth-permissive environment of the developing CNS to promote recovery after injury (Hilton & Bradke, 2017; Huebner & Strittmatter, 2009). These permissive factors include Semaphorins, Netrins, Ephrins, and Slits, together with their receptors (Giger et al., 2010). In this dissertation, I will focus on Semaphorins and their role in neurite regeneration.

1.2 The Semaphorins

1.2.1 Semaphorins and their receptors

The first semaphorin was discovered in 1992 in the grasshopper embryo and was initially named Fasciclin IV, this protein was found to be expressed in axons and muscle of the developing limb bud and to play a role in axonal growth cone guidance (Kolodkin et al., 1992). Soon after, the same research group identified three proteins similar to Fasciclin IV in structure and function, a transmembrane and a secreted protein in *Drosophila*

Melanogaster as well as a similar protein in humans (Kolodkin et al., 1993). Around the same time, a secreted protein with very similar DNA regions and structural components was found in chicks. This protein, capable of producing growth cone collapse in dorsal root ganglion cells (DRGs) *in vitro*, was named Collapsin (Luo et al., 1993). Due to their similarity in structure and function, these proteins were named semaphorins to denote their function as semaphores (signals) for growing axons (Goodman et al., 1999; Kolodkin et al., 1993).

Semaphorins are glycosylated proteins that can be either secreted or transmembrane. The hallmark feature of these proteins, conserved among all family members, is the 500 residue-long N-terminal domain, known as the Sema domain. It has several blocks of conserved amino acids and is characterized by highly conserved cysteine residues. This domain facilitates homodimerization between semaphorins and serves as the binding site for their receptors (Alto & Terman, 2017; Yazdani & Terman, 2006). There are eight classes of semaphorins, categorized from 1-7, and a V class which is only present in viruses. While classes 1 and 2 are exclusive to invertebrates, classes 3 to 7 are present only in vertebrates except for class 5 semaphorins which have also been identified in the fruit fly *Drosophila Melanogaster* (Alto & Terman, 2017; Yazdani & Terman, 2006).

The first semaphorin receptors discovered were the Neuropilins, a family of receptors for class 3 semaphorins (He & Tessier-Lavigne, 1997; Kolodkin et al., 1997). Two Neuropilins have been identified, Neuropilin 1 and Neuropilin 2, some class 3 semaphorins can bind exclusively to only one of these proteins, but some others are able to bind to both (H. Chen et al., 1997; He & Tessier-Lavigne, 1997; Kolodkin et al., 1997; Takahashi et al., 1998). However, Neuropilins have a very short cytoplasmic domain with no signaling motifs required for axon guidance, indicating that while they are capable of binding semaphorins, they are not the main signaling transducing receptor (H. Chen et al., 1998; Nakamura et al., 1998; Yu & Kolodkin, 1999). It was found that Neuropilins form complexes with receptors in the plexin family and that the plexins can act as the signaling elements in the holoreceptor complex (Rohm et al., 2000; Takahashi et al., 1999; Tamagnone et al., 1999).

Plexins act as receptors for all semaphorin family members (Tamagnone et al., 1999). They were first discovered in *Xenopus laevis* using a monoclonal antibody (Takagi et al., 1987), and it was later found that this protein inhibited the formation of the plexiform layer in the *Xenopus* retina (Ohta et al., 1992), therefore acquiring their name. There are four classes of plexins, classified from A to D (Tamagnone et al., 1999). Classes A and B are present in both vertebrates and invertebrates, but classes C and D are exclusive to vertebrates (Alto & Terman, 2017; Jongbloets & Jeroen Pasterkamp, 2014; Yazdani & Terman, 2006). All plexin family members contain a 500 aminoacid region similar to the Sema domain in semaphorins located at the N-terminal region, which binds to semaphorins by itself or with Neuropilins. In addition to the Sema motif, the rest of the extracellular domain of plexins is highly conserved amongst the protein family members (Pascoe et al., 2015).

Semaphorins and Plexins, are present in all phyla. They can be traced back to unicellular choanoflagellates, which implies that these gene families originated from a common ancestor of choanoflagellates and Metazoa over 600 million years ago, further its highly conserved motifs suggest a similar function across organisms (Figure 1.2) (Junqueira Alves et al., 2019).

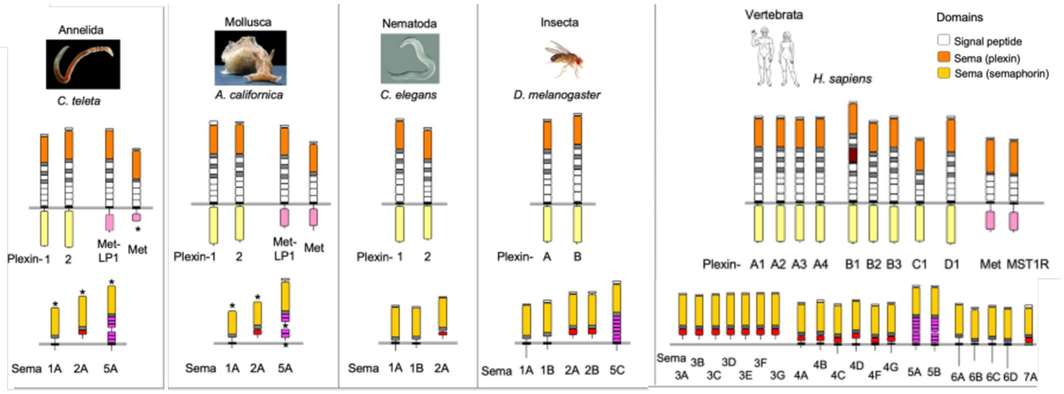

Figure 1.2 Semaphorins and their receptors are conserved in various organisms and all phyla. Semaphorins of all bilaterian Metazoa have high sequence similarity with the two invertebrate classes (class 1 and 2). There are five classes exclusive to vertebrates (class 3–7) and one class of viral semaphorins (not shown). Class 5 semaphorins are present in both vertebrates and invertebrates.

Modified from Junqueira Alves et al., 2019

1.2.2 Semaphorin function

Even though they were first discovered in the nervous system, semaphorins and plexins are also expressed in non-neuronal organs, such as the cardiovascular, endocrine, gastrointestinal, hepatic, immune, musculoskeletal, renal, reproductive, and respiratory systems from development to adulthood where they participate in significant physiological processes (Alto & Terman, 2017). Some of these processes are morphology-related, such as changes to cell adhesion, cell migration, and cytoskeletal organization (Fan et al., 1993; Hung & Terman, 2011; Kruger et al., 2005). In the context of this dissertation, I will focus on how semaphorins function in the nervous systems during development and adulthood and their role in neuronal injury.

During neurodevelopment, semaphorins are expressed by neuronal and non-neuronal cells, acting as guidance cues for neuronal growth cones and aiding axons to reach their targets by working as chemorepellents (Pasterkamp, 2012). The ability of semaphorins to guide axons has been observed in several species. In *Drosophila,* semaphorin 1a participates in patterning of neuromuscular connectivity in the PNS, in which it normally functions to mediate specific axon defasciculation events (Yu et al., 1998). Similarly, in the limb bud of Grasshopper where it was initially discovered, Sema I is expressed by epithelial cells and acts as a repulsive cue to delay or stop proximally extending axon growth cones to allow other guidance molecules to direct pioneer axons from the limb to the CNS (Kolodkin et al., 1992).

In vertebrates, secreted semaphorins produce in vitro growth cone collapse in Dorsal Root ganglion cells (DRGS) in chicken and mouse (Luo et al., 1993; Mlechkovich et al., 2014). Semaphorins in the peripheral nervous system prevent the axons of dorsal root ganglion neurons, cranial nerves, spinal motoneurons, and sympathetic neurons from deviating from their correct path (Masuda & Taniguchi, 2016). In the mouse, when the secreted SEMA3A receptor Plexin A4 (PlxnA4) is knocked out, developing sensory axons grow in an uncontrolled manner due to the lack of growth cone repulsion (Danelon et al., 2020; Yaron et al., 2005).

Interestingly, SEMA3A acts as a chemoattractant in the developing cortex for migrating cortical neurons (Chen et al., 2007). It can also promote dendritic arborization of the basal dendrites in layer V pyramidal neurons (Danelon et al., 2020; Gu et al., 2003; Tran et al., 2009; Yaron et al., 2005). In the process of synapse formation, a secreted semaphorin, SEMA3F, regulates synapse specificity by selectively limiting dendritic spine density along apical dendrites of deep layer cortical pyramidal neurons (Tran et al., 2009).

Considering the many important roles semaphorins play in neurodevelopment it is no surprise that changes in semaphorin expression have been described in several types of neuropathologies and injury to the nervous system (Fard & Tamagnone, 2021; Mecollari et al., 2014).

1.2.3 The role of semaphorins in neurite regeneration

The vertebrate class 3 semaphorins, which are secreted, have been widely studied regarding their role in CNS injury (Mecollari et al., 2014; Pasterkamp & Verhaagen, 2001). Several studies have shown that Sema 3 expression increases in the mouse spinal cord and cerebral cortex, starting 24 h after injury and possibly for up to two months (De Winter et al., 2002; Hashimoto et al., 2004). Further, inhibiting SEMA3A, one of the class 3 semaphorins, promoted regeneration and reconnection in several mouse injury models such as adult hippocampal slices (Montolio et al., 2009), olfactory nerve regeneration after axotomy *in vivo* (Kikuchi et al., 2003), and promoted a regenerative response and functional recovery after a complete spinal cord transection (Kaneko et al., 2006). Moreover, a SEMA3A-blocking antibody was able to rescue ganglion cells (RGCs) from SEMA3A-induced apoptosis after optic nerve axotomy (Shirvan et al., 2002). Interestingly enough, in the permissive PNS environment, SEMA3A expression decreased after nerve injury by crushing facial and spinal motoneuronal axons (De Wit, 2003), which could aid in the regrowth of peripheral processes.

The role of other Semas has also been investigated. A recent study showed that expression levels of SEMA4C, SEMA4D, SEMA5A, SEMA6A, and SEMA6D were elevated one week after spinal cord injury in mice. Furthermore, mice deficient in the receptors for SEMA4C, SEMA4D, SEMA5A, and SEMA6D present enhanced axonal regrowth and reduced axon retraction (Ueno et al., 2020).

Even though there is ample evidence concerning the involvement of semaphorins in recovery after injury, several questions remain unanswered. Are the mechanisms involved in the response to injury of adults' neurons the same as in axon guidance during neurodevelopment? Are these regenerating axons sensing semaphorins? Is the PNS more successful at regeneration because it is able to downregulate semaphorin expression?

1.3 *C. elegans* as a Model Organism

Caenorhabditis elegans (*C. elegans*) is a small (0.25-1 mm, depending on life stage) cylindrical and transparent nematode that typically lives in soil and organic matter and can be found worldwide (Félix & Duveau, 2012). In 25°C this nematode has a 3-day life cycle, a 10-day lifespan, and a progeny size of up to 250 offspring per individual (Figure 1.3A), allowing researchers to obtain many animals in a very short time and in a relatively small space (Brenner, 1974; Corsi et al., 2015).

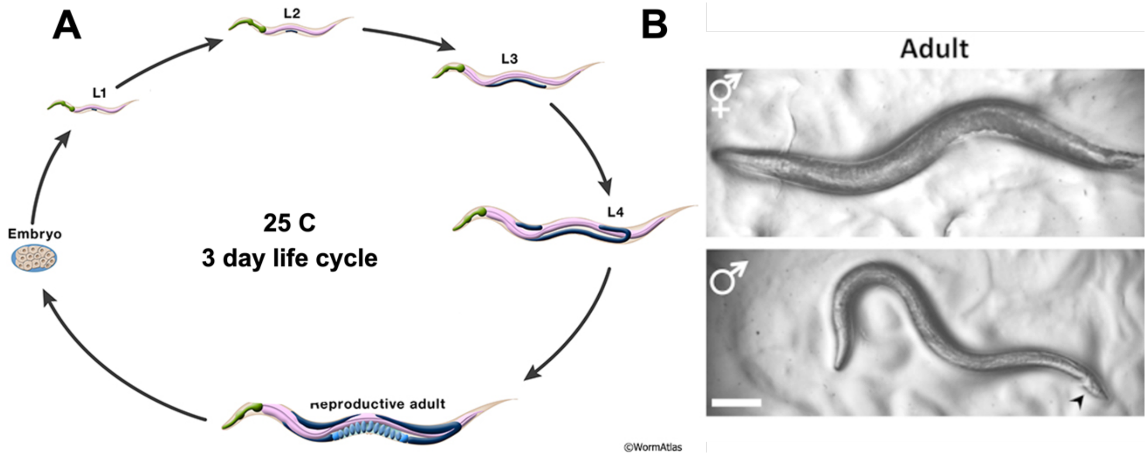

Figure 1.3 *C. elegans* life cycle from embryo to adult male or hermaphrodite**.** A) Life cycle at 25°C. The animals develop from embryo through four larval stages before becoming reproductive adults. B) Micrographs of adult hermaphrodite (top) and male (bottom) animals. Males are easily distinguished by their "harpoon" shaped tails (black arrowhead).

Adapted from (Corsi et al., 2015; Herndon et al., 2018).

Even though there is a small percentage of males (>0.1%), it mainly exists as a self-fertilizing hermaphrodite (Figure 1.3B). This characteristic is advantageous for genetics and other studies in the laboratory because self-fertilization simplifies stock maintenance since a single animal can produce an entire population with very low inter-worm variability (Corsi et al., 2015). Self-fertilizing hermaphrodites tend to become homozygous over time, which means that mutagenized strains will eventually become isogenic (Brenner, 1974).

C. elegans is also known for its ease of cultivation in the laboratory, making it a highly accessible and cost-effective model organism for scientific research. The animals can be grown in agar plates seeded with a lawn of a non-pathogenic *E. coli* strain which acts as their food source (Brenner, 1974). Another advantage is its easy long-term storage by freezing, allowing researchers to build up extensive collections of mutant strains (Brenner, 1974), which are available through collaborations and repositories.

Its invariant number of 959 somatic cells has allowed researchers to map every cell from fertilization to adulthood and generate a complete cell lineage (Kimble & Hirsh, 1979; Sulston et al., 1983; Sulston & Horvitz, 1977). Its nervous system, comprised of 302 neurons in the adult hermaphrodite, has been reconstructed from electron micrographs, providing the most complete wiring diagrams of any nervous system (White et al., 1986), and recent studies added new EM images and connectivity dataset (Brittin et al., 2021; Cook et al., 2019; Witvliet et al., 2021).

Since *C. elegans* was adapted for culture in the lab by Sidney Brenner in 1963 (Brenner, 1974, 2009), mutations that lead to developmental and behavioral defects have been identified in genetic screens. Several decades later, *C. elegans* was the first multicellular organism to have its genome fully sequenced (*C. elegans* Sequencing Consortium, 1998). This led to the molecular identification of many essential genes in developmental and cell biological processes through forward and reverse genetics. Further, its genome is highly conserved, with about 40% showing homology to mammalian genes (Kaletta & Hengartner, 2006; Lai et al., 2000). This has made it a valuable model for studying various biological processes, including development, aging, and disease.

The availability of a comprehensive "biological toolkit" that can be used in *C. elegans* has positioned this small transparent nematode as one of the leading model organisms. For example, gene activity can readily be reduced by feeding bacteria expressing RNAi (Fire et al., 1998; Timmons et al., 2001), and many processes can be studied in live animals at the single-cell level using fluorescent proteins. Many optogenetic tools that can change specific neurons' activity have recently been developed and used in *C. elegans* (Haspel et al., 2020; Husson et al., 2013).

Additionally, laser microsurgery can be used in *C. elegans* to ablate entire cells or perform a small injury to neurites in the nervous system (Fang-Yen et al., 2012; Haspel et al., 2020). The possibility to ablate one or more cells in a living organism has helped to determine the functions of various neurons, for example, those involved in locomotion, feeding, mechanosensation, and chemosensation (Avery & Horvitzt, 1989; Bargmann et al., 1993; Bargmann & Horvitz, 1991; Chalfie et al., 1985; Gabel et al., 2007; Gray et al., 2005; Li et al., 2006; Tsalik & Hobert, 2003; Ward et al., 2008). This technique can also be used to perform small cuts or injuries to individual nerve fibers, axons, and dendrites and was used to show that the *C. elegans* nervous system has regenerative ability (Gabel et al., 2008; Harreguy et al., 2020, 2021, 2022; Haspel et al., 2020; Yanik et al., 2004).

1.3.1 The *C. elegans* nervous system

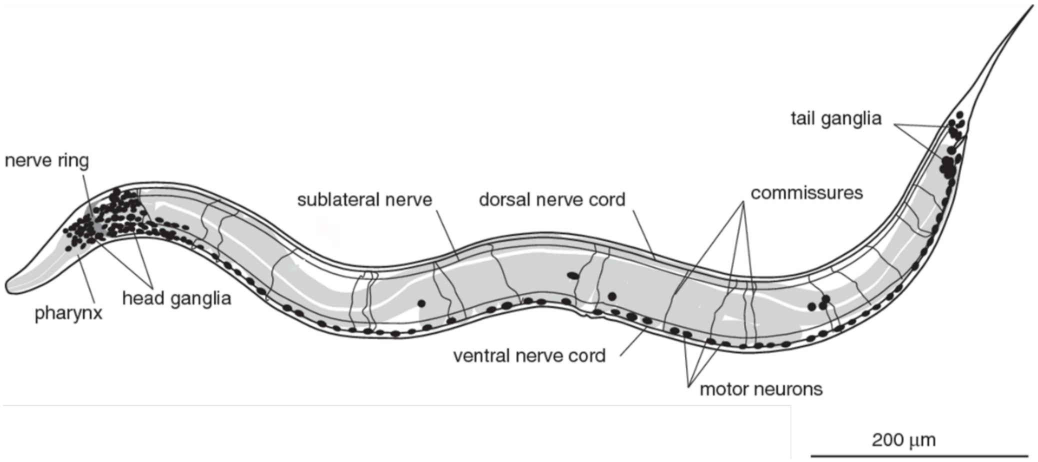

Figure 1.4 The *C. elegans* nervous system. It comprises the head and tail ganglia and the ventral and dorsal nerve cord, which runs along the animal's body and where the motoneurons that drive locomotion are located. Some motoneurons extend commissures from the dorsal to the ventral side of the animal to innervate dorsal body muscle. *Adapted from* (Hobson et al., 2017).

There are 302 neurons in the hermaphrodite and 385 in the male adult *C. elegans* (Sulston & Horvitz, 1977; White et al., 1986). Most neuronal cell bodies are found in the head and tail ganglia and arranged along the ventral side of the animal, forming the ventral nerve cord (VNC, Figure 1.4 ; Altun & Hall, 2005). While most neurons have a very simple structure with only one or two neurites, certain neurons can have highly branched and complex neurite trees. Except for a few cases, it is not possible to differentiate axons from dendrites because they both transmit and receive synapses (Corsi et al., 2015). In addition to neurons, *C. elegans* has 56 glia-like cells that are primarily associated with sensory neurons and do not produce myelin (Oikonomou & Shaham, 2011). Despite its compact size and the simplicity of its nervous system, *C. elegans* is capable of a wide range of behaviors, including locomotion, feeding, mating, orientation to attractants, repellents, temperature, and the earth's magnetic field (Vidal-Gadea et al., 2015), associative and no-associative learning, as well as making rational (Faumont et al., 2012) and irrational (Iwanir et al., 2019) decisions. All behaviors are generated by nervous systems that integrate sensory input and internal state, engage in neural processing, and generate a motor program that affects the body and world through muscle contraction.

Of *C. elegans'* 302 neurons, approximately 113 are motoneurons that innervate muscle to control locomotion and the movement of reproductive and feeding behaviors. They move in their environment in an undulatory pattern by propagating dorsoventral body bends against the direction of locomotion and can either crawl on solid surfaces or swim in liquid media (Haspel et al., 2020). Crawling and swimming are controlled by 75 motoneurons along the VNC that innervate 75 body-wall muscle cells posterior to the head (Corsi et al., 2015)

The VNC locomotion motoneurons differentiate into eight classes with stereotypical iterating connectivity (Haspel & O'Donovan, 2011, 2012): A-type (VA, DA) and B-type (VB, DB) motoneurons are excitatory and cholinergic, and are active during backward or forward movement, respectively (Haspel et al., 2010). D-type motor neurons (VD and DD) are inhibitory GABAergic neurons and are post-synaptic to muscle cells and other motor neurons (Deng et al.,2020; Haspel et al.,2020). AS motoneurons are similar in shape to DA but are not associated with a direction of locomotion, and VC motoneurons mainly control muscles in the vulva. VA, VB, VC, and VD classes innervate ventral muscles, while DA, DB, DD, and AS neurons innervate the dorsal muscles by sending commissures to the dorsal side (Figure 1.4) (White et al., 1976, 1986).

There are 46 motoneurons that extend commissures from the VNC to the dorsal side of the animal. These commissures present a convenient positioning and morphology that allows for easy identification of the neuron they extend from, as well as an easily distinguishable target for laser injury to evaluate regenerative capacity *in vivo*. Further, it is possible to assess and quantify regeneration only 24 hours after injury (Yanik et al., 2004).

1.3.2 Neuronal regeneration in *C. elegans*

Since it was described that *C. elegans* GABA motoneurons could regrow their neurites after injury (Yanik et al., 2004), multiple types of neurons have been assessed for their regenerative capacity with particular focus on mechanosensory and other types of motoneurons (Chen & Chisholm, 2011; Wu et al., 2007).

Axotomy of motoneurons in *C. elegans* causes locomotor deficits, with functional recovery and axon regrowth observed 24 hours after injury (Harreguy et al., 2020, 2021, 2022; Yanik et al., 2004). Further, injury to PLM, paired mechanosensory neurons that mediate sensing of gentle touch to the posterior body (Chalfie et al., 1985), significantly reduced touch response. Still, the fusion of the regenerated axon with its distal counterpart resulted in the recovery of touch sensitivity. These findings provide evidence that regenerated axons can regain functionality (Neumann et al., 2011; Wu et al., 2007). Other neurons, however, like the paired AFD chemosensory neurons that mediate magnetotactic and thermotactic behavior, do not regenerate or recover their sensory function (Chung et al., 2006a).

Apart from neuron type, several other factors might affect regeneration outcomes after injury. Age affects regeneration after injury in mechanosensory touch neurons, where adult animals showed a decreased regrowth rate compared to L1 animals (Wu et al., 2007). Further, the distal axon fragment after the injury took longer to degenerate and be removed in adults, indicating that debris' clearance or removal rate decreases with age (Wu et al., 2007). The presence or absence of axon guidance molecules also affects regrowth accuracy when the regrowing axons attempt to find their targets. Animals lacking Ephrin signaling, a molecule that both promotes and inhibits regeneration in other organisms and is expressed in *C. elegans* neurons and epidermis (Chin-Sang et al., 1999; Wang et al., 1999), show significantly decreased axon misguidance (Wu et al., 2007), indicating that axon guidance molecules play an important role in recovery and regrowth after injury.

Unlike humans and other mammals, *C. elegans* lacks myelin, invading macrophages, and complex immune responses, making it less suitable for investigating the interaction between injured neurons and these non-neuronal factors. However, *C. elegans*' simpler neuronal environment can be used to isolate molecular factors and focus on fundamental and conserved aspects of neural regeneration since many factors that regulate axon regeneration in *C. elegans* have similar roles in vertebrate organisms (Bejjani & Hammarlund, 2012).

1.3.3 *C. elegans* semaphorins

C. elegans expresses 3 semaphorins and 2 plexins (Figure 1.2 middle); two membrane-bound semaphorins, *smp-1* and *smp-2* that signal through their receptor *plx-1* and one secreted semaphorin, *mab-20* that signals through its receptor *plx-2* (Ginzburg et al., 2002; Nakao et al., 2007) and in a *plx-2*-independent manner through an unidentified receptor (Nakao et al., 2007).

All three semaphorins play a significant role in epidermal morphogenesis, primarily involved in modulating transient cell contacts to prevent the formation or maintenance of inappropriate cell associations (Ginzburg et al., 2002; Ikegami et al., 2012) as they guide ventral enclosure and vulva formation in the hermaphrodite (Ikegami et al., 2012). Further, semaphorin signaling knockouts exhibit a prominent phenotype characterized by frequent displacement of sensory rays in the male-specific tail (Dalpe et al., 2012). During synaptic assembly, *plx-1,* and *smp-1/smp-2* mutants exhibit impaired synaptic tiling of neuromuscular junctions. In the DA8 and DA9 tail motoneurons, the synapses are intermingled instead of each axon forming synapses selectively within a distinct axonal region, providing compelling evidence for the necessity of semaphorin signaling in the development of the *C. elegans* nervous system (Mizumoto & Shen, 2013). Finally, *mab-20* null animals exhibit significant axon guidance defects, with 17% showing fasciculation defects within the dorsal and ventral nerve cords and more than 20% presenting with DA or DB axonal misguidance phenotypes (Roy et al., 2000).

Even though semaphorins play a role in axon guidance and synaptic assembly in *C. elegans* similar to its role in vertebrate neurodevelopment, and they are involved in response to neural injury in vertebrates, the role *C. elegans* semaphorins may play in response to neural injury has not been explored. The relative simplicity of the *C. elegans* semaphorin signaling system makes it an ideal model to address this question.

I hypothesize that semaphorins restrict *C. elegans* regeneration in motoneurons and that their effect must be overcome to achieve successful recovery after injury.

1.4 Objective

This dissertation aims to understand the role of the semaphorin signaling pathway in *C. elegans* neuronal regeneration after injury. In order to address this aim I provide the following body of work organized in the subsequent four chapters.

In Chapter 2, published in 2020 in Scientific Reports (Harreguy et al., 2020), I describe the methods and capabilities of the Yb-doped fiber laser microsurgery platform and compare its functionality and performance with other widely used laser microsurgery tools. Chapter 3, published in 2022 in Frontiers in Cell and Developmental Biology (Harreguy et al., 2022), dives into the role of the two plexin receptors in *C. elegans.* Here I describe expression patterns, their role in neuronal morphology, and their effect on regeneration after laser microsurgery in plexin knockout animals. Finally, in Chapter 4, I look at the three semaphorins, the effects that knocking them down has on the nervous system and body morphology of the animals, and how they respond to injury.

CHAPTER 2

YTTERBIUM-DOPED FIBRE FEMTOSECOND LASER OFFERS ROBUST OPERATION WITH DEEP AND PRECISE MICROSURGERY OF *C. ELEGANS* NEURONS

Originally published in *Scientific Reports*:

Harreguy, M. B., Marfil, V., Grooms, N. W. F., Gabel, C. V., Chung, S. H., & Haspel, G. (2020). Ytterbium-doped fibre femtosecond laser offers robust operation with deep and precise microsurgery of *C. elegans* neurons. Scientific Reports, 10(1), 4545.

2.1 Introduction

A focused pulse of laser light can induce accurately localized sub-cellular damage to approach diverse questions in biology. In the field of neuroscience, laser ablation can kill cells (i.e., neurons and glia) by aiming at the nucleus, or sever neurites (i.e., axotomy and dendrotomy), allowing the study of neuronal function and regeneration in-vivo. Laser microsurgery platforms often use pulsed lasers at nanosecond or femtosecond pulse width. The pulses' high strength electric field ionizes molecules to create a bubble of plasma that vaporizes water and tissue to generate damage (Tsai et al., 2009; Vogel et al., 2005). The absorption process at the focus is non-linear and depends strongly on the pulse intensity, which scales with the pulse energy divided by pulse duration (Chung & Mazur, 2009). Hence, the ten-thousand-fold shorter femtosecond laser pulse requires lower energy for plasma formation and ablation. Pulse energies used for femtosecond pulse ablation are typically tens of nanojoules (nJ), compared to tens of millijoules (mJ) for nanosecond pulse ablations. Excess deposited energy diffuses away from the focal point. Accordingly, longer pulses generate more severe damage beyond the region of laser energy deposition compared to shorter pulses (Fang-Yen et al., 2012).

Laser microsurgery was pioneered and has been an important tool to study the development and neurobiology of *Caenorhabditis elegans* since 1980 when Sulston and White used it to study cell-cell interaction in post embryonic stages (Sulston & White, 1980), and when Chalfie and colleagues ablated neurons to test their necessity for touch sensitivity (Chalfie et al., 1985). Microsurgery of neurites (termed axotomy) was also pioneered in *C. elegans* (Yanik et al., 2004) where a laser-pumped titanium-sapphire laser was used to cut commissure neurites of motoneurons. These Ti:Sapphire lasers are typically conFigure d to produce near-infrared (NIR) pulses with energies up to 50 nJ, a centre wavelength of approximately 800 nm, pulse duration of 100–200 femtoseconds, and repetition rates of 80 MHz. Ablation at 80 MHz does not allow complete dissipation of pulse energy8 and in many cases an external electro-optic pulse picking device is added to reduce the repetition rate and ablate at 1 to 10 kHz. The longer intervals between pulses at these lower repetition rates allow the deposited energy to dissipate completely (Chung et al., 2006b; Gattass et al., 2006; Shen et al., 2005), improving the surgical resolution. Nanosecond lasers were adapted for axotomy, offering lower cost, and more robust design (Chalfie et al., 1985; Williams et al., 2011), but with higher energy per pulse. They are typically diode laser-pumped or Nitrogen laser-pumped dye laser typically conFigure d to produce green (532 nm), blue (450 and 488 nm), or ultra violet (337 nm) light. These lasers have pulse energies up to several mJ, pulse durations of several nanoseconds, and repetition rates up to 10 kHz.

Axotomy using nanosecond and femtosecond pulses at high or low repetition rate varies in the extent of damage to surrounding tissues and in the size of the gap induced in a severed axon, but axon regeneration seems to occur at comparable extents and rates after axotomy (Wu et al., 2007). At low repetition rate (1 kHz), the size of damage to tissue and neurite regeneration rates appear to be mostly affected by pulse energy (Bourgeois & Ben-Yakar, 2007). Laser energies near the damage threshold improve surgical resolution. For any energy level there is a minimal number of pulses that will initiate ablation but adding pulses does not substantially increase the region damaged (Bourgeois & Ben-Yakar, 2007; Chung & Mazur, 2009).

Nanosecond lasers advantages are their relatively low cost, compact size, low maintenance and lower safety requirements. Femtosecond lasers dissect with higher resolution and less damage to surrounding tissues. The choice of laser system is usually motivated by application and involve a compromise, considering precision, cost, and operational reliability. Neurites spaced further apart require less surgical resolution while bundled neurites often require submicron resolution (Chung et al., 2006b). Here we compare a new type of laser, an Ytterbium-doped fibre femtosecond-pulse laser, with the two laser types most commonly used for laser axotomy in *C. elegans*: a femtosecond Ti:Sapphire and a nanosecond diode-pumped passively Q-switched solid-state laser.

2.2 Materials and Methods

2.2.1 Laser platforms

The Yb-fibre system which generates ~400 fs pulses in the infrared (1030 nm) (BlueCut, Menlo Systems GmbH, Germany) includes an integrated pulse picking unit composed of two acousto-optic modulators (AOMs). A fixed AOM reduces repetition rate from 50 MHz to 1 MHz, a second variable AOM reduces it further as low as 1 kHz. We use the BlueCut Control software provided by Menlo Systems with the laser. The software allows user control of the repetition rate (typically, we use 1 kHz) and external gating of the variable AOM by a transistor-transistor logic (TTL) signal. We use a function generator (model 33210 A, Keysight Technologies) to provide the TTL pulse at various lengths (typically 100 ms for 100 pulses at 1 kHz). Reliable picking of single laser pulses can be accomplished through synchronization of the two AOMs in the pulse picker unit. Alternatively, we pick a single laser pulse with a 1-ms TTL signal, accepting occasional fails that are easy to visually recognize. Users control laser power by choosing a level of 1 to 99 arbitrary units that are scaled by the software. Typically, we use 10–20 units for ablations. We measured 3–65 nJ/pulse at the image plane (PM100D Power and Energy Meter Console with S170C Microscope Slide Power Sensor Thorlabs GmbH) when changing the arbitrary units scale from 4 to 35 (of 99). The beam is directed through a beam expander (10X Achromatic Galilean Beam Expander, AR Coated: 650–1050 nm, Thorlabs, USA) and dichroic mirror (750 nm long-pass, Thorlabs, USA).

The diode pumped passively Q-switched solid-state system (1Q532–3), Crylas Laser Systems, USA (Williams et al., 2011), was integrated via a flip-mounted mirror to the same optical path and microscope objective as the Yb-fibre laser. The only components that had to be replaced were the beam expander (10X Achromatic Galilean Beam Expander, AR Coated: 400–650 nm, Thorlabs, USA) and 1:1 beam splitter (Thorlabs, USA) to accommodate the shorter wavelength (532 nm). The Ti:Sapphire femtosecond laser (Mantis Pulse Switch Laser, Coherent, Inc.) generates 100-fs pulses in the near infrared (800 nm). We operated the laser at 10 kHz, used 0.25 s exposure for ablations, and propagated the beam through a home-built 10x Galilean expander.

2.2.2 Ablation parameters

We ablated samples with 13 to 15-nJ (Yb-fibre), 10-nJ (Ti:Sapphire), and 28-μJ (nanosecond) pulse energies, at 1–10 kHz repetition rate. We used 100 pulses in all cases except for ink ablations with the nanosecond laser, for which we used 5 pulses. We focused pulses with an Olympus UAPO 40×, 1.35 NA oil immersion objective for ink, bundle, and motoneuron ablations and an Olympus 100×, 1.4 NA oil immersion objective for motoneuron ablations. Where possible, laser power and pulse number were set to the minimum setting in which damaged could be observed.

2.2.3 Measurement of lesion area and estimation of minimal power and beam size

Lesion area at the focal plane was determined by focusing the laser through a coverslip (22 × 40 mm rectangular #1.5 (0.17 mm) thickness) onto a layer of black ink (Sharpie permanent marker, ink side was facing up and away from objective lens). Bright field mages were acquired (acquisition software: MicroManager v.2.0, camera Flash4.0 Hamamatsu, Japan) after lesion at the focal plane, as well as 2 μm above and below. Largest diameter of damage area was quantified from 5 images using ImageJ (FIJI distribution v.1.52).

To estimate the minimum ablation power and damage size, we followed a procedure described by Liu (J. M. Liu, 1982). We set both Ti:Sapphire and Yb-fibre lasers power to the minimum energy in which a damage spot could be observed on a slide covered in black ink frequency was set in both cases at 10 kHz. At least 10 damage spots for each power setting were made on the black slide in each case before increasing power. Power was increased in the smallest possible increments and new damage spots were made to the ink. Power for each setting was measured with an optical power and energy meter (Thorlabs). We plotted the square of the damage diameter against the log of pulse energy.

2.2.4 Bundle ablation

Bundle ablation was performed in adult animals that express green fluorescent protein (GFP) either pan-neuronally (strain NW1229) or in the amphid neurons (strain NG3416), obtained from *C. elegans* Genetics Center and Gian Garriga, respectively. In all cases, an area of the bundle that included multiple neurites was brought into focus and the laser was aimed at a neurite in the bundle. Images were taken before and after lesion with MicroManager (Edelstein et al., 2014) or Nikon Elements.

2.2.5 Laser axotomy and regeneration measurements

For laser microsurgery and time-lapse microscopy, *C. elegans* hermaphrodites at the fourth larval stage (L4) were mounted by placing them in a drop of cold, liquid 36% Pluronic F-127 (Sigma-Aldrich) with 1 mM levamisole (Sigma-Aldrich) solution, and pressed between two coverslips (Melentijevic et al., 2017). The slides were brought to room temperature, to solidify the Pluronic F-127 gel and immobilize the animals. Laser axotomy was performed using both the Yb-fibre and the nanosecond pulse laser system installed on the same microscope (ASI RAMM open frame with epifluorescence and bright field

Olympus optics), for adequate comparison. In both cases, the beam was focused to a diffraction-limited spot that was first located on the live image by lesion of a surface of black ink on a coverslip as described above. The targeted neuron was visually inspected immediately following laser exposure (100–500 ms) to confirm successful axotomy. In some cases, multiple laser exposures were necessary to generate a break in the nerve fibre. Axotomy of D-type motor neurons were done by severing the anterior ventral-dorsal commissures 40–50 μm away from the ventral nerve cord. Neuronal regeneration was assessed 24 hours after axotomy on the same microscope and imaging system.

2.2.6 Quantification and analysis

Z-stacks were acquired both before and immediately after injury as well as 24 h post injury. Maximum intensity projections were constructed, and post injury images (1 min post injury) were analysed to quantify the damage area. Images taken 24 h post injury were analysed to quantify outgrowth. Outgrowth was counted when a new branch extended from the injury site. Image measurements and analysis were carried out with ImageJ software v.1.52, and statistical analysis was done with GraphPad Prism v.8.0.50.

2.2.7 Statistics and interpretations of results

Most of the D motoneuron regeneration and ectopic outgrowth data is binary: we score whether or not neurons regrow or outgrow. We calculated p-values for these data by Fisher's exact test. For the size of the injury, we calculated p-values by the unpaired, unequal variance, two-tailed t-test. For the ink damage test, we conducted a one-way analysis of variance (ANOVA). We performed post-hoc comparisons using the Tukey test. Data are represented as average ± standard deviation (SD). * and ** indicate values that differ at $p < 0.05$ and 0.001 levels, respectively.

2.3 Results

2.3.1 Ytterbium-doped fibre femtosecond laser

Rare-earth doped mode-locked fibre laser produces high power pulsed radiation by amplifying seed source radiation through a thin coiled fibre. Specifically, Yb2O3-doped fibre lasers emit pulses that are one hundred to hundreds of femtoseconds wide, with wavelengths 1000–1100 nm, at average power of milliwatts to tens of watts (Limpert et al., 2002). The basic design is similar to Ti:Sapphire lasers that are very commonly used for multiphoton imaging and axotomy (Chung et al., 2013; Curley et al., 1992). One advantage of Ti:Sapphire laser over Yb-fibre is that the wavelength is tunable, but this advantage is not crucial for ablation applications such as ours. The advantages of Yb-fibre are higher possible power, lower maintenance, smaller footprint, and air cooling. The specific system used here (BlueCut, Menlo Systems GmbH, Germany) includes an internal pulse picker which simplifies set up and lowers the overall cost compared to Ti:Sapphire systems that require an external pulse picker. Our Yb-fibre system can ablate with user-defined repetition rate of single shot to 50 MHz and pulse energies of nJ to μJ. As further described in the Methods, in the Yb-fibre ablation setup the laser beam is sent through a beam expander into a microscope objective that focuses the pulses into a sample. Brightfield and fluorescent light is captured by a sCMOS camera for visualization and targeting (Figure 2.1a).

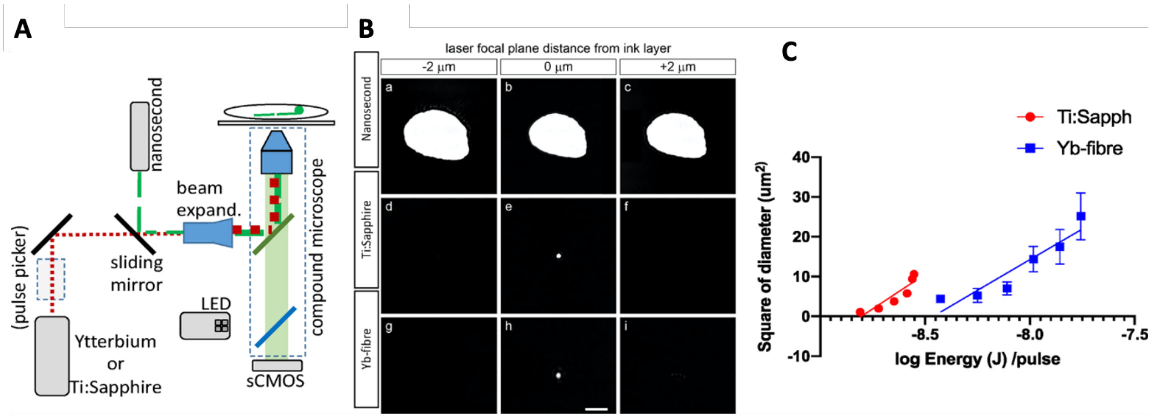

Figure 2.1 Yb-doped fibre femtosecond laser integrated in epifluorescence microscope produces a small damage spot, comparable to Ti:Sapphire laser. A) Lasers are integrated to an epifluorescence compound microscope through a beam-splitter or dichroic mirror. Note that some lasers require an external pulse-picking device. B) Damage spot on a thin layer of black ink is larger when induced with a nanosecond pulse laser (top) than with either of the femtosecond lasers (middle Ti:Sapphire; bottom Yb-fibre). Damage spots are not reduced in size two micrometres above or below the image focal plane for the nanosecond pulse laser, while undetected for the femtosecond pulse lasers. Scale bar = 5 µm. C) Square diameter of damage plotted against log scale of the energy per pulse used to estimate theoretical minimum beam size (square root of slope) and the threshold energy (x-axis intercept) for Ti:Sapphire (red) and Yb-fibre (blue).

2.3.2 Lesion size

We evaluated lesion size by focusing the laser beams through a coverslip onto a layer of black ink (Figure 2.1B). We adjusted the laser to the lowest possible power setting that induced axotomy. Yb-fibre laser produced a slightly smaller damage at the focal plane (Figure 2.1e; 1.34 ± 0.25 µm; n = 15; $p = 0.04$) than Ti:Sapphire (Figure 2.1h; 1.66 ± 0.36 µm; n = 16); neither generated significant damage 2 µm above or below the focal plane (Figure 2.B.d,f,g,i). The nanosecond-pulse laser produced a much larger lesion than either femtosecond laser ($p < 0.0001$) not only at the focal plane (12.5 ± 0.5 µm) but also 2 µm above or below (13.0 ± 0.4 µm; 14.0 ± 0.4 µm). Even though smaller lesion sizes were reported for the nanosecond laser, that study utilized a very low energy setting (10 pulses at 100 Hz) only meant for alignment and not for axotomy (Williams et al., 2011).

To calculate the minimum theoretical beam size diameter as well as the threshold energy we used the extrapolating method described by Liu et al. (J. M. Liu, 1982). As shown in Figure 1c, we plotted square diameter of damage area against the log of the pulse energy and fit data to a line. We calculated the theoretical minimum beam size as the square root of the slope of the line. We calculated the threshold energy as the x-axis intercept of the same line (Figure 2.1C). The calculated minimum diameter was 5.9 ± 2.1 µm for Ti:Sapphire and 5.6 ± 2.2 µm for Yb-fibre; threshold energy was 1.57 ± 0.54 nJ and 3.4 ± 0.8 Nj, respectively.

We estimated the peak intensities by modelling the pulse intensity, I(x, y, t), as Gaussians in the transverse directions (x,y) and in time (t) (Vogel et al., 2005). The Gaussians are defined by full width at half maximum (FWHM) in each direction. The FWHM in the transverse directions are the minimum diameter, d, calculated from the fit in Figure 2.1c. The FWHM in the temporal direction is the pulse duration, τ. Integrating I(x, y, t) over all x, y, and t, we find that the pulse energy E = I0 d2 τ (π/ln(16))3/2, where I0 is the peak intensity. By using the threshold energy calculated from Figure 2.1c and assuming pulses without optical stretching (100 fs for Ti:Sapphire, and 400 fs for Yb-doped laser), we obtain I0 = 3.7 × 1010 W/cm2 for Ti:Sapphire and 2.2 × 1010 W/cm2 for Yb-doped fibre laser. Because some linear absorption of laser light by the black ink may occur, the threshold energy is likely underestimated and the minimum diameter is likely overestimated, so that I0 is higher for cells.

2.3.3 Qualitative accuracy test by dendritic bundle ablation in *C. elegans*

A Ti:Sapphire laser system can selectively ablate one sensory dendrite in a tight bundle of twelve dendrites (Chung et al., 2006b). These dendrites are sensory organs of the twelve amphid neurons located in the nose of *C. elegans*. We replicated this treatment using both the nanosecond pulse laser and the Yb-fibre laser. The Yb-fibre femtosecond laser, similar to the Ti:Sapphire, is capable of ablating only one neurite in the bundle with no damage to surrounding tissue. However, the nanosecond-pulse laser produces a larger injury affecting surrounding tissue and therefore damages more than one dendrite (Figure 2.2). The damage observed for the nanosecond-pulse laser is more localized than what we previously described in Figure 2.1B. This could be due to the fact that the higher energy might be causing thermal damage to the ink while not vaporizing the tissue. Additionally, the three-dimensional geometry and the ability of the energy to penetrate through the tissue also need to be considered.

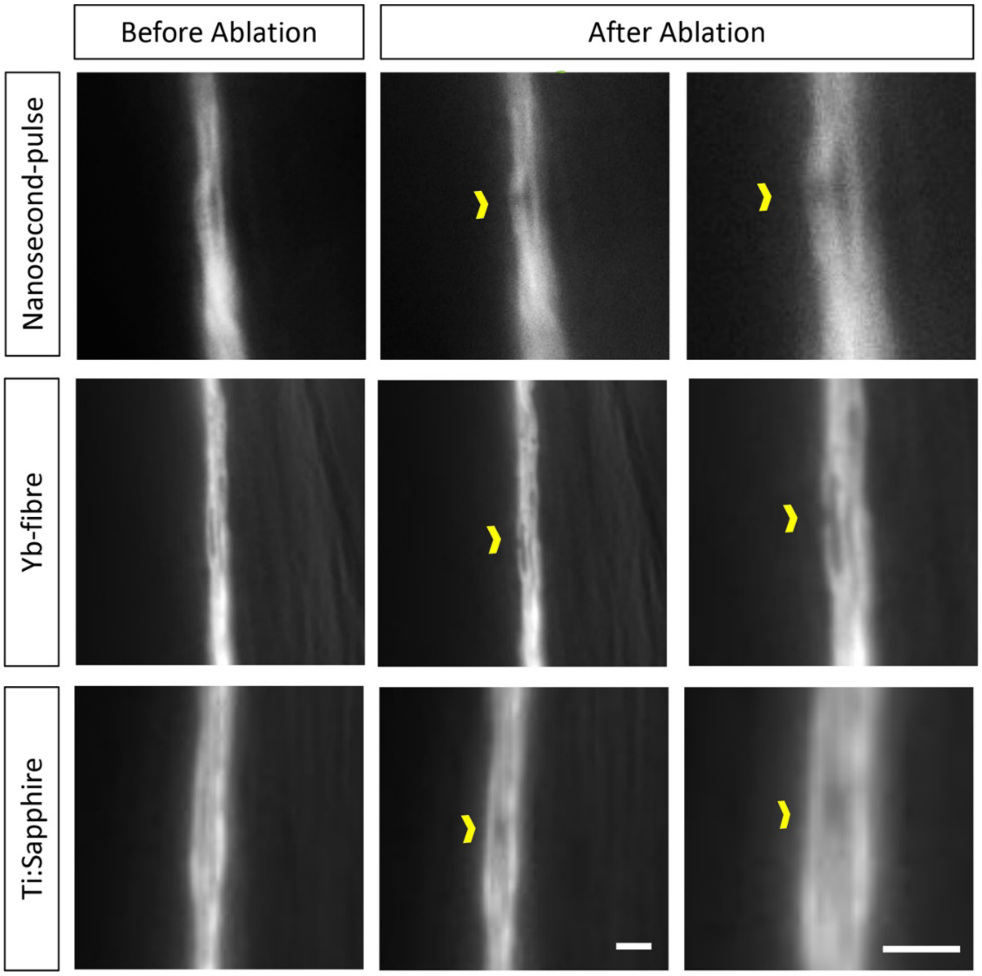

Figure 2.2 A single *C. elegans* dendrite can be injured without damage to neighbouring dendrites. A single dendrite located in a sensory bundle in the nose of the animals was successfully ablated (yellow chevron) using the Ti:Sapphire and the Yb-fibre lasers without collateral damage to adjacent dendrites. The nanosecond-pulse laser injured more than one dendrite. Scale bar = 2 µm.

2.3.4 Quantitative regeneration assessment in *C. elegans* motoneurons

Finally, we assessed how the different laser setups might impact neuronal regeneration in *C. elegans* (Figure 2.3). We aimed the three laser systems at commissures of D-type motoneurons which extend from the ventral to dorsal side of the animal (Figure 2.3A). The size of the axotomy-gap (Figure 2.3B) between severed ends produced by the nanosecond laser after initial retraction (3.8 ± 1.4 μm) was significantly larger than the gap produced by Yb-fibre laser (2.4 ± 0.8 μm, $p = 0.02$) or Ti:Sapphire laser (2.03 ± 0.49 μm, $p < 0.0001$). However, similar proportion of neurites regenerated after injury (Figure 2.3C; $p = 0.12$) with the Yb-fibre laser (27 of 50 neurons in 11 animals), nanosecond laser (11 of 32 neurons in 11 animals), or Ti:Sapphire laser (16 of 26 neurons in 9 animals).

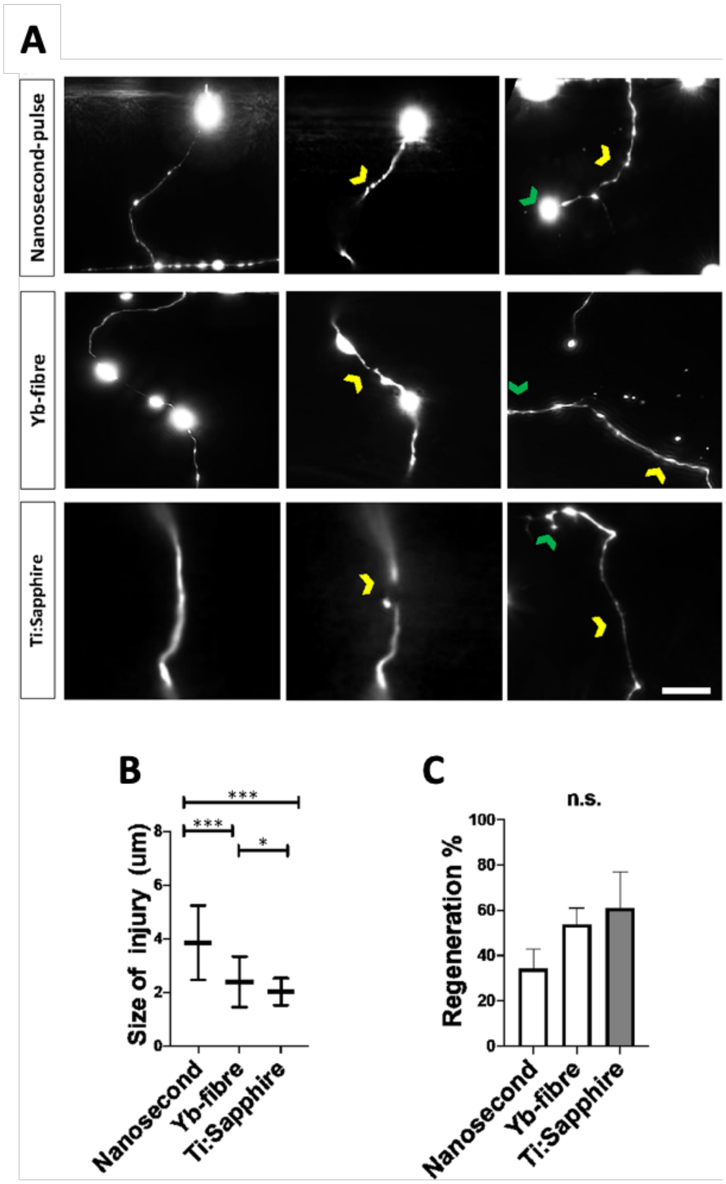

Figure 2.3. Nanosecond laser induces larger gap at site of injury but injured neurons regenerate at similar rate. A) *C. elegans* motoneuron axotomy. Commissures of D motoneurons in immobilized animals were axotomized, animals were recovered and axon found again next day to asses regeneration. Images taken before, 1 second after and 24 hours after injury. Sites of axotomy (yellow chevron) and regenerating branch (green chevron) are indicated. B) Mean gap between injured tips was larger after injury with nanosecond laser. C) Percentage of neurons that regenerated at 24 h was the same for the three types of lasers. Images in A for before and at 24 h are maximal projections of Z stacks while the images at 1 s are each a single frame, leaving some parts of the neuron out of the imaging plane. *$p < 0.05$ ***$p < 0.001$. Scale bar. = 5 µm.

2.4 Discussion

Yb-doped fibre lasers possess several advantages over more commonly used nanosecond pulse lasers and similar capabilities to Ti:Sapphire lasers. Femtosecond fibre laser systems are designed for the high standards of industrial cutting and welding. Compared to a Ti:Sapphire system, Ytterbium-doped fibre laser requires much less frequent alignment and optimization and less maintenance overall. It is our experience that a Ti:Sapphire system requires daily alignment to maintain its operation, but a Yb-doped system turned off for weeks could cut axons as soon as it was turned back on.

Comparable turnkey laser systems, such as the Spectra-Physics Spirit, are commercially available. However, we found that the BlueCut Yb-fibre laser was the most suitable at the time we initiated this study. The most notable reasons include the integrated pulse picking, the simple incorporation of this unit to an existing microscope, air rather than liquid cooling and the relatively lower cost (including the external pulse-picker required for other systems). The Yb-fibre laser used here offers integrated power adjustment and pulse picking, controlled by a dedicated software that can pick single pulses. In our experience, we never use the full laser power and a unit with about 20% of existing power would have been preferable, for safety and cost reasons.

The ability to produce injury depends on pulse energy and duration. The injury producing plasma is induced by a multiphoton absorption that requires a minimal intensity threshold which is only reached at the focal plane. In the case of neuronal injury with a 1.4 NA objective and a pulse duration of 100 fs, this threshold occurs at an intensity of 6.5×10^{12} W/cm^2 or an energy of 4 nJ per pulse (Vogel et al., 2005). In this study, Yb-fibre and Ti:Sapphire lasers produced comparable pulse width (<400 fs), while the nanosecond-pulse laser produced four orders of magnitude longer pulse (<1.3 ns). Hence, the former induces axotomy with lower energy levels and therefore less collateral damage as longer pulses require more energy to reach the threshold intensity. Yet, regeneration rates were comparable among all three systems.

Further, the Yb-fibre laser system enables the lesion of neuronal processes located on the side of an adult *C. elegans* farther from the objective (n > 20 animals). The mounting and diameter of an adult animal requires optical penetration of 80–100 μm deep, compared to 30–40 microns for nanosecond laser systems (Williams et al., 2011). The most probable reason is that near infrared photons penetrate deeper and are less scattered by biological tissue. Reduced scattering also lowers the required energy levels.

Here we have described a new laser axotomy system that provides the same high precision capabilities of widely-used Ti:Sapphire lasers but with less maintenance and higher robustness. This capability is not limited to neurons in *C. elegans* and might be useful to address experimental questions in transparent tissue that require an accurate and localized micrometre-sized lesion up to 100 μm deep with no collateral damage.

CHAPTER 3

SEMAPHORIN SIGNALING RESTRICTS NEURONAL REGENERATION IN *C. ELEGANS*

Originally published in *Frontiers in Cell and Developmental Biology*:

Harreguy, M. B., Tanvir, Z., Shah, E., Simprevil, B., Tran, T. S., & Haspel, G.(2022).Semaphorin signaling restricts neuronal regeneration in *C. elegans.* Frontiers in Cell and Developmental Biology, 10, 814160.

3.1 Introduction

During neurodevelopment, growth factors and guidance cues regulate dendrite morphogenesis, axon growth cone initiation and navigation, axon elongation, and target recognition, but their effects are less pronounced in the adult nervous system. Studying their role in the context of adult regeneration and recovery could provide insight into the molecular and cellular response to injury (Chen et al., 2011; Chisholm et al., 2016).

The semaphorins are a family of glycosylated proteins that were first characterized for their role in the development of the insect and avian nervous systems as axonal guidance cues but were later found in a variety of other tissues and organisms (Alto & Terman, 2017; Junqueira Alves et al., 2019). All semaphorins have a distinctive 500 residue long N-terminal domain, known as the Sema domain. This domain, which is a seven-blade beta-propeller, with each blade formed by four anti-parallel beta-strands (Gherardi et al., 2004), is exclusive to semaphorins and their receptors, the plexins, where it mediates semaphorin dimerization and receptor binding. Eight classes of semaphorins are phylogenetically conserved in nematodes, flies, chick, mammals, and viruses, with three classes of smaller proteins that are secreted and five classes that are membrane-bound by a transmembrane domain or a glycosylphosphatidylinositol (GPI) link (Alto & Terman, 2017; Junqueira

Alves et al., 2019). Correspondingly, four classes of plexins are conserved in invertebrates and vertebrates (Negishi et al., 2005; Tamagnone et al., 1999). All plexins are transmembrane proteins with an extracellular Sema domain that mediates semaphorin binding and signaling, either by themselves or with a neuropilin co-receptor, in the case of the secreted class 3 semaphorins in vertebrates (Negishi et al., 2005; Pascoe et al., 2015).

In mammals, semaphorins and their receptors, neuropilins and plexins, were originally described as guidance cues for neuronal growth cones aiding axons to their targets by acting as chemorepellents (Kolodkin & Tessier-Lavigne, 2011). More recently, semaphorins have been implicated in multiple key roles of neural circuit assembly during neurodevelopment (Koropouli & Kolodkin, 2014; Yoshida, 2012). For example, the mammalian secreted semaphorin, SEMA3A, is involved in various neurodevelopmental processes in the mouse, including repelling dorsal root ganglion sensory axons, promoting basal dendrite elaboration in cortical pyramidal neurons, and pruning of hippocampal axons (Bagri et al., 2003; Danelon et al., 2020; Mlechkovich et al., 2014; Yaron et al., 2005). Another well studied secreted semaphorin, SEMA3F, and its receptor Neuropilin-2, are also involved in axon guidance, synaptic plasticity, and refinement, as well as in restraining the excess of dendritic spines on apical dendrites of cortical neurons and regulating inhibitory interneuron numbers in the hippocampus (Assous et al., 2019; Eisenberg et al., 2021; Riccomagno & Kolodkin, 2015; Riccomagno et al., 2012; Tran et al., 2009). As the mediators of semaphorin signaling, the plexins are involved in axon guidance, synapse and dendrite formation, axonal pruning and synaptic stability (Limoni, 2021; Shen & Cowan, 2010).

In accordance with their role in neurodevelopment, semaphorins could be involved in axonal regeneration after injury (Fard & Tamagnone, 2021). For example, SEMA3A expression levels increase after injury in the spinal cord and cerebral cortex e Winter et al., 2002; Hashimoto et al., 2004) and regenerating axons avoid areas with high SEMA3A expression (Pasterkamp & Verhaagen, 2001). Accordingly, a SEMA3A-specific inhibitor improved axon regeneration and spontaneous hind leg movement after spinal cord transection (Kaneko et al., 2006). Plexin expression and function in response to injury varies depending on the type. Plexin A family members increase their expression after axonal injury in facial motoneurons and rubrospinal neurons, contributing to the role of semaphorins in restricting regeneration (Spinelli et al., 2007). On the other hand, PlexinB2 is upregulated after spinal cord injury in glial cells proximal to the injury site and is required for wound healing and recovery (Zhou et al., 2020).

The *Caenorhabditis elegans* genome encodes for only three semaphorin and two plexin homologues. Of those, PLX-1 binds the two membrane-bound semaphorins (SMP-1 and SMP-2), while PLX-2 binds the only secreted semaphorin (MAB-20; Figure 1A) (Ginzburg et al., 2002; Nakao et al., 2007). Both membrane-bound and secreted semaphorin-plexin systems are involved in development; semaphorins guide ventral enclosure (Ikegami et al., 2012), and regulate epidermal morphogenesis (Ginzburg et al., 2002; Ikegami et al., 2012) as well as vulva and tail-rays morphogenesis in the hermaphrodite and males, respectively (Dalpe et al., 2012). In the nervous system, membrane-bound semaphorin signaling (the *plx-1*/*smp-1*/*smp-2* pathway) is necessary for synaptic tiling in two DA motoneurons in the tail (Mizumoto & Shen, 2013) and for guidance of the long axons of mechanosensory neurons (Ginzburg et al., 2002). Secreted semaphorin signaling (via the *plx-2*/*mab-20* pathway) contributes to motoneuronal axon guidance; eliminating this pathway, when not embryonic lethal, causes defasciculation of the ventral nerve cord (VNC; 17% of surviving *mab-20* knockout animals) and axon misguidance in DA and DB motoneuron classes (4% of surviving *mab-20* knockout animals; (Roy et al., 2000)**.**

3.2 Materials and Methods

3.2.1 Strains and transgenics

We maintained *C. elegans* strains under standard laboratory conditions on nematode growth medium agar (NGM: 0.25% Tryptone, 0.3% Sodium Chloride, 1 mM Calcium Chloride, 1 mM Magnesium Sulfate, 25 mM Potassium Phosphate (pH 6.0), 5 µg/ml Cholesterol, 1.7% Agar) plates with OP-50-1 Escherichia coli bacterial lawn at 15°C (Stiernagle, 2006), without antibiotics. All animals used in the experiments were hermaphrodites.

We acquired semaphorin and plexin mutants from Caenorhabditis Genetics Center (CGC) or the *C. elegans* National Bioresource Project of Japan (NBRP): ev778 (*mab-20*, null), tm729 (*plx-2*, null), ev715 (*smp-1*, null), ev709 (*smp-2*, null), tm10697 (*plx-1*, null), and evIs111 ([F25B3.3:GFP + dpy-20 (+)], pan-neural GFP expression). To allow imaging and microsurgery, we crossed males of NW1229 (evIs111), induced by 10-min exposure of L4 larvae to 10% ethanol (Lyons & Hecht, 1997), with null-mutant hermaphrodites to obtain knockout animals expressing GFP in the entire nervous system: TOL55 (ev715, evIs111, outcrossed x6), TOL57 (ev709, evIs111, outcrossed x6), TOL59 (tm10697, evIs111, outcrossed x1), and TOL62 (tm729, evIs111, outcrossed x1). All strains were verified by PCR upon arrival, after crosses, and at the end of the study. All generated strains and primer sequences for genotyping will be deposited with the CGC.

The reporter strain for *plx-1*p:EGFP (NW2339, 2,621 bp sequence immediately 5′ to the ATG start codon cloned into the multiple cloning site of pPD95_77; (Dalpé et al., 2004) and *plx-2*p:GFP (NW1693, 4,529 bp sequence immediately 5′ to the ATG start codon cloned into the multiple cloning site of pPD95.75) were generous gifts from Dr. Joseph Culotti (University of Toronto, Mt Sinai Hospital) and Dr. Richard Ikegami (UC Berkeley), respectively. For unambiguous identification, we crossed each reporter strain with a NeuroPAL transgenic strain (OH15495; (Yemini et al., 2021)).

3.2.2 Locomotion analysis

We tracked locomotion behavior of multiple animals over an agar surface (1.7% in NGM buffer), without food, as well as in liquid (NGM buffer). We recorded videos with a static multi-worm tracker, composed of three major parts, from top to bottom: 1) a CMOS camera (acA4024-29um, Basler) mounted with a fixed focal length lens (C Series 5 MP 35 mm 2/3″, Edmund Optics), and an infrared cut-off filter (SCOTT-KG3 M25.5 × 0.5, Edmund Optics); 2) a specimen stage for plates or slides; 3) a collimated Infrared LED light source (M850L3 and COP1-B, Thorlabs).

One day before the experiment, we transferred animals of the fourth larval stage (L4) onto a new plate with healthy OP-50-1 bacterial lawn. Ten to fifteen minutes before tracking, animals were transferred onto a 30 mm agar plate with no food or a 150 µL drop of NGM buffer, placed on a microscope slide. During tracking, animals moved freely, and we recorded multiple 25 Hz 15-s videos using Pylon Viewer (Pylon Camera Software Suite, Basler). We analyzed the videos with Tierpsy worm-tracker (Javer et al., 2018) that can track multiple animals and extract up to 726 features for each tracked trajectory. We used the Tierpsy post-processing user interface to merge tracked sections (trajectories) if those were erroneously split by the automatic tracking, and we rejected any trajectory shorter than 3 s, as well as ambiguous cases of animal proximity. Recording and Tierpsy analysis were done by undergraduate researchers, blinded to the animals' genotype and injury condition. We analyzed the HDF5 output file produced by Tierpsy with a MATLAB script (code available upon request) to collect the mean speed and frequency values for each trajectory and then plotted the data and estimated confidence intervals between each group and its control with a freely available software for Estimation Statistics (https://www.estimationstats.com; (Ho et al., 2019); that focuses on the magnitude of the effect (the effect size) and its precision. We also present statistical significance calculated with a two-sided permutation t-test to compare sham vs. injured groups, or one-way ANOVA with Tukey's multiple comparisons test post hoc to compare genotypes (GraphPad Prism v9.2), included as p values in the text and as asterisks that denote levels of significance. We routinely use this tracking system to evaluate and compare wild-type, injured, and uncoordinated mutant strains. We tracked all the knockout, transgenic, and wild-type strains without injury to assess their baseline locomotion parameters. Further, we tracked locomotion to assess recovery 6, 12, and 24 h after microsurgery. For comparison, we also quantified locomotion parameters of sham-surgery groups for each genotype and time point. We treated the sham-surgery groups through the same protocol (including cooling and immobilization, see below), except for the exposure to the laser beam.

3.2.3 Expression and neuronal morphology analysis

To reduce autofluorescence and straighten the animals we incubated fourth stage larvae (L4) in M9 buffer for 90 m and washed in the same buffer three times, incubated in 1 mM Levamisole (a paralytic nicotinic agonist, Sigma Aldrich) for 15 m, and fixed overnight at 4°C in 10% formalin solution, neutral buffered (SIGMA), then washed and mounted with Fluoromount-G (EMS), and allowed the slides to dry for at least 24 h before imaging. We used a laser scanning confocal microscope (Leica SP8; microscope: DM6000CS; objectives: Leica ×40/NA1.30 HC PL APO oil or Leica 63x/NA1.40 HC PL APO oil, with lateral resolutions of 223 nm and 207 nm respectively; laser lines: 405 nm, 561 nm, and 488 nm). We collected multiple optical slices (thickness optimized by the confocal software, ranging 0.343–0.345 µm for the ×63 objective, and 0.410–0.422 µm for the ×40 objective). To analyze morphology and cellular expression we constructed the maximum intensity projections for at least 10 animals of each strain and, in some cases, processed images to reduce background noise via the Leica Application Suite (LASX) software.

For unambiguous identification of VNC motoneuronal expression, we crossed each transcriptional reporter strain with a NeuroPAL transgenic strain and imaged the F1 progeny that expresses both transgenes. The NeuroPAL strains express an invariant color map across individuals, where every neuron is uniquely identified by its color and position (Yemini et al., 2021). We identified 29 motoneurons in three animals and rejected three motoneurons that expressed GFP, but their location and NeuroPAL colors were ambiguous.

3.2.4 Laser microsurgery

For laser microsurgery and associated microscopy, we mounted *C. elegans* hermaphrodites at L4 stage by placing them in a drop of ice-cold, liquid 36% Pluronic F-127 with 1 mM levamisole solution and pressed them between two #1 coverslips (Melentijevic et al., 2017). We brought the coverslips to room temperature to solidify the Pluronic F-127 gel and immobilize the animals. We used a Yb-fiber laser (100 pulses at 10 kHz repetition rate) to cut a single neurite with submicron precision and no discernable collateral damage (Harreguy et al., 2020, 2021). We took images immediately before and after the lesion to visually verify the microsurgery. In some cases, multiple laser exposures were necessary to disconnect a neurite. We disconnected the ventral-dorsal commissures (White et al., 1976) of all motoneurons that we were able to identify by their relative position (at least six per animal), at about 45 µm away from the VNC. We assessed neuronal regeneration 24 h (following most regeneration studies in *C. elegans*, since (Yanik et al., 2004) after microsurgery on the same microscope and imaging system in at least six neurons per animal in at least 15 animals for each condition. We considered neurites regrown when a new branch was observed extending from the proximal segment of the injury site (Harreguy et al., 2020, 2021). When the branch extended to the distal segment or the target of the pre-injury neurite, we considered it regrown and reconnected. We used Fisher Exact on a 2 × 3 contingency table to compare the fraction of observed neurites that regrew or reconnected. We used ImageJ (FIJI v.1.52) and LASX (Leica) for image processing and visualization and Prism (GraphPad v.9.2.0) for statistical analysis and plotting.

3.3 Results

3.3.1 *C. elegans* animals that do not express functional semaphorins or plexins exhibited altered locomotion patterns.

We analyzed the contribution to locomotor behavior of each of *C. elegans* three semaphorins and two plexins (Figure 3.1A) by comparing the speed and frequency of locomotion of knockout (ko) mutant strains to that of wild-type animals. During crawling on agar (Figure 3.1B), all strains translocated significantly slower compared to 204 ± 54 µm/s of wild-type (speed and p values were: *plx-1* 123 ± 37, $p < 0.0001$; *smp-1* 83 ± 33, $p < 0.0001$; *smp-2* 123 ± 35, $p < 0.0001$; *plx-2* 168 ± 41, $p = 0.0011$; *mab-20* 186 ± 51, $p = 0.0016$); and the undulation frequency of all strains was reduced compared to 0.43 ± 0.08 Hz of wild-type (frequency and p values were: *plx-1* 0.29 ± 0.07, $p = 0.0497$; *smp-1* 0.19 ± 0.09, $p < 0.0001$; *smp-2* 0.25 ± 0.06, $p < 0.0001$; *plx-2* 0.36 ± 0.09; *mab-20* 0.36 ± 0.08). Relative to crawling, swimming speed and frequency were less affected by the absence of plexins or semaphorins (Figure 3.1B), only *plx-1*(ko) and *plx-2*(ko) animals translocated slower than 243 ± 88 µm/s of wild-type (speed and p values were: *plx-1*,196 ± 63, $p = 0.003$; *smp-1*,209 ± 94; *smp-2* 234 ± 63; *plx-2* 172 ± 38, $p < 0.0001$; *mab-20* 277 ± 52); only *smp-1*(ko) animals undulated at higher frequency compared to 1.34 ± 0.27 Hz of wild-type (frequency and p values were: *plx-1* 1.53 ± 0.55; *smp-1* 1.62 ± 0.44, $p = 0.0014$; *smp-2* 1.17 ± 0.29; *plx-2* 1.14 ± 0.22; *mab-20* 1.23 ± 0.22). The largest reduction of crawling speed and frequency was in *smp-1*(ko) animals that were also the only genotype to exhibit a change (increase) in undulation frequency during swimming.

We focused further analysis on the plexins (*plx-1* and *plx-2*), because as the only receptors, segregating membrane-bound and secreted pathways, they provide a comprehensive and specific manipulation of these pathways, as well as the identity of the cellular targets (Fujii et al., 2002).

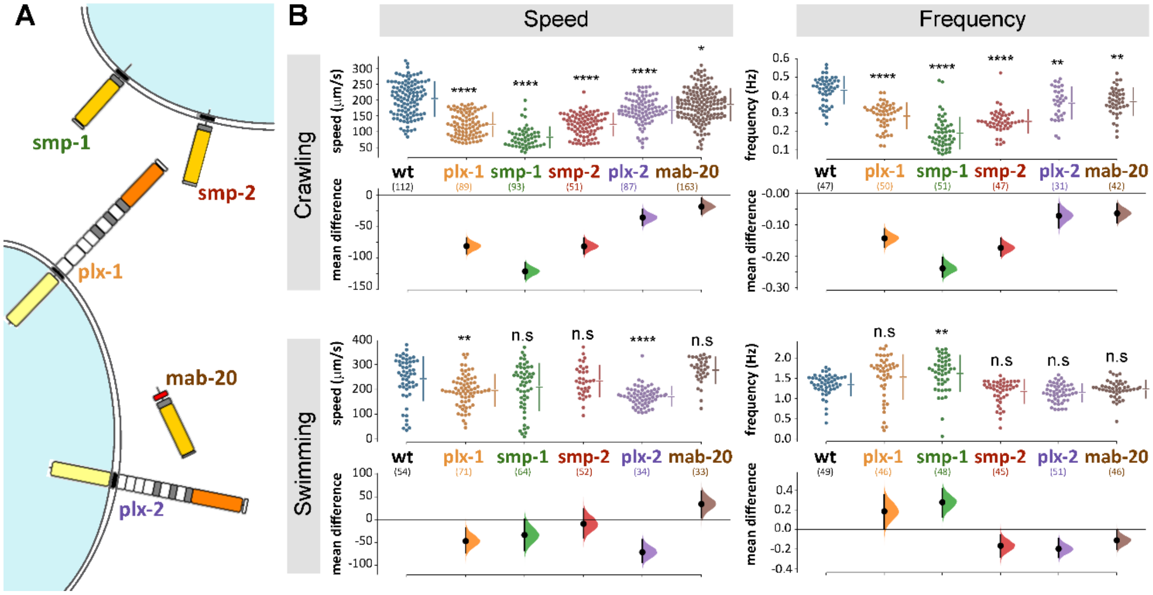

Figure 3.1 *C. elegans* semaphorin system comprises only three ligands and two receptors and omitting any one component affects locomotion. A) Semaphorin signaling system of *C. elegans*. The membrane bound semaphorins *smp-1* and *smp-2* signal through *plx-1*, while the secreted *mab-20* signals through *plx-2* (molecular diagrams adapted from (Junqueira Alves et al., 2019). B) Mutant strains with knocked out semaphorins or plexins are significantly different from wild-type when crawling (locomoting on agar) or swimming (locomoting in liquid media). The largest difference was in *smp-1* (ko) animals. Data points are mean absolute translocation speed or frequency to both directions of locomotion of analyzed trajectories; n. s $p > 0.05$, *$p < 0.05$, **$p < 0.01$, ***$p < 0.001$, ****$p < 0.0001$; one-way ANOVA with Tukey's multiple comparisons test post hoc; in parentheses are the number of analyzed trajectories from 20–25 animals for each genotype.

3.3.2 Gross neuronal morphology was unaffected by the absence of PLX-1 and PLX- 2

We used confocal microscopy to image at least five intact four instar (L4) larvae of each plexin-knockout and wild-type strain, expressing pan neuronal green fluorescent protein (GFP), with emphasis on neuron-rich areas around head, tail, the ventral nerve cord, pharynx, and vulva, and particularly at the commissures of motoneurons (Figure 3.2). We did not observe any morphological differences between mutant and wild-type animals in any of these regions.

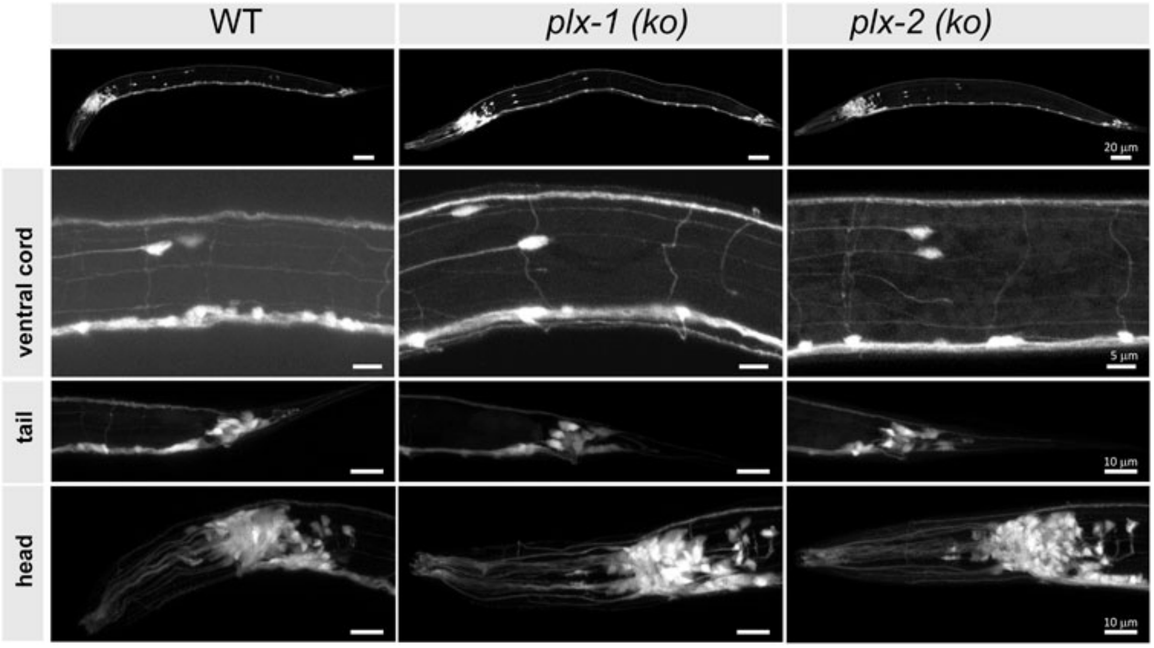

Figure 3.2 Neuronal morphology of plexin knockout strains is comparable to wild-type. The nervous systems are visible *via* pan-neuronal GFP in neuron-rich areas (VNC, head, and tail ganglia) of *wild-type* (WT) and knockout mutant animals [*plx-1* (ko) and *plx-2* (ko)], as well as the entire animals (top), to look for gross neuromorphological differences. We did not observe differences between wild-type and mutant strains. N > 5 animals for each strain. Scale bar = 20 µm (whole animals), 5 µm (VNC), and 10 µm (bottom panels).

3.3.3 Motoneuronal expression of PLX-1 and PLX-2

We imaged transcriptional reporters for *plx-1*p and *plx-2*p in order to identify their neuronal expression in the ventral nerve cord (VNC). GFP under the *plx-1*p promoter (Figure s 3.3 A,B) was mostly expressed in non-neuronal tissue including the pharyngeal muscle, the body-wall muscle in the head and along the body, and vulva muscle. We did not find expression in the nervous system of *plx-1*p:GFP, although a translational reporter was reported to express in the axon of a motoneuron at the base of the tail, namely DA9, of the embryo and L1 larva (Mizumoto & Shen, 2013). GFP under the *plx-2*p promoter was expressed by neurons in the head and tail (Figure 3.3C), as well as in motoneuron in the VNC (Figure 3.3D). Most expressing motoneurons were AS and DA classes (14 and 9, respectively, from three animals), six motoneurons of other classes, namely DB (3), VA (2), and VB (1) also expressed GFP. Both AS and DA extend commissures that were the targets for microsurgery, from the VNC to the dorsal nerve cord on the opposite side of the animal.

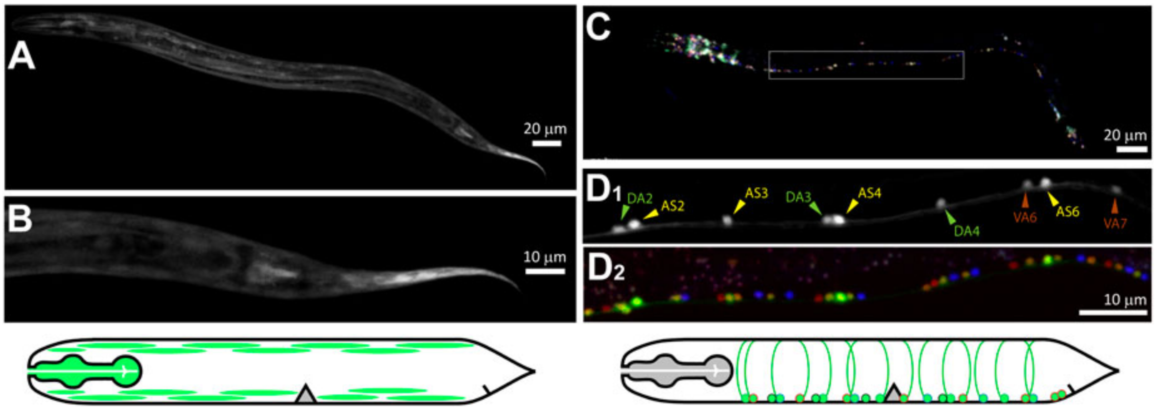

Figure 3.3 PLX-1 is expressed in non-neuronal tissue, while PLX-2 is expressed in excitatory motoneurons. A,B) Green fluorescent protein (GFP) driven by *plx-1p* promoter expressed in non-neuronal tissue such as the pharynx, body-wall muscle. C) GFP driven by *plx-2p* promoter expressed mostly in AS and DA motoneurons and in a few DB, VA, and VB motoneurons. D_1) Examples of DA2-4, AS2-6, and VA6-7 that were identified with co-expressed NeuroPAL (D_2). Scale bars are 20 µm (AC) and 10 µm (BD).

3.3.4 Neurites of plexin knockout mutants regenerate more than wild-type after laser microsurgery

We disconnected 156 commissural neurites of motoneurons of wild-type and plexin knockout mutant animals with laser microsurgery (Harreguy et al., 2020, 2021). These lateral processes extend to connect the ventral and dorsal nerve cords and when multiple processes are disconnected, locomotion is impaired (Yanik et al., 2004). When we examine the same neurite after 24 h, some regrew by sprouting a growth cone from the proximal segment and some of those reconnected to the distal segment or the dorsal nerve cord (Figure 3.4A). In the wild-type, 38 of 73 neurites regrew (0.52 ± 0.11) and only five of those (0.07 ± 0.058) reconnected (Figure 3.4B). The plexin knockout mutants exhibited significantly more regrowth ($p = 0.049$), 33 of 47 (0.7 ± 0.13) for *plx-1*(ko) and 26 of 36 (0.72 ± 0.15) for *plx-2*(ko). Reconnection happened significantly more ($p < 0.0001$) in the plexin knockout strains: in *plx-1*(ko), 13 of the regrown neurites (0.28 ± 0.13) and in *plx-2*(ko), 20 of the regrown neurites reconnected (0.56 ± 0.16).

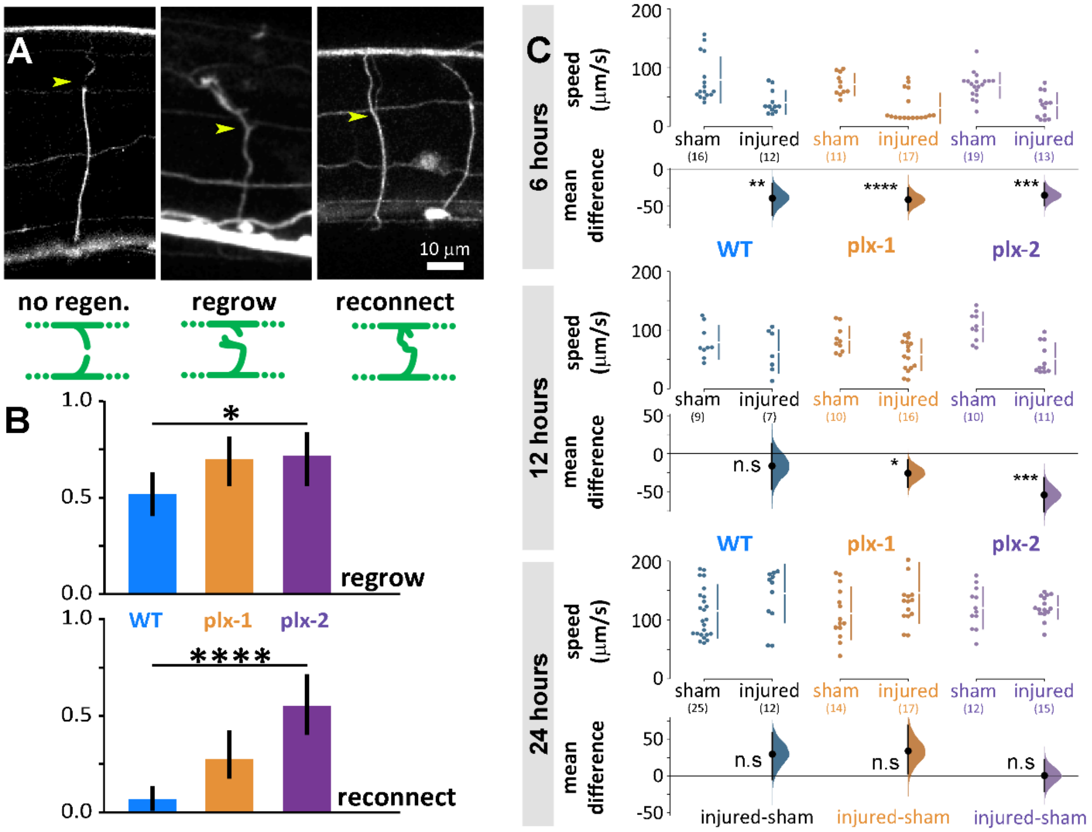

Figure 3.4 Neuronal regrowth and reconnection increased in the absence of plexins 24 h after laser microsurgery, while locomotion speed fully recovers in all genotypes. A) We scored all commissural neurites 24 h after microsurgery (yellow arrowhead for site of lesion, examples are 24 h after lesion) and scored them as exhibiting either no-regeneration (WT), regrowth (*plx-2*(ko), note growth cone), or reconnection (*plx-2*(ko)); schematically demonstrated in green diagrams, see methods. B) About half of wild-type neurites regrew 24 h post-injury and only 7% reconnected. Both plexin knockout mutant strains exhibited more regrowth (top) and *plx-2* exhibited more reconnection (bottom, note that reconnection implies regrowth). Bars are fraction of observed neurites; *$p < 0.05$, ****$p < 0.0001$; Fisher Exact on 2 × 3 contingency table. C) Injured animals of all groups moved significantly slower than sham operated 6 h post-injury, only wild-type recovered at 12 h, and all genotypes recovered when compared to sham operated after 24 h. Data points are mean absolute translocation speed to both directions of locomotion; n. s $P > 0.05$, *$p < 0.05$ ***$p < 0.001$,****$p < 0.0001$; two-sided permutation t-test; in parentheses are the number of analyzed trajectories from 7–20 animals.

Six hours after microsurgery, wild-type and mutant animals moved slower than sham-treated animals of the same genotype (sham vs. injured: WT 79 ± 39 vs. 41 ± 20 μm/s, $p = 0.004$; *plx-1*(ko) 72 ± 18 vs. 31 ± 25 μm/s, $p < 0.0001$; *plx-2*(ko) 70 ± 22 vs. 35 ± 21 μm/s, $p = 0.0001$; Figure 3.4C, top). Twelve hours after microsurgery, the mean locomotion speed of wild-type animals has recovered to levels comparable to sham-treated, while mutant animals moved slower than their sham-treated controls (sham vs. injured: WT 79 ± 28 vs. 63 ± 36 μm/s; *plx-1*(ko) 84 ± 22 vs. 58 ± 26 μm/s, $p = 0178$; *plx-2*(ko) 106 ± 25 vs. 51 ± 26 μm/s, $p = 0.0001$; Figure 3.4C, middle). Subsequently, 24 h after microsurgery, mean locomotion speed has recovered to levels comparable to sham-treated animals for all groups (sham vs. injured: WT 115 ± 45 vs. 145 ± 49 μm/s; *plx-1*(ko) 111 ± 44 vs. 146 ± 51 μm/s; *plx-2*(ko) 120 ± 35 vs. 121 ± 20 μm/s; Figure 3.4C, bottom).

3.4 Discussion

Here we have demonstrated that the two plexins that mediate semaphorin signaling in *C. elegans* restrict neuronal regrowth and reconnection after injury. In their absence, injured neurons of plexin knockout mutants exhibit higher levels of regrowth and reconnection.

By the nature of their ligands, the two plexins mediate different spatial signals. Paracrine interaction, such as those mediated by PLX-1 typically act at short-ranged by cell-to-cell interactions and conform subcellular resolution spatial information (Dalpé et al., 2004, 2005; Gurrapu & Tamagnone, 2016). Because both ligand and receptor are transmembrane proteins, the flow of information could be bidirectional, such as in the case of reverse-signaling through semaphorins, in which plexins function as ligands (Battistini & Tamagnone, 2016; Suzuki et al., 2022; Yu et al., 2010). On the other hand, juxtacrine interactions, such as those mediated by PLX-2 are more disperse over tissue where the ligand typically diffuses to set meaningful concentration gradients (Chen et al., 2007).

We demonstrated that neither the plexins nor the three semaphorins are necessary for gross neuromorphogenesis. However, at low penetrance their omission causes defasciculating and axon misguidance (Roy et al., 2000). In the nervous system, PLX-1 is only expressed by a single motoneuron in the embryo and first stage larva, namely DA9, where it is involved in synaptic tiling during development by restricting the synaptic regions (Mizumoto & Shen, 2013). Because, for the most part, PLX-1 is expressed in muscle and other non-neuronal tissue (Fujii et al., 2002), we hypothesize that its restrictive effect on regeneration is achieved by interaction with the semaphorin SMP-1 presented by the motoneurons (Z. Liu et al., 2005) The neurons could respond indirectly to the surrounding tissue via another signaling pathway, such as the ephrin pathway (as described for efn-4 in relation to *plx-2*/*mab-20*;(Nakao et al., 2007), or SMP-1 could mediate a direct cellular response via reverse-signaling from plexins to semaphorins (Battistini & Tamagnone, 2016; Suzuki et al., 2022; Yu et al., 2010). The other membrane-bound semaphorin, SMP-2, might not be involved in motoneuronal regeneration because it is not expressed by VNC motoneurons, but in body wall muscle and some sensory neurons in the head (Ginzburg et al., 2002). PLX-2 is expressed by four classes of motoneurons, and the most parsimonious hypothesis is that MAB-20 signals via PLX-2 to prevent aberrant neuronal regeneration; MAB-20 secretion from muscle cells generates a gradient that suppresses overgrowth of neurites in health and injury. A similar system was described for regenerating axons of murine spinal cord and brain, where expression of the receptor complex mediating SEMA3A function increases after injury, while SEMA3A secretion at the site of injury declines to undetectable levels during the period of axon regrowth, but persists to be secreted by cells adjacent to the injury site, creating an exclusion zone which regrowing axons do not penetrate (De Winter et al., 2002; Pasterkamp et al., 2001; Pasterkamp & Verhaagen, 2001). Notably, the absence of MAB-20 and PLX-2 had different effects on swimming speed, reminiscent of the different epidermal development phenotypes described for *mab-20*(ko) and *plx-2*(ko) (Nakao et al., 2007).

The phenotypes we describe for uninjured plexin and semaphorin knockout mutant animals are changes in speed and frequency of locomotion on agar surface and in liquid. To the most part, these effects are small in magnitude and include both increases and decreases compared to wild-type animals. The largest effects were on the translocation speed of *smp-1*(ko) during swimming and even worse during crawling. Because the semaphorin signaling pathways are involved in several aspects of embryonic development and its components are expressed in neuronal and non-neuronal tissue in the embryo, the phenotypes are likely the product of an accumulation of effects on structure and function of different tissue, such as muscle, cuticle, or the nervous system. Furthermore, the semaphorin pathways could regulate expression of downstream genes (Alto & Terman, 2017) that in turn affect locomotion behavior. Parsimoniously, because these effects are not the focus of this study, we removed the effect of these locomotion phenotypes by comparing animals after laser microsurgery to sham-operated animals of the same genotype. Moreover, the laser microsurgery experiments included only plexin knockout mutants and *smp-1*(ko) animals were not included in that comparison.

Locomotion behavior was impaired 6 h post-injury and recovered back to pre-injury parameters 24 h post-injury in wild-type animals and both plexin knockout mutant animals.

Because less than half of the neurites in the wild-type animals regrew and only 0.07 reconnected, we hypothesize that the recovery is due to reorganization of the locomotion circuit to produce a meaningful motor pattern that is indistinguishable from that of an uninjured animal (Haspel et al., 2021). Similarly, the recovery of plexin knockout mutants that exhibit much higher levels of regrowth and reconnection can be due to reorganization. Full recovery of locomotion with only partial recovery of neurites and synapses has been described in other systems (Oliphint et al., 2010), but the underlying circuit mechanism is unknown.

The conserved but concise semaphorin-plexin system and readily available genetic and transgenic tools in *C. elegans*, together with accurate injury and quick neuroregeneration and recovery of behavior, provide an attractive experimental model. The secreted and membrane-bound semaphorin signaling pathways both restrict regeneration but in distinct processes that likely include spatial specificity and recurrent signals. Further studies, including of the effect on regeneration of each and combinations of the semaphorins and their localization, before and right after injury, as well as the spatiotemporal dynamics of related secondary messengers such as calcium and cAMP, will address proximate hypotheses about the involvement of semaphorin signaling in neural recovery from injury.

CHAPTER 4

INVESTIGATING THE ROLE OF THE THREE *C. ELEGANS* SEMAPHORINS IN NEURITE REGENERATION

4.1 Introduction

C. elegans has three semaphorins and two plexin receptors. PLX-1 acts as a receptor for membrane-anchored semaphorins, SMP-1 and SMP-2, and MAB-20, a secreted semaphorin, signals through PLX-2 (Fujii et al., 2002; Ginzburg et al., 2002; Ikegami et al., 2004; Nakao et al., 2007; Roy et al., 2000).

SMP-1 and SMP-2 are involved in epidermal morphogenesis; in seam cells to guide ventral enclosure (Fujii et al., 2002; Ginzburg et al., 2002), male tail rays (Dalpe et al., 2012; Nukazuka et al., 2008) and vulva formation (Z. Liu et al., 2005). Further, *smp-1/smp-2* and *plx-1* knockouts exhibit low penetrance axon misguidance in the M1 pharyngeal neuron (Refai et al., 2013). Due to most studies focusing on epidermal defects, nervous system expression of SMP-1 and SMP-2, particularly of the VNC, has not been evaluated in detail. Their role in *C. elegans* neurite regeneration has also not been studied.

On the other hand, MAB-20-deficient animals exhibit a high penetrance of body morphology defects, DA and DB motoneurons axon misguidance, and aberrant cell migration (Roy et al., 2000). Its role in regeneration was assessed in a genetic screen, and it was determined that knocking down MAB-20 significantly increases the ability of the PLM neuron to regrow after laser microsurgery (Chen et al., 2011).

In Chapter 3, which main focus is the plexins, I have previously shown that semaphorin signaling restricts neuronal regeneration in *C. elegans* motoneurons as in the absence of the plexin receptors, regeneration rates, both for regrowth and reconnection, significantly increase (Harreguy et al., 2022). In this chapter, I will explore the role of all three *C. elegans* semaphorins in motoneuron regeneration after laser microsurgery.

4.2 Materials and Methods

I performed all experiments as indicated in Chapter 3 and (Harreguy et al., 2022) unless otherwise specified.

4.2.1 Strains

I maintained *C. elegans* strains as indicated in Chapter 3 (Stiernagle, 2006). The strains I used were TOL55 (ev715, evIs111, outcrossed x6; *smp-1* null), TOL57 (ev709, evIs111, outcrossed x6; *smp-2* null), and a new *mab-20* null strain, made by deletion of 3445 bp, conferring myo-2 GFP and G418 resistance, obtained from CGC, VC4164 (gk5250 [loxP + Pmyo-2::GFP::unc-54 3' UTR + Prps-27::neoR::unc-54 3' UTR + loxP]) (Au et al., 2019), that I crossed to males of NW1229 (evIs111) to obtain a *mab-20 knockout* strain expressing pan-neuronal GFP.

4.2.2 Body morphology analysis

To analyze the body morphology of the MAB-20 knockout animals, I surveyed more than 100 animals, previously fixed and mounted onto an optical slide, under the epifluorescence lamp of the SP8 confocal microscope using the 20X objective. I scored morphological phenotypes as detailed below and quantified them using GraphPad Prism v.10. To analyze morphology and cellular expression, I constructed the maximum intensity projections for at least 10 animals of each strain.

4.2.3 Laser microsurgery

I assessed neuronal regeneration 24 h after microsurgery on anesthetized and immobilized animals (gelled 36% Pluronic F-127 with 1 mM Levamisole) by imaging the injured neurites with a laser scanning confocal microscope (Leica SP8, specifications in Chapter 3).

4.3 Results

4.3.1 Body and neuronal morphology is unaffected in *smp-1* and *smp-2* knockout animals

I acquired images of the entire animals and high magnification images of areas rich in neurons, including the head, tail, VNC commissures, and vulva regions. Body morphology was comparable to the *wild-type,* and no abnormal neuronal connections were identified (Figure 4.1). I analyzed at least 10 animals per genotype.

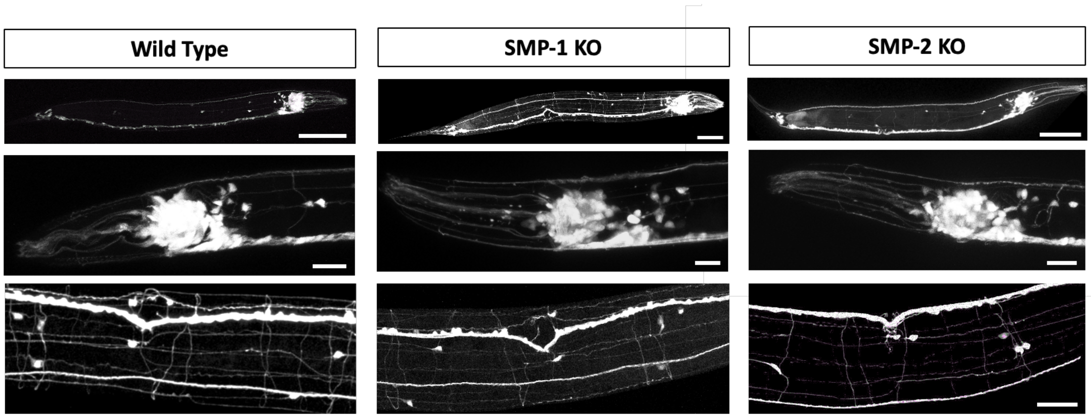

Figure 4.1 Neuronal morphology of membrane-bound semaphorins knockout strains is comparable to wild-type. The overall neural morphology (top) of semaphorin knockout animals expressing pan-neuronal GFP, as well as selected neuronal-rich areas (nose, middle; vulva, bottom) do not exhibit specific morphological abnormalities. In the vulva region, commissural axons and dendrites extend across from the ventral to the dorsal side of the animal. Scale bar (Whole animal) = 50 µm. Scale bar (vulva region) = 20 µm. Scale bar (nose region) = 10 µm.

4.3.2 Animals deficient in MAB-20 exhibited abnormal body morphology and axon guidance defects

I acquired images of *mab-20* null animals and observed that some had abnormal body morphology. Some presented elongated and thinner bodies; others had “bumps” or an enlarged posterior body (Figure 4.2 A-C). I surveyed 104 fixed animals (Figure 4.2 D); about half of the animals (62, 0.53, with Fisher Exact confidence interval of 95% CI= 0.09) presented no abnormal phenotype, while 36 animals (0.31, 95% CI= 0.88) presented an enlarged posterior body (Figure 4.2 A),13 animals (0.11, 95% CI= 0.07) had a thinner body than *wild-type* (Figure 4.2 B), I named them “skinny” ,and 7 animals (0.06, 95% CI= 0.06) presented a “corkscrew-like” VNC (Figure 4.2 C) comparable to the ones observed in mutant animals named “roller” that show cuticle defects that give the animal its helically shaped appearance (Cox et al., 1980). No animal presented more than one of these three phenotypes. Further, all animals with enlarged posterior or roller phenotype, exhibited axonal guidance defects with disorganized displaying disorganized neurites or abnormal motoneuron commissures (Figure 4.2 E).

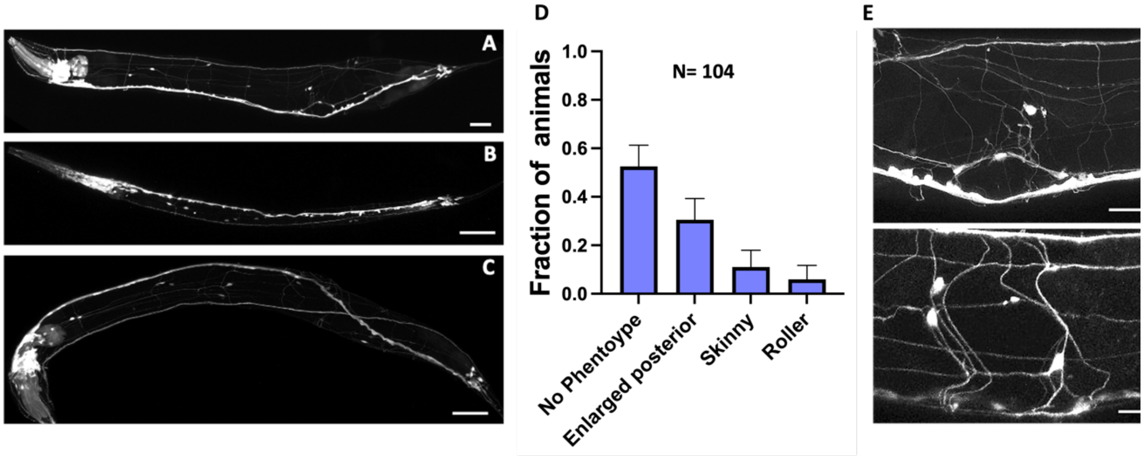

Figure 4.2 ***mab-20*** **knockout animals present several body morphology and axon guidance defects.** A) Animals with enlarged posterior. B) Animals with thinner bodies ("skinny"); C) Animals with "roller" (corkscrew VNC) body morphology. D) About half the animals did not present body morphology phenotypes and most of the others presented an enlarged posterior (N= 104 animals). E) Some animals with abnormal body morphology also presented abnormal motoneuron commissures or disorganized neurites. Scale bar A-C = 25 µm. Scale bar E= 10 µm

4.3.3 *mab-20* knockout animals showed increased neurite regeneration after laser microsurgery, SMP-1 and SMP-2 null animals' regeneration ability was comparable to Wild Type

I disconnected commissural neurites by laser microsurgery (Harreguy et al., 2021, 2022) and, 24 hours later, proceeded to image the injured neurites under a confocal microscope (Figure 4.3). At this timepoint, regenerating motoneurons should have formed an axonal growth cone and extended from the neuronal stump at the ventral side towards their targets on the dorsal side of the animal and, in some cases reconnect to the target (Ghosh-Roy & Chisholm, 2010; He & Jin, 2016; Sun et al., 2014).

Wild-type animals regrew 38/73 neurites (0.52, 95% CI=0.11) but only 5 neurites (0.07, 95% CI=0.083) reconnected (Harreguy et al., 2020; Harreguy et al. 2022). SMP-1 and SMP-2 deficient animals regrew and reconnected at rates similar to wild-type ($p >$

0.99, p= 0.668, respectively). In *smp-1* knockout animals, 10/19 (0.52 95% CI =± 0.20) disconnected neurites, regrew, and 3 (0.16 95% CI = 0.22) reconnected. Additionally, *smp-2* knockout animals regrew 18/31 (0.581 95% CI =0.155) neurites and only reconnected 4 (0.129 95% CI = 0.16; Figure 4.3 B-C).

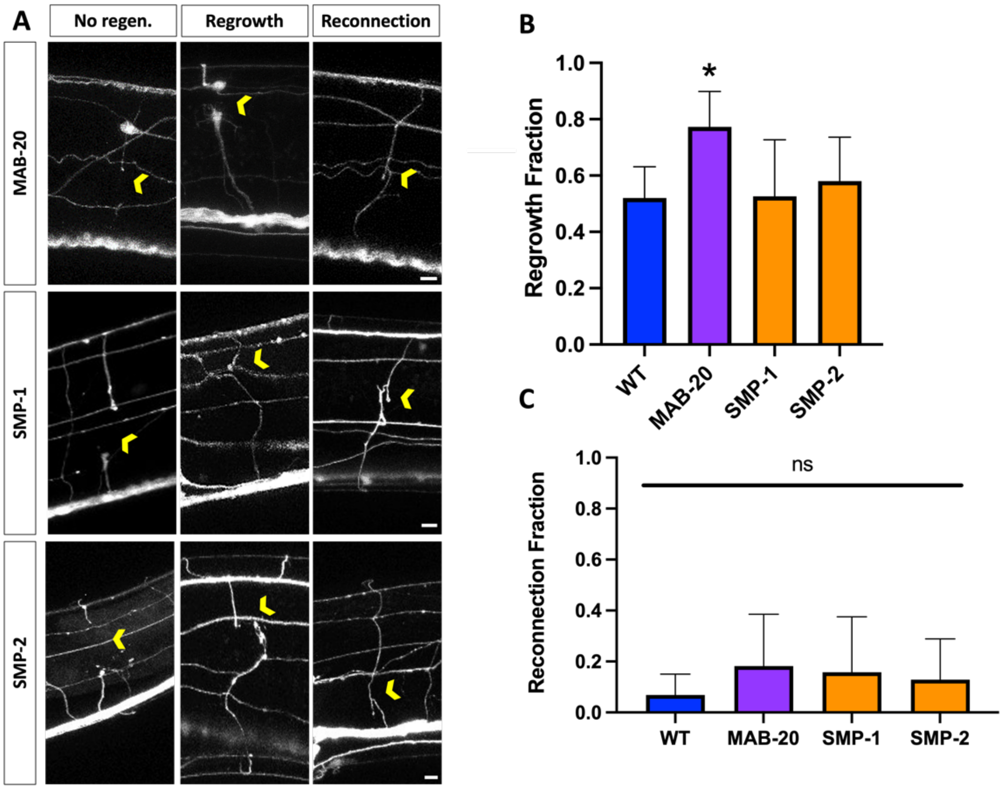

Figure 4.3. Neurite regeneration increases in *mab-20* but not in *smp-1* or *smp-2* knockout animals. A) Examples of no-regeneration, regrowth, and reconnection of neurites (left to right) in the three genotypes; yellow arrowhead indicates the injury site. Scale bar = 5 µm; B) More than half of neurites regenerated (combined regrew and reconnected). *mab-20 ko* animals regrew their neurites significantly more than WT; p = 0.048. Fisher Exact. C) There were no significant differences in regrowth and reconnection rates compared to WT (SMP-1: p= 0.336; SMP-2: p=0.447; MAB-20: p=- 0.435). Error bars are 95% CI.

MAB-20 knockout animals exhibited a significantly higher overall regeneration rate than the wild-type (p= 0.048), with 17/22 (0.77, 95% CI=0.126) neurites being able to regrow after the injury and 4 of those being able to reconnect (0.182 ± 0.203; Figure 4.3 B-C). Since these results were statistically significant from wild-type, I compared the regeneration ability of *mab-20* knockout to that of *plx-2* knockout animals (Figure 4.4, Chapter 3; (Harreguy et al., 2022)). No significant difference was observed with regard to overall regeneration ability (Figure 4.4 A; p=0.76, Fisher exact test). However, while *mab-*

20 knockouts regrew at a higher rate, *plx-2* knockout animals showed a greater reconnection ability (Figure 4.4 B; p= 0.002, Chi-square test).

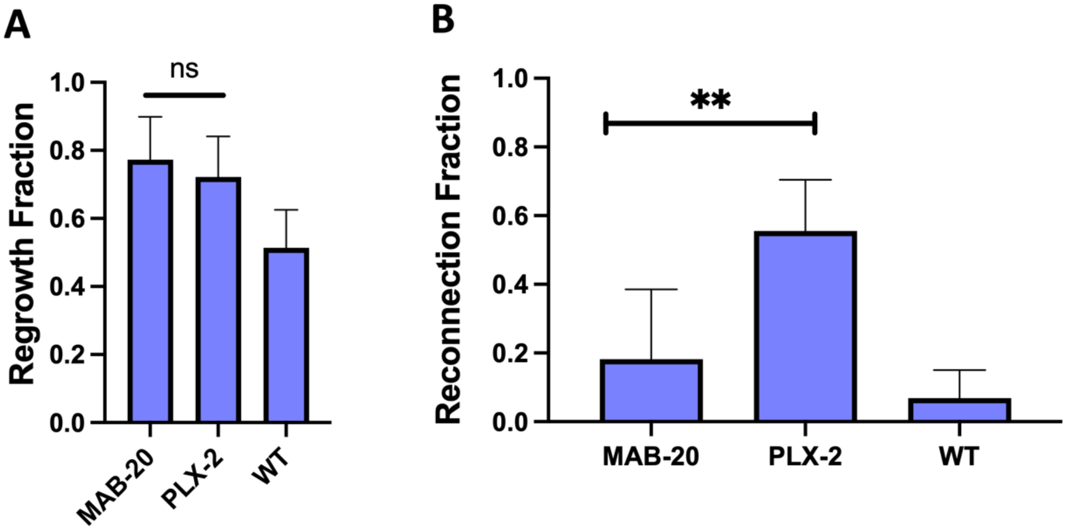

Figure 4.4 MAB-20 and PLX-2 deficient animals are able to regenerate their neurites at a similar rate, but PLX-2 null animals exhibit a higher reconnection rate. A) *mab-20* and *plx-2* knockout animals regenerate at a similar rate (p= 0.764, Fisher exact test). B) While *mab-20* knockout animals can regrow their neurites at a higher rate, *plx-2* knockout exhibit significantly higher reconnection (p= 0.002, 2x 3 table; Chi-square test).

4.4 Discussion

In this chapter, I have shown that out of the three semaphorins in *C. elegans*, only the secreted semaphorin, MAB-20, restricts neuronal regrowth and reconnection after injury.

MAB-20 signals through PLX-2, which I have previously described as being expressed in several motoneuronal types (Harreguy et al., 2022). Even though both knockout strains present the same regeneration ability of approximately 75%, *mab-20* knockout animals exhibited a disorganized regrowth with significantly fewer neurites reconnecting to their targets. This could be because MAB-20 is a strong chemorepellent and in its absence, neurites regrow in a highly disorganized manner without any guidance to find their target. In the absence of only PLX-2, MAB-20 could still act in a PLX-2-

independent manner (Nakao et al., 2007) and somewhat restrict aberrant growth. Similarly to our observation regarding regeneration, only *mab-20 knockout* animals present severe body morphology defects and aberrant axon guidance during development, also reported by (Roy et al., 2000).

On the other hand, neither SMP-1 nor SMP-2 alone had an effect on the regenerative ability of *C. elegans* motoneurons. My previous findings show that the SMP-1 and SMP-2 receptor, PLX-1, restricts regeneration, with 70% of injured neurites regenerating in its absence (Harreguy et al., 2022). These results suggest that SMP-1 and SMP-2 could have a redundant effect only observed when both signaling molecules are absent. A similarly redundant function for SMP-1 and SMP-2 was observed when evaluating developmental axon guidance defects in the M1 pharyngeal neuron (Refai et al., 2013). This effect could be further investigated in the *smp-1/smp-2* double knockout strain.

My results suggest a role for *C. elegans* semaphorins in neuronal regeneration that is similar to what has been suggested in mammalian systems (Cooke et al., 2022; Pasterkamp & Giger, 2009) where, similar to its role in neurodevelopment, regenerating axons avoid areas with high semaphorin concentration.

CHAPTER 5

GENERAL DISCUSSION AND FUTURE RESEARCH

5.1 Discussion

In this dissertation, I have described a novel laser microsurgery platform using a Yb-doped laser, which performs in a comparable manner to traditional Ti:Sapphire lasers but costs less, requires less maintenance, and is more robust as it can operate in a wide range of room humidity and temperature conditions. I used this laser microsurgery platform to conduct all the injury experiments described in Chapter 3 and 4. In these chapters, I investigated the role of all members of the *C. elegans* semaphorin pathway in neuronal regeneration.

C. elegans lacks glial cells around the VNC and does not display an immune response after injury. This simplicity allowed me to study the effects of the entire semaphorin pathway in the intrinsic cellular regenerative response at the single neuron level, which at this time is extremely difficult in mammals due to the complexity of their signaling pathways and their anatomy.

From studies performed in mice and other vertebrates, it is known that some semaphorins and their receptors increase expression following injury and that regeneration and recovery are improved in the presence of semaphorin inhibitors (De Winter et al., 2002; Kaneko et al., 2006; Kikuchi et al., 2003; Montolio et al., 2009) and, in a comparable manner to the role they play during neurodevelopment, regenerating axons avoid areas with high semaphorin concentration. I hypothesized that in a similar role, *C. elegans* semaphorins would act as restrictive cues that direct motoneuron regeneration to prevent aberrant growth and misconnections.

In Chapter 3, I showed that the receptor for membrane-bound semaphorins PLX-1 is not expressed in motoneurons but instead in body muscles. Since deletion of PLX-1 resulted in an increase in regrowth and reconnection, it is probably safe to assume that SMP-1 and or SMP-2 are expressed to some extent in motoneurons in the VNC. In addition, the fact that *C. elegans*' neuromuscular junctions are comprised of connections made between neurons which synapse onto muscle arms that protrude from body muscle (Altun & Hall, 2005a; Dixon & Roy, 2005) and that neurite growth always occurs from the direction of the cell body (in this case the VNC) towards the target muscle (Byrne & Hammarlund, 2017), could indicate that locally expressed PLX-1 in muscle is driving axon pathfinding and aiding axons expressing SMP-1 or SMP-2 to their correct targets. While during neurodevelopment, a correct balance of repulsive and attractive cues is required to aid extending axons find their targets, removing the repellant effects of the semaphorins in the adult, in this case by knocking out its receptor PLX-1, could result in increased regrowth and reconnection rates to target muscle after injury. However, the fact that this effect is not observed when only SMP-1 or SMP-2 are knocked out is indicative of a redundant role that needs to be further investigated in *smp-1/smp-2* double knockout animals.

In the case of the secreted semaphorin pathway, I observed that knocking down the secreted semaphorin MAB-20 or its receptor PLX-2 increased regeneration after injury. However, only animals deficient in PLX-2 were exhibited increase reconnection rates to the dorsal side of the animal, while MAB-20 knockout animals only showed increased axonal regrowth compared to WT. As previously discussed, there is evidence suggesting that MAB-20 acts in a PLX-2 independent way (Nakao et al., 2007; Roy et al., 2000).

I observed that after 24 hours, some of the neurons that seemed to have successfully reconnected to their target did so by navigating a slightly different “route” than the one the initial neuron had followed, while others were able to navigate across the injury site and find the distal part of the severed axon and fuse themselves back together. The process of axonal fusion in *C. elegans* has been widely reported (Neumann et al., 2011; Teoh et al., 2018), and even though some of the players regulating this process have been identified, there are still unknowns regarding how this mechanism works. Tying this information to the fact that PLX-2 knockout animals have higher reconnection rates, it is possible that secreted MAB-20 via PLX-2 is aiding this fusion mechanism in injured motoneurons by encapsulating the injury site and preventing the injured axon from diverting from its original route. In contrast, PLX-1 could play a more direct role in long-range target pathfinding instead of axonal fusion.

To assess the functional reconnection of the motoneurons to their muscle targets, I quantified the recovery of locomotion behavior after injury. However, this proved not to be the ideal parameter because 24 hours after injury, locomotion behavior has fully restored to pre-injury parameters in all knockout animals as well as the WT. While I have discussed possible reasons for these observations in Chapter 3 it is clear that locomotion behavior, or at least crawling speed and frequency, are not good parameters to assess functional regeneration due to the resiliency of the behavior whereas even in *Wild Type*, crawling speed and frequency are fully recovered, probably due to mechanisms of synaptic plasticity and remodeling like strengthening of existing connections or increase in synapses number or strength. Therefore, other parameters should be assessed, or new methods explored. For example, in lamprey, swimming behavior appears fully recovered after spinal cord injury, with injured lampreys swimming at comparable speeds to sham lampreys even though only 30%-70% of axons regrow. However, after further study, researchers found that the swimming kinematics of injured lamprey are indeed different as injured lamprey need higher body wave frequencies to swim at the same speed as control animals and that control animals have longer wavelengths and higher amplitude in their body undulation, showing that while the behavior outcome is seemingly the same, there are quantifiable differences between injured and control animals (Fies et al., 2021; Oliphint et al., 2010).

To conclude this section, I would like to set the semaphorins aside for a moment and just pose the question; Why do only some *C. elegans* neurons regenerate after injury? While it is known that some neuronal types have regenerative ability and some do not, identical neurons can respond in different ways to similar injury. In a widely conserved process from invertebrates to mammals, after axonal injury, there is an initial retraction of the axonal bulb and an increase in extracellular calcium. This calcium influx into the cell following injury is thought to aid in re-sealing the axonal stump, which is considered essential for the regeneration response. Following this step, regenerating axons will form a growth cone structure at the tip of the injured axon and begin the elongation process (Byrne & Hammarlund, 2017; Chen & Chisholm, 2011; He & Jin, 2016; C. C. Winter et al., 2022). There is evidence that neuronal calcium conditions at the time of injury or calcium sensitivity could determine the ability of the cell to initiate calcium-dependent repair processes. Further, calcium stimulates the production of cAMP by promoting adenylate cyclase activity, cAMP has also been shown to be essential for axonal regeneration of PLM neurons and to stimulate both the process of fusion as well as regrowth (Chen & Chisholm, 2011; Ghosh-Roy et al., 2010). In contrast, too much calcium can activate cell death pathways via different mechanisms suggesting that a tightly regulated calcium homeostasis is required (Ghosh-Roy et al., 2010; Khaitin, 2021; Ribas et al., 2017; Weber, 2012; Xu et al., 2001). I suggest a hypothesis in which variability in cytoplasmic calcium concentration, either from calcium influx or release from internal stores, that affects calcium homeostasis could be responsible for the stochastic regeneration observed between neurons of the same type.

Finally, it is important to mention that the mechanisms I have described throughout this dissertation operate in syntony in the complex environment of a live animal and that future research should focus on elucidating how these pathways interact, not only on whether the semaphorins or calcium might play a role in the same repair pathways but also the involvement of other axon guidance cues such as ephrins and netrins that work together during development to orchestrate the correct wiring of the nervous system.

5.2 Future Directions

I plan to create an *smp-1/smp-2* double null strain to conduct morphology and locomotion analysis and further injury experiments to understand the role of these semaphorins in regeneration. Further, to investigate whether mab-20 could be acting in a *plx-2* independent manner through the LAD- *2* receptor we have acquired a *LAD*-2 knockout strain, I will generate the *lad-2/plx-2* double null and conduct the same experiments as for the *smp-1/smp-2* knockout.

To better understand the semaphorin plexin interaction at the injury site, we will determine the expression patterns and distribution dynamics of the three semaphorins. I contacted colleagues that study the semaphorin system in *C. elegans* and received transgenic plasmids that drive expression of fluorescent-tagged SMP-1 and SMP-2 (*smp1p::smp1::gfp* and *smp2p::smp2::gfp* constructs, kind gifts from Kang Shen from Stanford University and Kota Mizumoto from the University of British Columbia), and we have contracted InVivo Biosystems (Eugene, Oregon) to modify the plasmids into transcriptional reporters and inject them into a strain that expresses the NeuroPAL system for identification of neuronal expression. We have the two transgenic lines that express GFP in cells that transcribe either *smp-1* and *smp-2* at hand. To determine the spatial distribution and dynamics of the three semaphorins before, during, and after injury, we designed three transgenic strains. In one strain, MAB-20 is tagged with a red fluorescent protein (*mab-20p*::*mab-20::WrmScarlet)*. In the other two, we use a split red fluorescent protein that only fluoresces when two parts are in proximity (*plx-1p::WrmScarlet*$_{1\text{-}10}$*::PLX-1*, *smp-1p::WrmScarlet*$_{11}$*::SMP-1* and *plx-1p::WrmScarlet*$_{1\text{-}10}$*::PLX-1*, *smp-2p::smp-2::WrmScarlet*$_{11}$*::SMP-2*). These strains will allow me to locate the sites of ligand-receptor interactions and track their spatiotemporal distribution in real-time.

5.3 Conclusion

Ramon y Cajal, armed with the finest microscopes of his time, meticulous preparation, and keen observations, demonstrated remarkable scientific acumen when he postulated that there must be inhibitory factors that impede axon regeneration in the CNS but not PNS. In our 21st century, scientists have successfully identified some of these CNS regeneration-inhibiting factors and use tools such as transgenics, modern microscopy, and *in vivo* studies to further explore the differences between the regenerative ability of the PNS and the restrictive CNS.

In this dissertation, I used *C. elegans* as a model to study at the neuronal level the effects of semaphorins in neuronal regeneration using a novel laser microsurgery platform and shown that semaphorins play a restrictive role in neuronal regrowth and reconnection after injury. As I and other researchers delve deeper into the mechanisms and factors involved in promoting regeneration, we may uncover valuable insights that could aid in overcoming the challenges faced by regenerative medicine in treating central nervous system injuries and disorders.

In the words of Cajal:*" In man affected by various nervous diseases and in young animals exposed to traumatisms we observed regenerative phenomena. It is true that such reactions are ephemeral, aborted, and purposeless, but although unspecific they merit careful study. No matter what their significance, these productions have a positive biological interest"* (Lobato, 2008).

APPENDIX A

NEURONAL MICROSURGERY WITH AN YB-DOPED FIBER FEMTOSECOND LASER

Originally published in *C. elegans Methods and Applications*:

Harreguy, M. B., Tran, T. S., & Haspel, G. (2021). Neuronal microsurgery with an Yb-doped fiber femtosecond laser. In *C. elegans Methods and Applications.* (3rd ed.). Springer Nature. https://doi.org/10.1007/978-1-0716-2180-6_17

A.1 Introduction

Ablation of cells or cell parts such as nerve fibers with a laser microbeam has proven to be a useful tool to address questions of necessity and regeneration in multiple fields. Laser microsurgery has been widely used in *C. elegans* since it was first described by John White (Sulston & White, 1980) in 1980 and was instrumental in multiple discoveries such as details of cell–cell interactions (Sulston & White, 1980), the elucidation of the touch sensitivity circuit (Chalfie et al., 1985), and the role of GABA in *C. elegans* nervous system (McIntire et al., 1993). More recently, in 2004, Yanik (Yanik et al., 2004) showed that some *C. elegans* axons are capable of regenerating, which established *C. elegans* as a model for regeneration studies. Further, the technique can also help identify specific behaviors associated with injury in addition to providing insight about factors that affect regeneration (DiLoreto et al., 2019; Fang-Yen et al., 2012).

Laser microsurgery platforms have evolved significantly since the 1980s, most modern laser ablation platforms are one of two kinds, either nanosecond or femtosecond lasers (Haspel et al., 2020). Nanosecond lasers are more suited for cell ablation experiments while femtosecond lasers can be used for both cell ablation and axotomy as they can be adjusted to generate large areas of damage or to be precise and dissect subcellular structures as the laser beam can be focused onto a point in the sample with minimal damage to surrounding tissues (Vogel et al., 2005). This difference is mainly due to the million-fold decrease in pulse width increasing the required energy per pulse by the same ratio. While femtosecond laser pulses are typically in the order of tens of nanojoules (nJ), nanosecond pulses are usually in the order of tens of millijoules (mJ). Because excess energy diffuses away from the injury spot, nanosecond-long pulses generate more damage surrounding the injury (Fang-Yen et al., 2012).

Most commonly used femtosecond lasers in the field are Ti:Sapphire lasers which produce near-infrared (NIR) pulses with energies up to 50 nJ, a center wavelength of approximately 800 nm, pulse duration of 100–200 femtoseconds, and repetition rates of 80 MHz (Gattass et al., 2006). However, Ti:Sapphire lasers need constant maintenance, are very susceptible to room environmental conditions such as high humidity and tend to have a very high cost. In this chapter, we describe how to assemble and operate a laser microsurgery platform using an Yb-doped fiber laser. The advantages of this type of laser are higher possible power, lower maintenance, smaller footprint, and air cooling (Harreguy et al., 2020).

The specific Yb-fiber system described here (BlueCut, Menlo Systems GmbH, Germany) which generates ~400 fs pulses in the infrared (1030 nm) includes an internal pulse picker which simplifies setup and lowers the overall cost compared to Ti:Sapphire systems that require an external pulse picker. Further, Yb-fiber system can ablate with user-defined repetition rate of single shot to 50 MHz and pulse energies of nJ to μJ. We have recently demonstrated that our novel setup shows comparable microsurgery results to those obtained with the Ti: Sapphire systems (Harreguy et al., 2020) without its disadvantages.

A.2 Materials

A.2.1 Microscope assembly

1. Yb-fiber system (BlueCut, Menlo Systems GmbH, Germany).

2. 4 circular mirrors: 2 for alignment and 2 for periscope.

3. Optical rails and base.

4. Achromatic Galilean beam expander, AR coated: 650–1050 nm (can be replaced by a Galilean pair and optical rails).

5. Microscope (e.g., RAMM conFigure d by Applied Scientific Instrumentation).

6. High NA objective with high IR transmission (e.g., Olympus UAPO 40, 1.35 NA).

7. Immersion oil.

8. 750 nm long-pass dichroic mirror.

9. Dichroic mirror cube holder.

10. sCMOS Camera (e.g., Flash4.0, Hamamatsu).

11. IR cut-off filter (that prevents 1030 nm from hitting camera, e.g., Chroma ET750sp 2p8).

12. LED light source (e.g., LED 120, X-cite).

13. Passive optical table.

14. Power and energy meter console with s170c microscope slide power sensor.

15. NIR detector card (VRC4, Thorlabs).

16. Alignment plate.

17. Laser safety goggles for 1030 nm.

18. Beam blockers.

A.2.2 Laser microsurgery

1. Immobilization Solution: Pluronic F127 36% (see Note 1), Tetramisole 1 μM (or similar anesthetic).

2. #1 Rectangular microscopy coverslips.

3. Dissection microscope.

4. 60 mm petri dishes for strain maintenance.

5. NGM-Agar: (Stiernagle, 2006) 3 g of NaCl, 2.5 g of peptone,20 g of agar,1 mL of cholesterol (5 mg/mL in ethanol), 1 mL of 1 M CaCl2, 1 mL of 1 M MgSO4, and 25 mL of 1 M (pH 6.0) KPO4 to prepare 1 L.

6. OP-50-1 bacteria (GCG).

7. Transgenic *C. elegans* strain (e.g., NW1229 pan-neuronal GFP expression, CGC).

A.3 Methods

A.3.1 Laser safety

Lasers are dangerous and should always be operated with caution. This laser is a class 4 laser which means it is hazardous for eye exposure and that it can burn through skin and some materials at close range and should be handled with extreme care. Always use the minimal energy and number of pulses that produce the required lesion. Before using the laser, it is very important to receive laser safety training. The laser manufacturer can provide further guidance.

In addition, beam blockers should always be in place even when the laser is off and only removed when performing experiments. When the laser is on, safety goggles should be worn at all times and the user's hands should be free of any reflective surfaces such as jewelry or watches. "Laser in use" signs should be displayed on the door outside the room where the laser is set up to prevent people without appropriate protection from coming in.

A.3.2 Microscope and laser setup (Figure A.1)

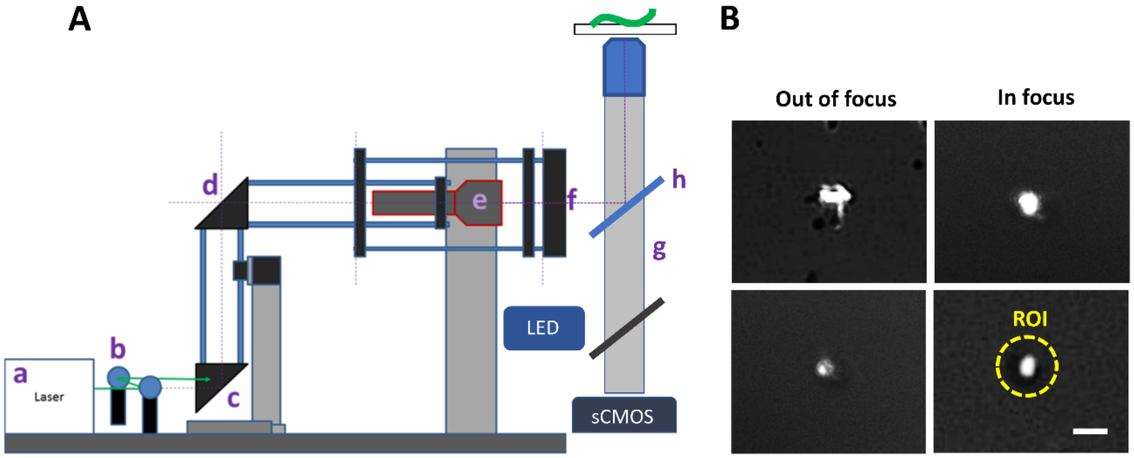

Figure A.1 Laser setup and alignment. A) Laser setup. BlueCut laser source (a) is fastened to an optical table. The beam is directed in free space to aligning mirrors (b), a pair of periscope mirrors (c and d), and a beam expander (e), to fill the back focal aperture (f) of the microscope (g) and onto the dichroic mirror (h). B) Black Slide test. The laser damage spot should be circular and the focus of the microscope is adjusted in order to get defined and crisp edges. A circular region of interest is selected with the white lesion in its center. Scale bar =5 µm

1. Set up optical table and secure the laser system so that the beam is aligned with the center of the table.

2. Secure all connection between the laser console, the AOM seed, and the computer, and make sure that no cables are in the path of the laser beam.

3. Set up the microscope, the LED fluorescent light source, and the camera at the other end of the table (see Note 2).

4. Install the IR cut-off filter to avoid damage to the camera.

5. Assemble the periscope and align it to direct the laser through the beam expander into the back focal plane of the microscope at the side of the filter cube.

6. Turn the laser on at a very low power setting and in continuous mode and use the NIR Detector Card to observe the path of the laser beam. Secure the small circular mirrors to the table so that their configuration allows to direct the beam (hitting the center of each mirror) to the center of the lower periscope mirror (see Note 3).

7. Adjust the angle of the lower periscope mirror to center the laser beam on the upper periscope mirror.

8. Set up the dichroic mirror in the dichroic mirror cube holder (see Note 4).

9. Attach the dichroic mirror to the top of the microscope's fluorescent filter turret.

10. Using the optical rails from the periscope attach the beam expander so that the beam expander optics are close to the back focal opening of the microscope.

11. Turn the laser in a low power setting again and using the NIR card adjust the iris on the beam expander so that the entire back focal aperture of the microscope is illuminated.

12. Proceed with alignment procedures.

A.3.3 Laser alignment

Alignment is probably the most dangerous process when working with a laser as the user is adjusting, moving mirrors and introducing objects in the laser beam path. Please read subheading A.3.1 before starting alignment (see Notes 5 and 6).

A.3.3.1 Alignment process

1. Turn on the laser in continuous mode at a low power setting and using the NIR card adjust the circular mirrors to hit the center of each mirror, starting from the one closest to the laser and up to the upper periscope mirror.

2. Use the alignment knobs and the alignment plate, placed on the rails between the periscope mirror and the beam expander, to adjust the mirrors further so that the laser beam is exactly at the center of the optical frame before the beam expander. Move the beam with the lower mirror when the plate is farthest from the microscope, and with the upper mirror when it is closer to the microscope.

3. You might need to repeat steps 1 and 2 several times as adjusting one mirror might alter where the laser hits other mirrors.

4. Adjust the beam expander so that the back focal aperture of the microscope is fully illuminated. The expanded beam should be as collimated as possible. You can test this by removing the microscope and verifying that the shape and size of the expanded beam does not change over some distance.

5. Proceed to fine alignment using the "Black ink slide" test (see Subheading A.3.3.2) with the laser to pulse mode.

6. After optimal alignment has been reached, measure laser power with the power meter and record the number. Measuring power before every experiment is a good practice and can also help determine if the laser needs alignment.

A.3.3.2 Fine alignment test: “Black Ink Slide”

1. Cover a #1 rectangular coverslip in black ink using a black permanent marker and allow the ink to dry for a few minutes.

2. Place the coverslip under the microscope with the ink side facing away from the objective and focus on it. Use immersion oil for the high NA objective and use the microscope in Kohler aligned brightfield mode (see Note 7).

3. Starting with a low power setting fire the laser and keep increasing power until a white spot is visible on the slide.

4. Keep doing this and adjust the microscope focus and the setting of the beam expander until the white spot is the smallest possible size, looks circular, and has defined and crisp edges (Figure B.1B).

5. To be able to aim the laser for microsurgery, use ImageJ to draw a circular Region of Interest (ROI), with the laser spot in the center of the circle and save the ROI so it is easily available (Figure B.1B; see Note 8).

A.3.4. Laser microsurgery

1. On the day before performing the laser microsurgery, pick animals of the desired age and transfer them onto a new, seeded NGM plate (see Note 9).

2. Before starting the experiment turn the laser on, make sure everything is working appropriately, perform the black ink slide test, open the saved ROI, and adjust it if needed (see Subheading B.3.3.2).

3. Fill a bucket with ice and place an empty tip-box lid on top of the ice making sure the flat surface is level.

4. Mix Pluronic F127 36% solution with enough concentrated Tetramisole (1mMsolution to dilute to 1μM Tetramisole) in a 1.5 ml tube and keep the tube in ice (see Note 10).

5. Place #1 rectangular coverslip on top of the tip box and wait a minute until the surface of the coverslip is cold, add 25 μL of the Pluronic + Tetramisole mixture to the coverslip surface (see Note 11).

6. With a pick transfer the animals onto the drop of Pluronic +Tetramisole mixture and gently press another coverslip on top until the liquid between the coverslips is evenly spread (see Note 12).

7. Remove the coverslip from the ice and wait until the liquid mixture becomes solid or the glass does not feel cold to the touch anymore.

8. Using a dissection microscope make sure that the animals are present between the coverslips and that the animals are healthy (see Note 13).

9. Place the coverslip in the microscope and secure it as if it were a slide (see Note 14).

10. Using the microscope software and adjusting the focus, find the target neuron or cell (see Note 15).

11. Once you locate the target cell, select the injury spot by placing it in the middle of the ROI.

12. Put on the laser safety goggles, remove the beam blocker from the laser opening, and press the pulse key to fire the laser. The injury should be immediately visible. If the injury is not visible, increase laser power slightly and try again (see Note 16).

13. Take before and after images of the injury site (Figure A.2A).

14. After all the desired cells have been injured, remove the coverslip from under the microscope and move it back on the ice.

15. After 5 min on the ice slowly separate both coverslips being careful not to break them. Once both sides are separated, place them under the dissection microscope to find the animals.

16. With a pick carefully remove the animals from the Pluronic + Tetramisole mixture which should have the consistency of a gel and place them into individual NGM plates.

17. After 24 h or the desired time for your experiment, repeat steps 2–9 to mount the animals between two coverslips again and image the injury site (Figure A.2A).

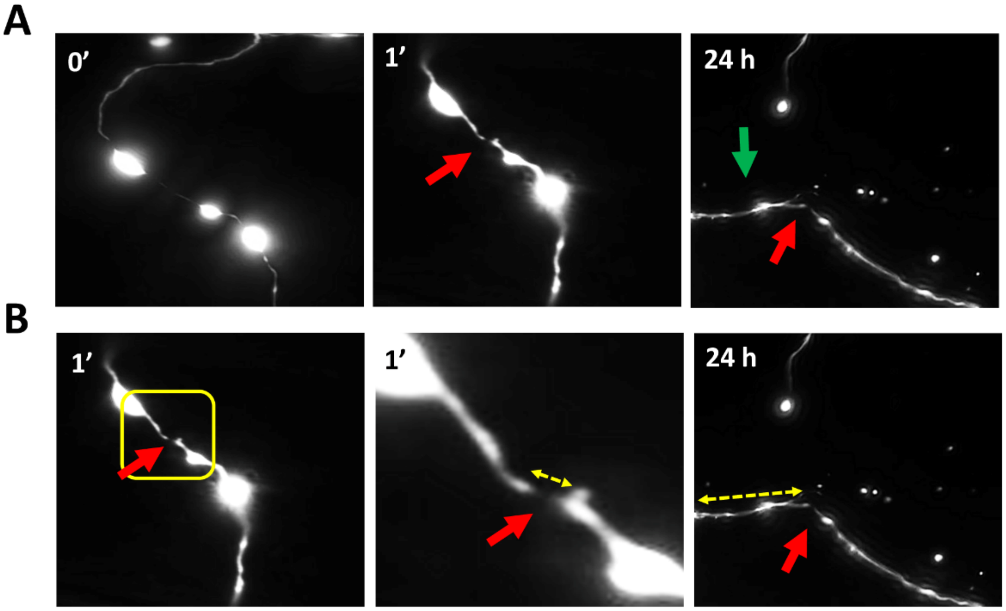

Figure A.2 *C. elegans* neurites regrow following microsurgery with an Yb-doped fiber laser. A) *C. elegans* axotomy. Commissures of GABAergic (D type) motoneurons injured in immobilized animals were found again on the next day to assess regeneration. Arrows indicate the sites of axotomy (red arrow) and regenerating branch (green arrow). B) Example of measuring the sizes of the injury size and outgrowth. Size of injury is measured between the two retracting branches. Outgrowth is measured from the site of injury to the tip of the regenerated branch. Scale = 10 µm

A.3.5 Data analysis

1. The specific assay and statistical test depends on your scientific question. For example, you can score the number of neurons that regenerated or cells that survived by looking at images taken 24 or 48 h after injury. In that case, a Fisher's Exact test is appropriate.

2. For continuous values, such as extent of neurite regeneration, measure the initial injury size as well as outgrowth with a software such as FIJI (is just ImageJ v.1.53c (Schindelin et al., 2012; Schneider et al., 2012); Figure A.2B; see Note 17). In this case, we suggest to visualize the data in shared-control Gardner–Altman plots, and to calculate the p-value by two-sided permutation t-test (Estimation Statistics;(Ho et al., 2019)), or to compare among treatment groups with an ANOVA test.

A.4 Notes

1. Mix Pluronic F127 to 36% in deionized water by gradually adding the powder to a solution kept at 4 C and stirred continuously. This can take a few hours. Do not let the solution warm up because it will solidify. Aliquot and keep at 4°C. Prepare a concentrated Tetramisole 1 mM solution and use the Pluronic F127 36% solution to dilute to 1 μM.

2. We prefer a custom-made microscope without eyepieces for the obvious safety advantage. The suggested platform can be set up with any epifluorescence microscope that can accommodate a second dichroic mirror in its light path.

3. The laser beam should always hit the center of every mirror.

4. The dichroic mounting adapter directs the laser beam into the objective lens without interfering with the normal optical paths of the microscope.

5. For safety and efficiency reasons, we recommend that two people align the laser.

6. It is not reasonable to try and comprehensively cover laser alignment in this chapter. Your institution might have laboratories that are proficient in laser alignment or you could ask the vendor for advice.

7. Scoring a line or a grid on the ink with a sharp object might help with focusing.

8. The location of the ROI might need to be adjusted or at least checked with a black ink slide before every experiment.

9. For adult axotomy pick L4s the day before, it is easier to perform axotomy when the animal has few or no eggs.

10. It is very important to make and keep the Pluronic F127 36% solution at 4C or below as it will become solid at room temperature.

11. Try to avoid bubbles.

12. Four to five animals per coverslip works best.

13. You can use a thin permanent marker to draw a circle around each animal to make it easier to find under the microscope. You will use immersion oil so mark the coverslip that will be away from the objective and draw large circles.

14. If needed, you can place the coverslips on a glass slide. Mounting the animals between two coverslips allows optical access from either side of the animal more easily. We routinely lesion commissure neurites on the far side of the animal but they can end up closer to one coverslip or the other.

15. If epifluorescence is necessary to find the target cell, keep the shutter open as little as possible to avoid bleaching.

16. Always begin with a low laser power and slowly increase it until the injury is visible.

17. In case there is more than one branch in the regenerated neurite, sum the values.

APPENDIX B

A LOW POWER FLEXIBLE DIELECTRIC BARRIER DISCHARGE DISINFECTS SURFACES AND IMPROVES THE ACTION OF HYDROGEN PEROXIDE

Originally published in *Scientific Reports*:

Gershman, S., **Harreguy, M. B**., Yatom, S., Raitses, Y., Efthimion, P., & Haspel, G. (2021). A low power flexible dielectric barrier discharge disinfects surfaces and improves the action of hydrogen peroxide. *Scientific reports*, *11*(1), 4626.

B.1 Introduction

There is an urgent need for wide use of sanitizing and disinfecting agents and techniques. Brought into focus by the current COVID-19 pandemic, it is no longer limited to medical, pharmaceutical, or food industry, but rather expanded to the decontamination of commonly used surfaces such as doorknobs and devices, such as masks, cell phones, and pens. Over the last two decades, cold atmospheric pressure plasmas (CAP) have seen rapid development in the areas of bacterial and viral inactivation and surface disinfection (Aboubakr et al., 2018; Bekeschus et al., 2020; Boekema et al., 2015; Guo et al., 2018; Joshi et al., 2011; Laroussi, 2002, 2005; Sakudo et al., 2019). A recent review summarizes the achievements of a broad range of CAP plasma sources, including dielectric barrier discharges (DBD), that effectively inactivate bacteria, viruses, fungi, and bacterial spores. In spite of these achievements, the only sterilization method that involves plasma, which is currently recommended by the Centers for Disease Control and widely accepted in industry, is based on plasma activation of hydrogen peroxide vapor, one of the most effective (Cummings A.I & Childers R.W, 1990). Hydrogen peroxide does not leave any dangerous residue because its decomposition products are water and oxygen. Here, we investigate the synergistic action of hydrogen peroxide and CAP implemented for the first time in a flexible device suitable for personal use and able to treat curved surfaces. We demonstrate faster disinfection than plasma or hydrogen peroxide alone in stable low power operation.

The disinfecting and even sterilization effectiveness of plasmas is due to their bio active properties such as reactive oxygen (ROS) and nitrogen species (RNS), electrons, currents, electric and electromagnetic fields, and UV rays (Bauer & Graves, 2016; Lu et al., 2016; Verlackt et al., 2018). The mechanisms of bacterial inactivation have been investigated by many groups but remain unclear. The chemical and electrical plasma properties may be affecting a bacterial cell in stages. The electrons and the electric field affect the cell membrane and aid in the cell penetration by the RNSs and some long-lived ROSs. ROS are involved in lipid peroxidation and other oxidative reactions damaging the cell membrane and aiding the transport of RNS/ROS into the cell. Inside the cell the ROS/RNS damage proteins, lipids, and the DNA. The combined effect of these processes is bacterial cell inactivation (Bekeschus et al., 2019; Sakudo et al., 2019).

Most of the work on medical and biological applications of DBDs has been conducted on one of three configurations, a floating electrode configuration, a plasma jet (floating electrode or two electrode), and a less common surface DBD (Brandenburg, 2017; Eto et al., 2008; Fridman et al., 2006; Gorbanev et al., 2019; Laroussi & Akan, 2007; Pons et al., 2005; Sakudo et al., 2019; Winter et al., 2015; Xie et al., 2017). In a floating electrode device, the high voltage electrode is encased in a dielectric material and the treated surface acts as a ground electrode (Brandenburg, 2017; Fridman et al., 2006; Sakudo et al., 2019); the treated surface is exposed to high electric fields and fluxes of charged particles. The most extensively studied is the plasma jet, which uses power from pulsed dc to microwave range and where plasma effluent is carried by a gas flow to the treated surface. The plasma effluent is suitable for medical applications but requires a compressed gas supply (Brandenburg, 2017; Gorbanev et al., 2019; Laroussi & Akan, 2007; Winter et al., 2015). Surface DBD has been primarily studied as an actuator for flow control in aeronautics applications and for large area surface modifications (ex.(Pons et al., 2005)). Introduction of devices based on flexible printed circuit design facilitated its applications in medical and biological fields (Boekema et al., 2015; Eto et al., 2008; Kim et al., 2018; Pai et al., 2018; Xie et al., 2017). The device studied here is also based on a flexible printed circuit design.

Atmospheric pressure plasmas have been shown to be effective for the decontamination of surfaces from bacteria and viruses, but the level and the rate of inactivation strongly depend on the biological species, experimental conditions, and the plasma source. For example, D-value (time for 1log10 reduction) is 225 s for the exposure to the gases produced by one DBD (Pavlovich et al., 2014), 150 s for another DBD (Laroussi, 2002), 35 s for *E. coli* exposed to an atmospheric pressure helium/air glow discharge (Laroussi, 2005) , and 15 s for a paper-DBD (Xie et al., 2017). The fast reduction D = 15 s was achieved by a single-use flexible DBD device using a printed patterned electrode on a paper substrate and operated at 2 kHz, 3.5 kV AC, 10 W. This is a disposable device (Xie et al., 2017). This diversity of results and conditions makes it necessary for us to test the new device design presented here and quantify the disinfection of standard microorganisms.

Another variation on plasma disinfection is the use of low-pressure plasma activated hydrogen peroxide vapor (Bekeschus et al., 2019; Crow & Smith, 1995; Krebs et al., 1998). Systems such as the low temperature sterilization systems by Sterlis Healthcare

(Cummings A.I & Childers R.W, 1990) are widely accepted methods of sterilization of materials susceptible to high temperatures, humidity, and corrosion. In more recent studies, the addition of hydrogen peroxide has been explored to enhance plasma disinfection at atmospheric pressure (Golkowski et al., 2012; Govaert et al., 2019; Kahnert et al., 2005; Yamamoto et al., 2002). Addition of H_2O_2 droplets into a corona discharge produced 6log10 reduction, and adding H_2O_2 vapor to the plasma effluent produced a reduction greater than 6log10 in the bacterial load and a significant reduction in biofilm and spores (Govaert et al., 2019; Kahnert et al., 2005; Yamamoto et al., 2002). The dominant mechanisms responsible for the enhancement depend on the type of plasma, the state of H_2O_2. H_2O_2 vapor is ionized in a plasma to form H_2O_2-, while droplets may be negatively charged, a water solution of H_2O_2 is subject to the active species introduced by plasma into the solution akin to plasma activated water. Pure water is acidified by plasma enhancing the bactericidal effects, while buffered solutions such as phosphate buffer saline (PBS) maintain the pH level but are affected by the dissolved ozone, nitrates, (Bruggeman et al., 2016; Bruggeman & Leys, 2009; Traylor et al., 2011).

The flex-DBD described here is safe to the touch, but unlike plasma jet devices, it does not need any additional gas supply or sophisticated power sources, and unlike a paper-DBD device it is capable of long-term stable operation. We demonstrate a fast disinfection effect of over 4log10 in less than 90 s on the standard bacteria, gram-negative *Escherichia coli* (*E. coli*). We also demonstrate the synergistic effect of the commonly available antiseptic, 3% H_2O_2, and the flex-DBD device, of surface decontamination > 6log10 in 90s. The device tested here could be used to disinfect surfaces, personal items, and protection equipment such as masks.

B.2 Methods

B.2.1 Device assembly and electrical diagnostics

The flex-DBD is based on a printed circuit design (Boekema et al., 2015; Kim et al., 2018; Xie et al., 2017). It consists of a layer of copper tape (0.127 mm thick, 16 mm × 26 mm) serving as a high voltage electrode and covered by a layer of Kapton polyimide tape (Kapton, DuPont), 100 μm thick, ∊rel ≈ 3.5, and a patterned ground electrode, copper (30 μm thick), electroless nickel immersion gold (ENIG) coated placed on top of the Kapton polyimide tape (Figure C.1A). The pattern on the ground electrode consists of 200 (10 × 20) square cavities, each 0.75 × 0.75 mm in size.

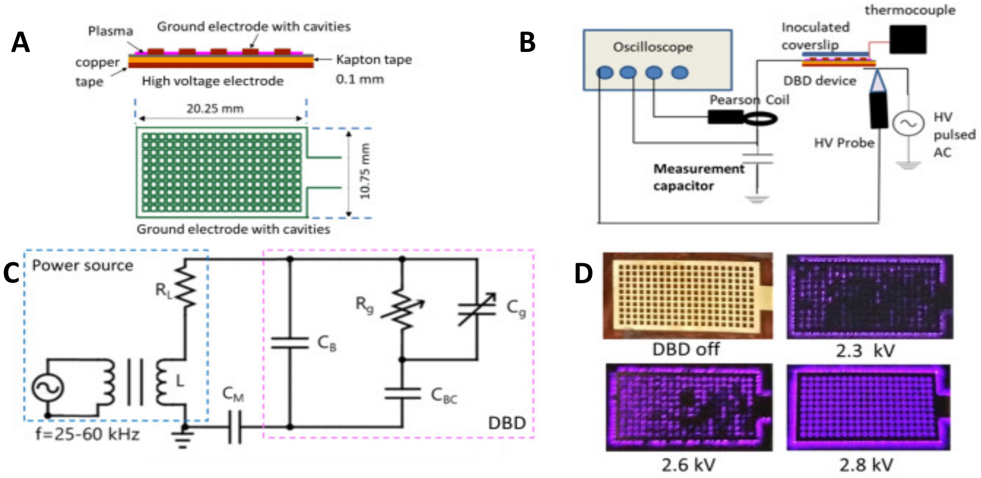

Figure B.1 The flex-DBD is based on a printed circuit design and operates at < 3 kV, ~ 40 kHz, < 0.5 W/cm2 supplied by a portable power source. A) The design of flex-DBD consists of conducting (copper) and insulating (polyimide) layers and a patterned ground electrode. B) The experimental setup includes a portable pulsed ac high voltage (HV) source and monitoring apparatus (oscilloscope). The patterned electrode and HV source are globally grounded. A coverslip inoculated with a bacteria sample is placed on top of the ground electrode. C) The equivalent circuit, where CB is the capacitance of the flex-DBD device excluding the rectangular cavities, CBC is the capacitance of the solid portion and Cg and Rg are the capacitance and resistance of the open-air portion of the cavities, CM is the measurement capacitor, and L and RL are the inductance and the resistance of the secondary coil of the high voltage transformer of the high frequency power source. (dD As the applied voltage increases, a greater part of the surface of flex-DBD lights up).

A regulated, 500 V–10 kV, 25–60 kHz, pulsed AC power source (PVM 500 AC, Information Unlimited) was used to generate the discharge (Figure B.1B). The patterned electrode of the flex-DBD was connected to the power-supply ground, and the copper foil electrode to the power-supply high voltage output transformer (Figure B.1B,C). We used a Tektronix D (2 GS/s, 250 MHz) oscilloscope to monitor the current, voltage, and charge transfer in the circuit during experiments: current to ground (Pearson Model 2877 Current Monitor, 1 V/A, 2 ns rise time); voltage at the high voltage (copper tape) electrode (Tektronix P6015 HV probe); and charge transferred was determined by measuring the voltage across a 10 nF capacitor (CM, Figure B.1B,C) connected in series on the ground side of the flex-DBD.

We operated the flex-DBD in resonance mode. The parallel connection between the DBD and the secondary coil on the high voltage output transformer has a resonance frequency, $\approx 12\pi LC\surd$, where L, is the inductance of the secondary (Figure B.1C) and C is the capacitance of the flex-DBD. During operation the capacitance of the flex-DBD is approximately, $C \approx CB + CBC$. At the resonance frequency, the overall impedance of the L-C circuit as seen by the power source is at a maximum, therefore minimizing the current drawn and hence the power used by the device (Figure B.1C) and maximizing the voltage applied to the DBD, hence facilitating a discharge at lower power used by the power source. To start the device, we adjusted the frequency to a resonance value at a voltage amplitude below the starting voltage, then increased the applied voltage to the start the discharge (Vstart = 1.9 kV amplitude) and readjusted the frequency to a new resonance value for the flex-DBD with the plasma on (Figure B.1D). The voltage was then increased until the entire surface of the flex-DBD appeared to glow to the naked eye (Figure B.1D, 2.8 kV). The resonance operating frequency was 42 ± 2 kHz. The variation in the resonance frequency is likely due to the slight differences in the hand-made devices and the operating conditions. We monitored the temperature of the grounded glowing face of the flex-DBD for several minutes prior to starting experiments to ensure that a steady-state condition was reached, and continued to monitor the temperature during experiments. Voltage amplitude and duty cycle were adjusted to maintain the temperature below 50 °C in steady-state operation. Except for the low power trial at 2 kV, the disinfection experiments were conducted with a voltage amplitude of 3 kV, a displacement current amplitude of 50 mA, a duty cycle of ~ 20%, and pulse repetition rate of 1 kHz. The voltage, current, and charge measurements were conducted during the sterilization experiments.

B.2.2 Sterilization efficiency experiments

To demonstrate the disinfection ability of the flex-DBD, we tested the effectiveness of the device in reducing the bacterial load of *E. coli* 10-beta (New England Biolabs) and the standard *E. coli* AMS 198 (ATCC-11229). Bacteria were cultured following vendor's instructions at 37 °C in Luria broth or Luria broth agar (both from Research Products International). For the surface test experiments, we used a suspension of the *E. coli* strain (OP-50-GFP, Caenorhabditis Genetics Center) that expresses cytoplasmic green fluorescent protein and forms a uniform bacterial lawn rather than discrete colonies. The flex-DBD was attached to a holder, or in other experiments, to the lid of a 60 mm petri dish (Figure B.2A). The experiments included the treatment of bacteria seeded in petri dishes, on a disposable textile type material, on metal (aluminum), and on glass (microscope cover slips). For treatment of bacterial plates, we spread 50 µl of a fresh bacteria culture on LB-agar plates and treated the plate surface with the flex-DBD attached to a lid, placed over the petri dish (Figure B.2A), for different amounts of time. We then incubated the plates overnight at 37 °C and visually compared them to untreated control and examined for areas that were clear of bacteria. To test the disinfection of the textile-type surfaces, 100 µl of *E. coli* OP-50 was spread on textile-like polyethylene material (Tyvek, DuPont). The petri dish cover with the flex-DBD attached was placed over the inoculated area. The petri dish cover used in this experiment was cut to maintain a 1–2 mm distance between the treated surface and the face of the flex-DBD. Each region was treated for a set amount of time and at the end of the treatment time, immediately stamped with an LB contact plate (Carolina

Biological Supply Company). The untreated area was stamped as the control. The contact plates were incubated for 24 h at 37 °C. Qualitative results were assessed visually by observing GFP expression using a gel imaging station (FastGene Blue/Green LED GelPic Box, Nippon Genetics).

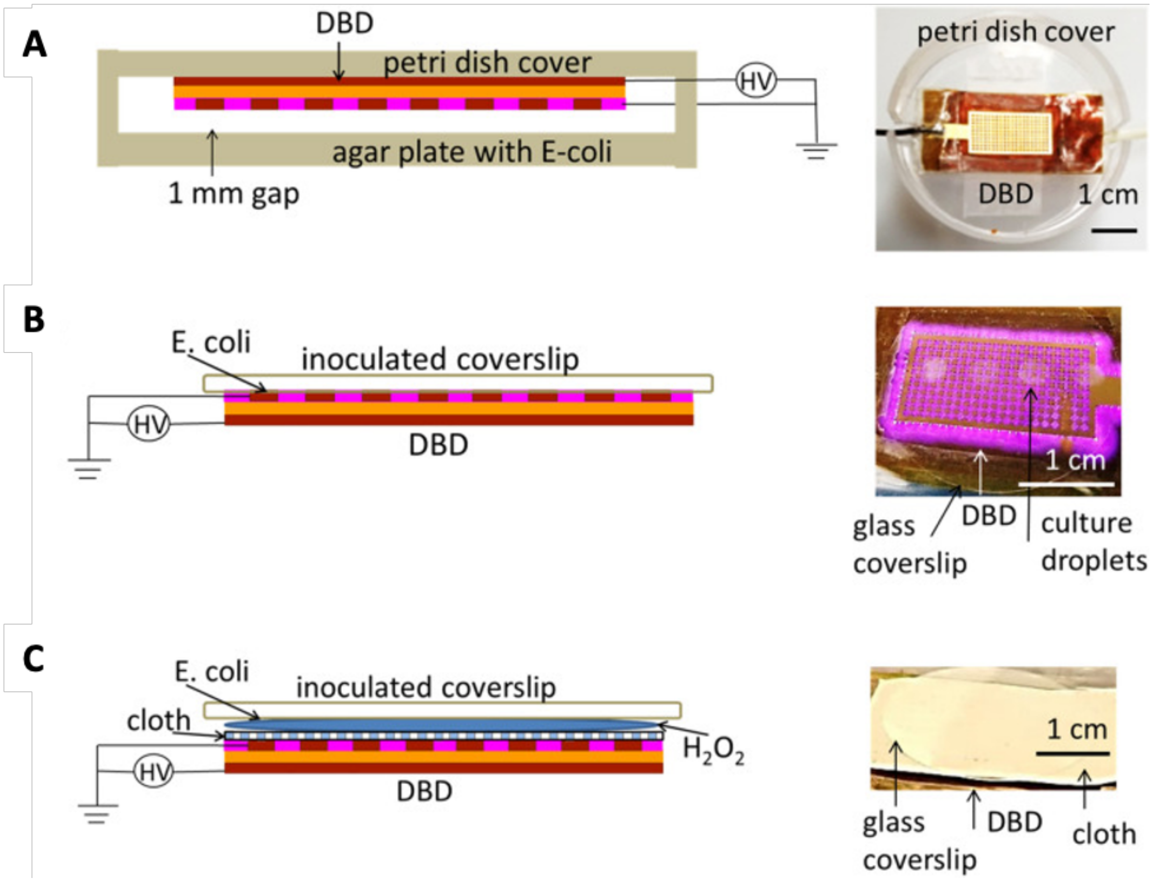

Figure B.2 Flex-DBD at a short distance, in contact with a surface, or with a liquid disinfectant. A) The flex-DBD is fixed to the inside of a petri dish lid. B) Inoculated coverslip is directly in contact with the flex-DBD. C) The flex-DBD is covered by a semi-permeable cloth with a liquid disinfectant on top; the inoculated cover slip is placed so that the bacterial culture is in contact with the disinfectant (20 µl dried culture, 10 µl 3% H_2O_2).

To quantify disinfection, bacteria (*E. coli* 10-beta, Standard *E. coli* AMS 198 or OP50-GFP) were inoculated on glass coverslips (25 mm diameter). Four droplets of 5 µl each (20 µl) of the bacterial culture (starting concentration 108 CFU/ml) were placed onto each coverslip and allowed to dry for approximately 40 min. The slides with dry bacterial culture were then placed onto the flex-DBD with the inoculated side directly in contact with the discharge (Figure B.2B). The coverslips were treated for 10, 30, 90, and 270 s. At the end of the treatment time, the treated coverslip was placed in a centrifuge tube with 7.5 ml LB, enough to cover the coverslip. The tubes were vortexed on a medium setting for 20 s to recover the bacteria from the treated surface but not damage the cell membrane. The resulting bacterial suspension was spread on LB-agar plates and incubated for 24 h. Cultures were then counted and the number used to calculate the logarithmic reductions of bacterial concentration. All disinfection experiments were conducted with the flex-DBD operating at 3 kV, 20% duty cycle, and 40–50 °C.

We tested the efficiency of the flex-DBD disinfection in conjunction with a commonly available 3% solution of H_2O_2. The discharge in the flex-DBD is suppressed by water so we used a semipermeable polyethylene material (Tyvek, DuPont) to keep the H_2O_2 solution from the surface of the flex-DBD (Figure B.2C). Pieces of material were disinfected by soaking for 5 min in a 70% solution of isopropyl alcohol then dried thoroughly for at least 30 min. For each trial, we placed a piece of the sterile material on top of the operating flex-DBD and five 2 μl droplets of 3% H_2O_2 solution on top of the polyethylene material. We then placed an inoculated glass coverslip on top of the solution with the bacteria in contact with the solution (Figure B.2C). At the end of each treatment, we dropped both the coverslip and the cloth into a centrifuge tube with 7.5 ml of LB solution. The same recovery and plating procedure was used in all experiments. The controls for this experiment were inoculated but untreated coverslips, as well as the same procedure with H_2O_2 but with the flex-DBD remaining turned off. We also compared the disinfection efficiency of H_2O_2 aided only by the UV light produced by the flex-DBD. To block all the output from the plasma except light, we placed a thin film filter transparent down to 190 nm between the DBD and H_2O_2. Finally, to eliminate the operation temperature as a factor contributing to the disinfection process, we placed inoculated glass coverslips on a heating block at 47 °C and repeated the same disinfection procedures to determine the reduction in the bacterial load. We did not observe any reduction in the number of CFU/ml.

B.2.3 Disinfection data analysis

To quantify bacterial load reduction, we imaged the treated plates after 24 h of growth and counted the number of bacterial colonies, interpreted as colony forming units (CFUs) in the plate-seeding solution. When possible, we used ImageJ (1.53c) software (Schneider et al., 2012) to count CFUs, otherwise we counted visually. The bacterial load in CFU/ml was calculated by multiplying the CFU count by 9375 (follows from 40 µl spread on each plate from coverslips washing volume of 7.5 ml LB broth, and original inoculation volume of 20 µl), and multiplying to account for any serial dilutions. The logarithmic reduction in the bacterial load was calculated as $log10(NoN)$, where No is the bacterial load at CFU/ml without any treatment (0 s coverslip), and N is the bacterial load at CFU/ml at each treatment time. All the experiments were performed in triplicates of samples and plates. Statistical significance between pairs of treatments was evaluated using repeated measures ANOVA.

B.2.4 Chemical tests of the treated solutions

We determined the pH of the LB broth, Phosphate Buffer Saline solution (Sigma-Aldrich), and the 3% hydrogen peroxide solutions before and after the application of the flex-DBD, using a pH meter (Aspera Instruments, model SX823-B, ± 0.01 pH) and pH test strips (Esee, ± 0.5) for amounts too small for the pH sensor.

We used two indicator strip tests to check the H_2O_2 production by the plasma, 2–200 ppm range test strips (Industrial Test Systems) to test the production of H_2O_2 in ≈20 µl of Luria Broth and a 1 – 10% range to check the changes in the concentration of in the 3% H_2O_2 solution used for the disinfection that combined the flex-DBD and H_2O_2.

We used a scavenger method to assess qualitatively the production of the OH· in solutions during plasma treatment. We used coumarin (> 99%, Sigma-Aldrich) as a scavenger because it reacts with OH· in solution to produce 7-hydroxycoumarin that fluoresces at 460 nm when excited at 390 nm (Manevich et al., 1997). Coumarin itself does not fluoresce in this spectral range. We prepared a 5 mM solution of coumarin in a 20 mM PBS by dissolving crystalline coumarin in the PBS solution at a pH9 and readjusting the pH of the resulting solution back to 7.4 with HCl (Manevich et al., 1997). We used three reference solutions: the coumarin stock solution, a solution prepared by adding equal amounts of coumarin solution and PBS, and a solution prepared by adding equal amounts of the coumarin stock solution and 3% hydrogen peroxide. The fluorescence of each solution was recorded at room temperature using an Ocean Optics Fluorescence/Absorption spectrometer. Coumarin/PBS solution and coumarin/hydrogen peroxide solutions were treated with the DBD discharge for 5 min, and the fluorescence was recorded immediately following the treatment.

B.3 Results and Discussion

B.3.1 Surface dielectric barrier discharge in a flex-DBD device

A 40 kHz sinusoidal voltage, amplitude of 1.9–3 kV, was applied to the high voltage electrode for ~ 200 μs (20% duty cycle at 1 kHz repetition rate). A surface dielectric barrier discharge ignites inside the cavities and around the perimeter of the flex-DBD (Figure B.1D). The discharge propagates along the surface of the dielectric and eventually erodes the substrate of the ground electrode. The erosion pattern observed on post-run devices indicates that the discharge occurs in the center portion of each cavity leaving the angles intact. This is due to the electric field topology in the cavity with the maximum electric field $E = V/r \sim 80$ kV/cm, at the center of the circular cavity with a given radius (r). The erosion of the substrate of the patterned electrode happens over months of operation, possibly because only a few cells are lit at any time (apparent only at high temporal resolution imaging synchronized with the current spikes, Figure B.3B). During the discharge, the maximum current can be up to 100 mA for several tens of ns.

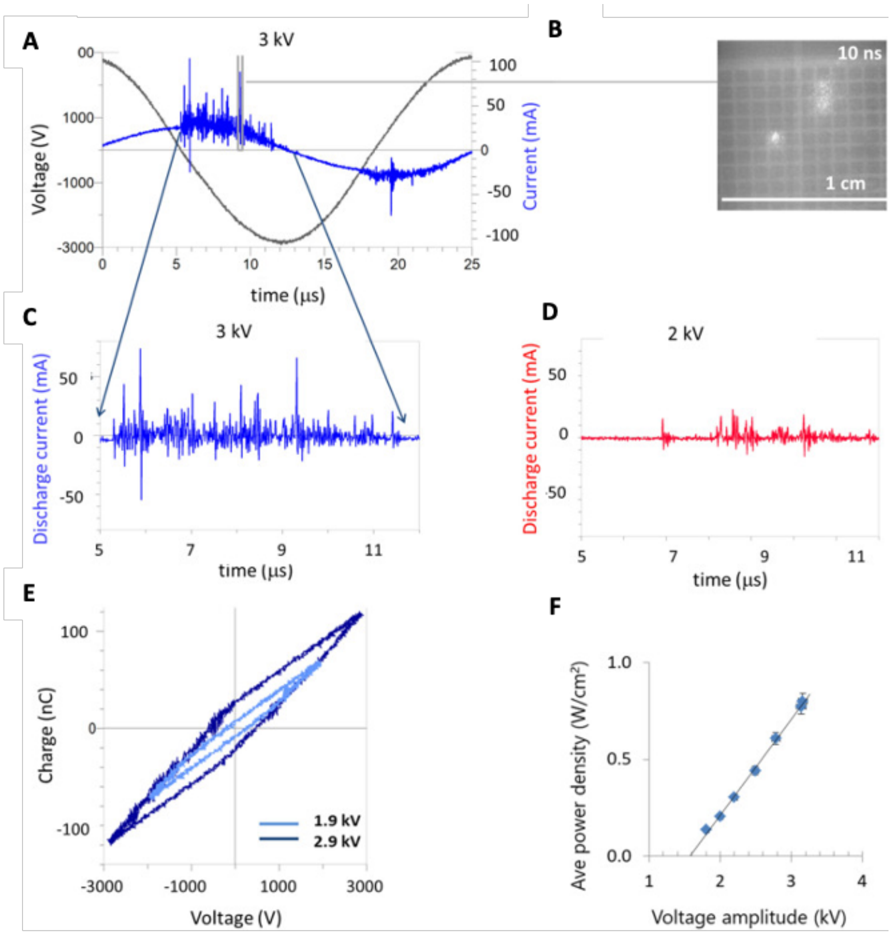

Figure B.3 Electrical characteristics of the flex-DBD. A) Current and voltage traces for one AC cycle. B) Only three of ninety cavities are lit during a 10 ns exposure synchronized with an individual current pulse (marked in a). C) The discharge current for one quarter of the cycle for applied voltage amplitudes of 3 kV and D) for 2 kV. E) From the Lissajous plots for one full cycle of the sinusoidal applied voltage we calculated that the 1.9 kV trial had 0.05 mJ/cycle and average discharge power of 0.3 W, while the 2.9 kV had 0.14 mJ/cycle and average discharge power of 0.75 W. F) The average power increases linearly as a function of the applied voltage amplitude when the duty cycle and the frequency were kept constant at 20% and 40 kHz, *respectively.*

Water can form a conductive film that prevents charge accumulation on the electrode, preventing breakdown conditions (Benard & Moreau, 2014; Biganzoli et al., 2013; Bruggeman et al., 2016; Wolfe et al., 1989). This effect depends on the voltage rise time and breakdown voltage may be reached at sub-nanosecond rise times. However, in the flex-DBD, the voltage rise time is ≈7 µs, too slow to prevent the charge leakage from the conductors. The parts of the device that become moist will not light until dry. If that occurs when the power is on, heating due to the resistive and dielectric losses will self-dry the device and it will restart once the moisture evaporates. We used a water-resistant material in the experiments with H_2O_2 solutions, to prevent the flex-DBD becoming wet while allowing active species from the plasma to reach the treated surface. This sensitivity to water is important for bio-related applications.

A typical current trace is comprised of a displacement current sinusoidal component of (42 ± 2) kHz and the superimposed sharp spikes 10 – 50 ns in duration corresponding to the discharges (Figure B.3A,C). The displacement current was subtracted from the total measured current to obtain the discharge current (Figure B.3C). The number of discharges, their overall duration, and their amplitude increase with increasing voltage (Figure B.3C). Although at 3 kV, the flex-DBD appeared completely lit, fast imaging triggered on a current spike demonstrates that during each current spike only a few bright regions are observed (Figure B.3B). Individual current spikes appear to correspond to isolated discharge events that appear randomly on the surface of the DBD. The number and the amplitude of the current spikes is not symmetrical in each half cycle of the AC current/voltage with a greater number of spikes occurring during the time when the mesh electrode acts as the anode, the voltage applied to the copper tape electrode is negative. In case of a positive mesh electrode, the electrons are able to flow into the anode and the current grows, but if the mesh electrode is negative, the electrons accumulate on the dielectric and the current stops resulting in lower current spikes. This asymmetry has been observed in plasma actuators that are a single edge surface DBD similar to the flex-DBD (Pons et al., 2005; Schneider et al., 2012). The number of individual discharges or current peaks varies depending on the maximum applied voltage (overvoltage). For example, the number of current peaks (over 10 mA) is 15 ± 8 at 2 kV and increases to 45 ± 8 for 3 kV (Figure B.3C). The greater number of current spikes results in a greater amount of charge transferred in the circuit as evident from the Lissajous plots (Figure B.3D).

The Lissajous plot has a two-slope shape with a slight asymmetry due to a greater number of more intense discharges for the negative voltage (positive patterned electrode). The energy dissipated in the circuit per one cycle can be calculated as the area of the Lissajous plot, and the power is then determined using the frequency, f, the duty cycle, ν,

$$P = f\nu \int QdV \qquad (C.1)$$

where Q is the charge measured by the capacitor probe and dV is the voltage obtained by the high voltage probe. For example, for the peak voltage of 1.9 kV the energy per cycle was 0.04 mJ/cycle. For the frequency of 41 kHz and a 20% duty cycle this gives the power of 0.3 W. For the max voltage of 2.9 kV the energy per cycle was 0.14 mJ/cycle, and the power, 1.1 W. The corresponding power density for the ~ 2 cm2 device is 0.15–0.5 W/cm2. The applied max AC voltage was varied from 1.6 kV to about 3 kV while keeping the frequency and the duty cycle constant. The resulting power varied linearly (Figure B.3E) with the applied voltage, which can be used as a calibration curve to set the desired power for a given device.

Increasing the operating voltage increases the discharge power and corresponds to an increase in the number of individual discharges and the production of plasma. Increasing the duty cycle increases the overall power consumption by the device but does not change the number of individual discharges per cycle.

B.3.2 Disinfection using the DBD

To evaluate the effectiveness of the flex-DBD device in decontamination of surfaces from biological contaminants, we conducted qualitative and quantitative experiments. The qualitative experiments included the treatment of *E. coli* in Petri dishes, the decontamination of inoculated aluminum and fabric surfaces (Figure B.4A, C); the quantitative bacterial load reduction was determined by treating bacterial culture dried onto glass coverslips (Figure B.4C).

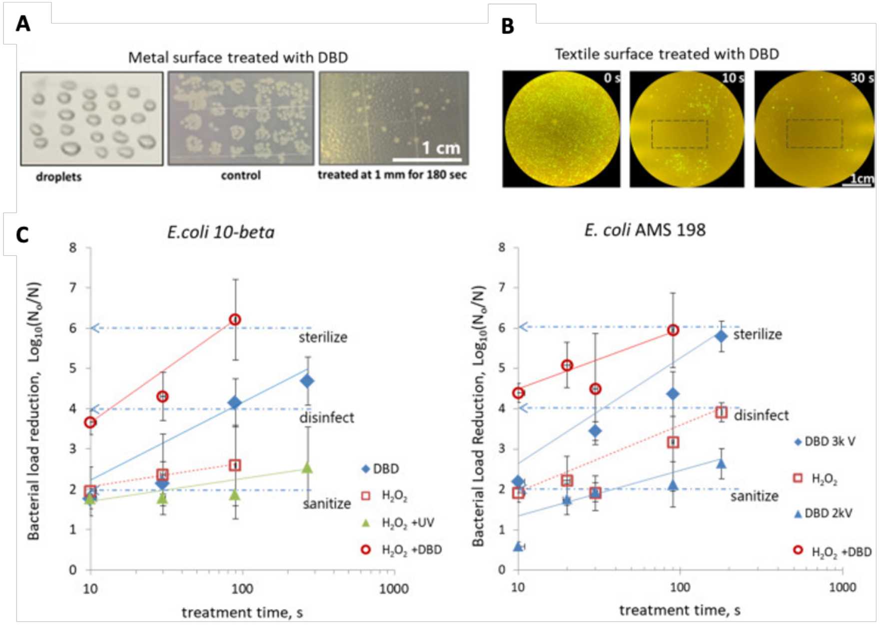

Figure B.4 Flex-DBD device effectively reduces bacterial load and its effect is synergistic with hydrogen peroxide. A) Aluminum surface inoculated with droplets of *E. coli* culture and stamped ("treated" photo). B) Textile surface inoculated with *E. coli* (OP50-GFP) and stamped. C) Reduction in the concentration of the *E. coli* colony forming units for two strains of *E. coli*. log10(No/N), where No is the number of CFU/ml surviving in the untreated samples, N is the number of surviving CFU/ml that remain after the treatment for 10, 30, 90, and 270 s. Common scale bars in a and b are 1 cm. The error bars are one standard deviation.

We placed droplets of the bacterial culture on an aluminum surface, treated by exposure to the flex-DBD, and then stamped with contact plates. The flex-DBD effectively reduced the bacterial load when the DBD was placed 1 mm from the surface and operated at 3 kV and 44 kHz, duty cycle of 20%. The flex-DBD device was also effective at disinfecting textile-type textile-like polyethylene material. To assess the spatial extent of disinfection we uniformly inoculated the fabric with a transgenic *E. coli* strain that expresses green fluorescent protein (OP-50-GFP) and treated a 10 × 20 mm area with the same operating parameters remained. Only viable bacteria contain GFP and fluoresce when excited with blue light. Indeed, there was a marked reduction in GFP positive colonies around the treated area (Figure B.4B). The distance of the DBD from the surface is also important because reducing the distance from 1 mm above the surface to a direct contact with the ground electrode, increased the rate of inactivation of bacteria. We obtained a similar spatial pattern by treating *E. coli* bacterial culture dried onto the surface of a glass coverslip, following 30 s treatment with the flex-DBD.

To quantify the bactericidal effect of the flex-DBD we inoculated and dried glass coverslips and measured the surviving bacterial load in colony forming units per milliliter (CFU/ml). Treatment with the flex-DBD device reduced viable bacteria $\log10(No/N) = 4.1$ after 90 s (Figure B.4C). The flex-DBD was operated at a voltage of 3 kV and discharge power of 0.5 W/cm2, and the temperature of the grounded surface was below 50 °C. We repeated the inactivation of *E. coli* using the Standard *E. coli* strain AMC 198 (ATCC 11,229) (Figure B.4C). Two experiments were conducted, one using a lower voltage, 2 kV peak voltage and the temperature of the grounded surface $T < 40$ °C, and 3 kV peak voltage and $T < 50$ °C. The higher applied voltage resulted in faster ($p = 0.003$, ANOVA) inactivation of *E. coli*; $\log10(No/N) = 5.8$ after 180 s treatment (Figure B.4C) as compared to $\log10(No/N) = 2.6$ after 180 s, demonstrating a dependence on the flex-DBD peak voltage.

We calculated the 1log10 reduction (D value) for *E. coli* AMS 198 because the data is less variable than that of 10-beta, probably due to a greater control of the strain characteristics. At the start of the plasma treatment, the plasma affects the most susceptible bacteria that is located the closest to the plasma and hence is subjected to shorter-lived reactive plasma species. Hence the inactivation rate is the highest for the short treatment times. A linear fit to the treatment times of 10 s to 270 s give the times for 1log10 reduction, D = 74 ± 2 s with the correlation coefficient, R = 0.996.

We tested whether it has been the device operating temperature (40 °C and 50 °C) that caused disinfection of *E. coli* 10 Beta and *E. coli* AMC 198 strains. Instead of treatment with flex-DBD we incubated contaminated coverslips at 50 °C. We found no reduction in the bacterial load even at the longest exposure times of 180 s and 270 s. Therefore, the improvement in the disinfection at higher voltage may be attributed to plasma related effects such as the increase in the concentration of reactive species.

Spectral analysis of the flex-DBD confirms the production of the OH· (Figure B.5A) and a wide range of ROS and RNS (Figure C.5B) by the discharge. Hydroxyl radical is the highest oxidizer and it reacts with lipids in the cell membrane and oxidizes proteins and nucleic acids inside the cells. Because of its reactivity, it is very short-lived and needs to be produced at the site of action. Since the inoculated coverslips were in contact with the patterned side of the flex-DBD during treatment, we can speculate that the reactions of OH· and other short-lived ROS are responsible for the fast-initial rate of bacterial inactivation. Ozone and nitrogen oxides evident in the IR absorption spectrum can diffuse into the substrate and continue the disinfection process at a slower rate limited by the rate of diffusion and cellular processes (Bauer & Graves, 2016; Girard et al., 2016; Lu et al., 2016).

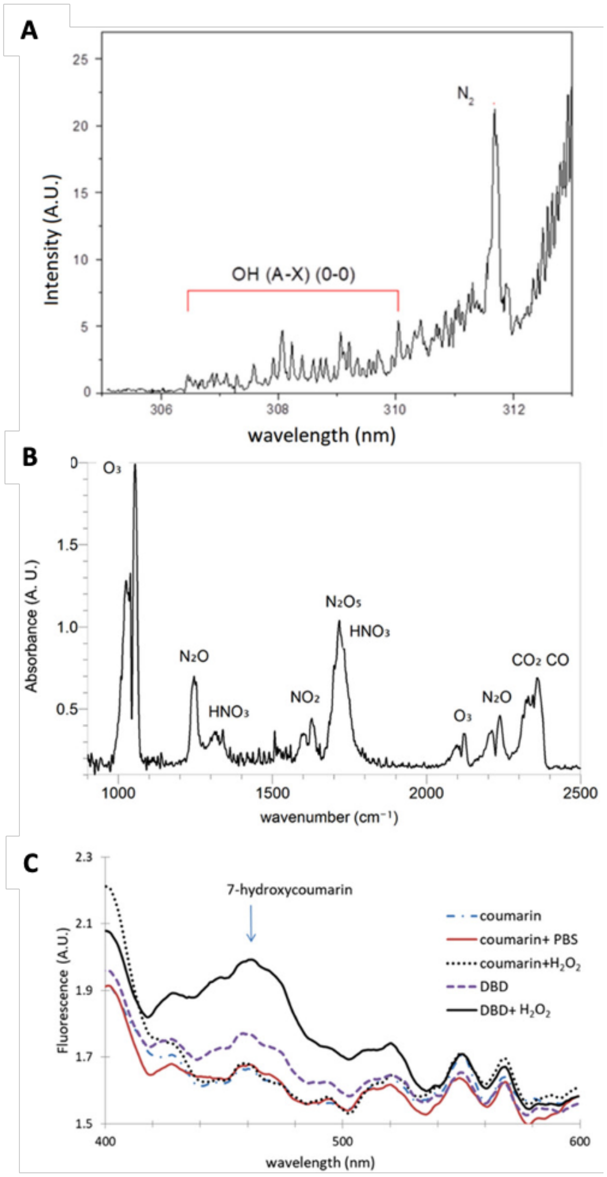

Figure B.5 Spectral analysis of the flex-DBD: A) Optical emission spectrum showing the OH· emission band. B) Infrared absorption spectrum showing the long-lived active species, O3, NO2, N2O, etc. produced in the discharge. Spectrum taken after 1 min of operation at the power and voltage used for treating bacteria. C) Fluorescence of the 7-hydroxycoumarin indicating the presence of OH· in solution. Solution of coumarin in PBS, and coumarin with H_2O_2 are not different from the coumarin in water that is used to produce the baseline spectra. Fluorescence intensity increased at 460 nm following plasma treatment (DBD) and further increased for plasma treated H_2O_2 solution (DBD + H_2O_2). Spectra were taken immediately after treating 1.5 ml liquid samples for 5 min at the same DBD setting. Each curve is an average of three trials.

B.3.3 Combined effect of plasma and hydrogen peroxide

To augment the disinfection, we applied the flex-DBD treatment in combination with 3% H_2O_2 solution commonly available and, widely used for oral, skin, and wound disinfection. Applying the DBD together with H_2O_2 results in a 3.5 log10 reduction in the bacterial population in just 10 s and in > 5log10 reduction in 90 s (Figure B.4C). The combined disinfection effect of hydrogen peroxide and plasma is faster than either DBD alone ($p = 0.04$, repeated measures ANOVA test) or H_2O_2 alone ($p = 0.03$).

The antibacterial mechanism of H_2O_2 solutions alone is based on the production of the highly reactive hydroxyl radicals, but there is no appreciable equilibrium concentration of OH. in the solution itself. We used a chemical scavenger method to detect the presence of the OH. radical in 3% H_2O_2 solution and found that the concentration is of the same order as coumarin/PBS solutions that contain no hydrogen peroxide (Figure B.5.C). The hydroxyl radical can be produced inside a cell by the Fenton reaction:

$$Fe^{2+} + H_2O_2 \rightarrow Fe^{3+} + OH^{-} + OH^{\cdot} \qquad \text{(C.2)}$$

The production of OH. leads to oxidation and eventually to cell death. This disinfection by H_2O_2 alone depends on the concentration of the solution and can be concentration limited, slowing down as the hydrogen peroxide is used up (Gibalov & Pietsch, 2000). Our results show that a bacterial load reduction due to the H_2O_2 alone (Figure B.4C) slows down faster than the corresponding DBD treatment (the times for 1log10 reduction, $D = 139 \pm 5$ s, $R = 0.97$ for *E. coli 10-beta*; and $D = 135 \pm 5$ s, $R = 0.947$ for *E. coli* AMC 198).

The sustained rate of reduction increases to $D = 40$ s ($R = 0.86$) when the treatment is carried out by both the DBD and the H_2O_2 solution (Figure B.4C) and reaches a > 6log10 reduction in just 90 s. In humid environments, air plasma produces hydroxyl radicals generally through the interactions of electrons and excited nitrogen with water vapor. But the hydroxyl radical reacts, oxidizes or recombines to form hydrogen peroxide on a microsecond scale (Bruggeman et al., 2016; Bruggeman & Leys, 2009; R. Zhou et al., 2015), which then diffuses into the solution, thus resulting in the production of H_2O_2 in the solution. The results of the indicator experiments support the increase of H_2O_2 concentration in both the Luria broth used for the *E. coli* suspensions and in the H_2O_2 solution used in the experiments with flex-DBD and H_2O_2. The application of flex-DBD to Luria broth for 90 s increases the concentration of H_2O_2 (and other oxidizing agents) to at least 100 ppm. Applying the flex-DBD directly to the H_2O_2 solution for 90 s treatment time, the concentration of increases the concentration of H_2O_2 from 3% before treatment to 5–10% after treatment.

Plasma can generate H_2O_2 in water solutions but the UV radiation from the plasma can also decompose the existing H_2O_2. To test whether the UV radiation from the flex-DBD was sufficient to explain the improved *E. coli* inactivation with H_2O_2 we blocked all plasma products except for the UV radiation with a UV filter. UV radiation improved the inactivation of bacteria in the first 30 s compared with H_2O_2 alone, but it did not achieve any additional reduction with increasing treatment time. After the first 30 s, the survival curve flattens ($D > 250$ s). This effect of UV radiation is insufficient to explain the improvement in the inactivation with H_2O_2 achieved by the addition of the DBD plasma. Hence the plasma, not UV radiation alone, improves the action of H_2O_2.

The remarkable synergy between plasma and H_2O_2 can be explained by the combination of the peroxone process with the RNS produced by the flex-DBD. The IR absorption spectrum is dominated by ozone and RNS. Peroxone is an advanced oxidation process that has been known for over 100 years. It involves the reactions of ozone and hydrogen peroxide that promote the production of OH·, which is a much more effective oxidizer than ozone alone (Wolfe et al., 1989). Plasma-generated superoxide can also aid in the process of generating OH· in solution. The scavenger method shows that plasma generates not only a stable hydrogen peroxide in a liquid solution but a measurable OH· concentration (Figure B.5C). Plasma treatment of a H_2O_2 solution results in a significant increase in the concentration of OH· in solution, well above plasma treatment alone. OH· oxidation can lead to an easier penetration of the membrane by RNS that damage the proteins inside the cell and improve the overall disinfection process (Bauer & Graves, 2016; Girard et al., 2016; Kovačević et al., 2017; Lu et al., 2016; Lukes et al., 2014). Hence the combination of plasma treatment with hydrogen peroxide is a powerful tool for disinfection of bacterial contaminants.

Although many years of investigation continue to demonstrate the potential of plasma in disinfection of biological and non-biological surfaces, the devices that have been accepted alongside the steam sterilization in medical and pharmaceutical industries are low pressure plasma- H_2O_2 vapor chambers (Cummings A.I & Childers R.W, 1990; Golkowski et al., 2012; Kahnert et al., 2005). Our results demonstrate that plasma disinfection could fill a technological gap not as a replacement for the standard bulk sterilization methods but in special niche applications and in personal consumer use (Bekeschus et al., 2019).

B.4 Conclusion

Here we demonstrate the effectiveness of the first hand-held flex-DBD device that is suitable for personal use by untrained personnel. This flex-DBD device achieves fast disinfection, 4log10 reduction, in under 90 s and reaches > 5log10 in 270 s. Augmented with H_2O_2-flex-DBD it achieves high bacterial load reduction two times faster than alone: > 6log10 in 90 s with D = 2.5 s for the first 10 s and D = 30 s for 10 s – 180 s treatment times. These results are faster than UV and chemicals alone and faster than atmospheric pressure glow discharge, mesh DBD, and plasma activated water.

The synergy of plasma and hydrogen peroxide is due to plasma activation of H_2O_2. Our experimental results indicate that the mechanism of this activation is due to two factors. A peroxone process produces $OH\cdot$ in H_2O_2 solution and the combined action of $OH\cdot$ and RNS leads to enhanced disinfection. Novel in-situ FTIR AS measurements of the flex-DBD show the presence of ozone and RNS in the plasma effluent. The scavenger method demonstrates a significant increase in the $OH\cdot$ concentration in the H_2O_2 solution. These measurements support the proposed mechanism.

The flex-DBD device can make effective disinfection accessible to the untrained public. It is safe in operation since the user facing components are grounded. The electrical measurements described above show that the flex-DBD operates consistently over prolonged periods, at least 15 min at a time for a total of more than 100 h of operation. The synergistic action with H_2O_2 reaches high levels of disinfection and opens exciting new possibilities for decontamination and treatment. This device can be used to disinfect personal protection equipment, hands, and frequently touched surfaces, as well as for wound treatment and other medical applications.

B.5 Acknowledgements

This material is based upon work supported by the U.S. Department of Energy, Office of Science, Office of Fusion Energy Sciences under contract number DE-AC02-09CH11466. This research used resources of the Princeton Collaborative Low Temperature Plasma Research Facility (PCRF http://pcrf.pppl.gov), which is a collaborative research facility supported by the U.S. Department of Energy, Office of Science, Office of Fusion Energy Sciences.

B.6 Author Contributions

S.G. collaborated on all experiments, data acquisition, analysis, writing the manuscript, and preparing the Figure s. M.B.H. collaborated on all biological experiments, conducted data acquisition for the biological experiments, and collaborated on writing the manuscript. S.Y. contributed the device design and main ideas for the experiments, manufactured the first prototypes of the device, collaborated on spectroscopic experiments. Y.R. contributed the main scientific direction and guidance of this work and collaborated on writing the manuscript. PE contributed scientific ideas for the experiments in the area of using the semipermeable material for the delivery of H2O2, collaborated on developing the scientific direction for this work. G.H. contributed the biological expertise and guidance for the project, collaborated on writing the manuscript. G.H. is the P.I. under the PCRF collaboration with PPPL.

B.7 Data Availability

The datasets generated during and/or analyzed during the current study are available from the corresponding author on reasonable request.

APPENDIX C

INFORMATION PERTAINING TO AUTHORSHIP, ACKNOWLEDGEMENTS, AND FUNDING OF DISSERTATION CHAPTERS

C.1 Information pertaining to authorship, acknowledgments, and funding for Chapter 2

C.1.1 Co-authors

Maria B Harreguy, Vanessa Marfil, Noah W.F. Grooms, Christopher V. Gabel, Samuel H. Chung, Gal Haspel

C.1.2 Author contributions

Approach conception: G.H.; ink layer experiment: M.B.H., N.W.F.G., V.M., and S.H.C.; amphid bundle ablation: M.B.H. and S.H.C.; axon regeneration experiments: M.B.H., N.W.F.G. and V.M.; laser maintenance: C.V.G.; supervision: C.V.G., S.H.C. and G.H. G.H. wrote the first manuscript draft; all authors subsequently took part in the revision process and approve the final manuscript.

C.1.3 Acknowledgements

We thank Chris McRaven, and Adam Perry, of Menlo Systems for support in setting up and integrating the BlueCut system. The system was purchased with funds from GH start-up resources provided by the New Jersey Institute of Technology. We also thank Michael Bastiani for advice on nanosecond pulse laser integration. We find WormBase invaluable; it is supported by grant U41 HG002223 from the NIH National Human Genome Research Institute, and from the MRC and BBSRC. Some strains were provided by the CGC, which is funded by NIH Office of Research Infrastructure Programs (P40 OD010440). This study was partially funded by grant CSCR14ERG002 from the State of New Jersey Commission on Spinal Cord Research.

C.1.4 Data accessibility statement

The datasets generated during or analysed during the current study are available from the corresponding author on reasonable request.

C.1.5 Funding

This study was partially funded by grant CSCR14ERG002 from the State of New Jersey Commission on Spinal Cord Research.

C.2 Information pertaining to authorship, acknowledgments, and funding for Chapter 3

C.2.1 Co-authors

Harreguy, M. B., Tanvir, Z., Shah, E., Simprevil, B., Tran, T. S., & Haspel, G.

C.2.2 Author contributions

MBH, TST, and GH contributed to the conception and design of the study. MBH, ES, and BS maintained and generated strains and collected behavior data. MBH and ZT collected and analyzed imaging data. MBH performed the statistical analysis. MBH wrote the first draft of the manuscript. GH, ZT, and TST wrote sections of the manuscript. All authors contributed to manuscript revision, read, and approved the submitted version.

C.2.3 Acknowledgements

We thank Joseph Culotti (University of Toronto, Mt Sinai Hospital) and Richard Ikegami (UC Berkeley) for sharing the *plx-2* and *plx-1* reporter strains. We also thank Kang Shen (Stanford University) and Kota Mizumoto (University of British Columbia) for the *plx-1* reporter constructs. We thank Monica Driscoll (Rutgers University) for her help in generating transgenic lines and the Hobert Lab (Columbia University) for the NeuroPal strains. We thank Joseph Soubany for help with locomotion analysis. Research reported in this publication was supported by NINDS of the National Institutes of Health (1R15NS125565-01; MBH, SE, SB, TST, and GH), by the State of New Jersey Commission on Spinal Cord Research (CSCR14ERG002; GH; and CSCR16IRG013; TST), by IOS of the National Science Foundation (2034864; TST), and by the NJIT Undergraduate Research Initiative (URI; ES). Some strains were provided by the CGC, which is funded by NIH Office of Research Infrastructure Programs (P40 OD010440).

C.2.4 Data availability statement

The datasets presented in this study can be found in online Open Science Framework repository: https://osf.io/6a49y/?view_only=75ca9fcc21594c9d9c85152e259d0230.

C.2.5 Funding

Research reported in this publication was supported by NINDS of the National Institutes of Health (1R15NS125565-01; MBH, SE, SB, TST, and GH), by the State of New Jersey Commission on Spinal Cord Research (CSCR14ERG002; GH; and CSCR16IRG013; TST), by IOS of the National Science Foundation (2034864; TST), and by the NJIT Undergraduate Research Initiative (URI; ES).

REFERENCES

Aboubakr, H. A., Mor, S. K., Higgins, L. A., Armien, A., Youssef, M. M., Bruggeman, P. J., & Goyal, S. M. (2018). Cold argon-oxygen plasma species oxidize and disintegrate capsid protein of feline calicivirus. *PLoS ONE*, *13*(3). https://doi.org/10.1371/journal.pone.0194618

Alto, L. T., & Terman, J. R. (2017). Semaphorins and their signaling mechanisms. *Methods in Molecular Biology*, *1493*, 1–25. https://doi.org/10.1007/978-1-4939-6448-2_1

Altun, Z. F., & Hall, D. H. (2005a). WormAtlas Hermaphrodite Handbook - Muscle System - Introduction. *WormAtlas*. https://doi.org/10.3908/WORMATLAS.1.6

Altun, Z. F., & Hall, D. H. (2005b). WormAtlas Hermaphrodite Handbook - Nervous System - General Description. *WormAtlas*. https://doi.org/10.3908/wormatlas.1.18

Assous, M., Martinez, E., Eisenberg, C., Shah, F., Kosc, A., Varghese, K., Espinoza, D., Bhimani, S., Tepper, J. M., Shiflett, M. W., & Tran, T. S. (2019). Neuropilin 2 Signaling Mediates Corticostriatal Transmission, Spine Maintenance, and Goal-Directed Learning in Mice. *Journal of Neuroscience*, *39*(45), 8845–8859. https://doi.org/10.1523/JNEUROSCI.1006-19.2019

Au, V., Li-Leger, E., Raymant, G., Flibotte, S., Chen, G., Martin, K., Fernando, L., Doell, C., Rosell, F. I., Wang, S., Edgley, M. L., Rougvie, A. E., Hutter, H., & Moerman, D. G. (2019). CRISPR/Cas9 methodology for the generation of knockout deletions in *Caenorhabditis elegans*. *G3: Genes, Genomes, Genetics*, *9*(1). https://doi.org/10.1534/g3.118.200778

Avery, L., & Horvitzt, H. R. (1989). Pharyngeal pumping continues after laser killing of the pharyngeal nervous system of C. elegans. *Neuron*, *3*(4), 473–485. https://doi.org/10.1016/0896-6273(89)90206-7

Bagri, A., Cheng, H.-J., Yaron, A., Pleasure, S. J., & Tessier-Lavigne, M. (2003). Stereotyped Pruning of Long Hippocampal Axon Branches Triggered by Retraction Inducers of the Semaphorin Family. *Cell*, *113*(3), 285–299. https://doi.org/10.1016/S0092-8674(03)00267-8

Bargmann, C. I., Hartwieg, E., & Horvitz, H. R. (1993). Odorant-selective genes and neurons mediate olfaction in C. elegans. *Cell*, *74*(3), 515–527. https://doi.org/10.1016/0092-8674(93)80053-H

Bargmann, C. I., & Horvitz, H. R. (1991). Chemosensory neurons with overlapping functions direct chemotaxis to multiple chemicals in C. elegans. *Neuron*, *7*(5), 729–742. https://doi.org/10.1016/0896-6273(91)90276-6

Battistini, C., & Tamagnone, L. (2016). Transmembrane semaphorins, forward and reverse signaling: have a look both ways. *Cellular and Molecular Life Sciences : CMLS*, *73*(8), 1609–1622. https://doi.org/10.1007/S00018-016-2137-X

Bauer, G., & Graves, D. B. (2016). Mechanisms of Selective Antitumor Action of Cold Atmospheric Plasma-Derived Reactive Oxygen and Nitrogen Species. *Plasma Processes and Polymers*, *13*(12). https://doi.org/10.1002/ppap.201600089

Bejjani, R. El, & Hammarlund, M. (2012). Neural regeneration in *Caenorhabditis elegans*. *Annual Review of Genetics*, *46*, 499–513. https://doi.org/10.1146/ANNUREV-GENET-110711-155550

Bekeschus, S., Favia, P., Robert, E., & von Woedtke, T. (2019). White paper on plasma for medicine and hygiene: Future in plasma health sciences. *Plasma Processes and Polymers*, *16*(1). https://doi.org/10.1002/ppap.201800033

Bekeschus, S., Kramer, A., Suffredini, E., Von Woedtke, T., & Colombo, V. (2020). Gas Plasma Technology-An Asset to Healthcare during Viral Pandemics Such as the COVID-19 Crisis? *IEEE Transactions on Radiation and Plasma Medical Sciences*, *4*(4). https://doi.org/10.1109/TRPMS.2020.3002658

Benard, N., & Moreau, E. (2014). Electrical and mechanical characteristics of surface AC dielectric barrier discharge plasma actuators applied to airflow control. *Experiments in Fluids*, *55*(11). https://doi.org/10.1007/s00348-014-1846-x

Biganzoli, I., Barni, R., & Riccardi, C. (2013). Temporal evolution of a surface dielectric barrier discharge for different groups of plasma microdischarges. *Journal of Physics D: Applied Physics*, *46*(2). https://doi.org/10.1088/0022-3727/46/2/025201

Boekema, B. K. H. L., Vlig, M., Guijt, D., Hijnen, K., Hofmann, S., Smits, P., Sobota, A., Van Veldhuizen, E. M., Bruggeman, P., & Middelkoop, E. (2015). A new flexible DBD device for treating infected wounds: In vitro and ex vivo evaluation and comparison with a RF argon plasma jet. *Journal of Physics D: Applied Physics*, *49*(4). https://doi.org/10.1088/0022-3727/49/4/044001

Bourgeois, F., & Ben-Yakar, A. (2007). Femtosecond laser nanoaxotomy properties and their effect on axonal recovery in C. elegans. *Optics Express*, *16*(8), 5963. https://doi.org/10.1364/OE.15.008521

Brandenburg, R. (2017). Dielectric barrier discharges: Progress on plasma sources and on the understanding of regimes and single filaments. In *Plasma Sources Science and Technology* (Vol. 26, Issue 5). https://doi.org/10.1088/1361-6595/aa6426

Brenner, S. (1974). The Genetics of *Caenorhabditis elegans*. *Genetics*, *77*(1), 71–94. https://doi.org/10.1093/genetics/77.1.71

Brenner, S. (2009). In the beginning was the worm.. In *Genetics* (Vol. 182, Issue 2). https://doi.org/10.1534/genetics.109.104976

Brittin, C. A., Cook, S. J., Hall, D. H., Emmons, S. W., & Cohen, N. (2021). A multi-scale brain map derived from whole-brain volumetric reconstructions. *Nature*, *591*(7848). https://doi.org/10.1038/s41586-021-03284-x

Bruggeman, P. J., Kushner, M. J., Locke, B. R., Gardeniers, J. G. E., Graham, W. G., Graves, D. B., Hofman-Caris, R. C. H. M., Maric, D., Reid, J. P., Ceriani, E., Fernandez Rivas, D., Foster, J. E., Garrick, S. C., Gorbanev, Y., Hamaguchi, S., Iza, F., Jablonowski, H., Klimova, E., Kolb, J., … Zvereva, G. (2016). Plasma-liquid interactions: A review and roadmap. In *Plasma Sources Science and Technology* (Vol. 25, Issue 5). https://doi.org/10.1088/0963-0252/25/5/053002

Bruggeman, P., & Leys, C. (2009). Non-thermal plasmas in and in contact with liquids. *Journal of Physics D: Applied Physics*, *42*(5). https://doi.org/10.1088/0022-3727/42/5/053001

Byrne, A. B., & Hammarlund, M. (2017). Axon Regeneration in C. elegans: worming our way to mechanisms of axon regeneration. *Experimental Neurology*, *287*(Pt 3), 300. https://doi.org/10.1016/J.EXPNEUROL.2016.08.015

C. elegans Sequencing Consortium. (1998). *Genome Sequence of the Nematode C. elegans: A Platform for Investigating Biology*. https://doi.org/10.1126/science.282.5396.2012

Chalfie, M., Sulston, J. E., White, J. G., Southgate, E., Thomson, J. N., & Brenner, S. (1985). The neural circuit for touch sensitivity in *Caenorhabditis elegans*. *The Journal of Neuroscience*, *5*(4), 956 LP – 964. https://doi.org/10.1523/JNEUROSCI.05-04-00956.1985

Chen, G., Sima, J., Jin, M., Wang, K., Xue, X., Zheng, W., Ding, Y., & Yuan, X. (2007). Semaphorin-3A guides radial migration of cortical neurons during development. *Nature Neuroscience 2008 11:1*, *11*(1), 36–44. https://doi.org/10.1038/nn2018

Chen, H., Chédotal, A., He, Z., Goodman, C. S., & Tessier-Lavigne, M. (1997). Neuropilin-2, a Novel Member of the Neuropilin Family, Is a High Affinity Receptor for the Semaphorins Sema E and Sema IV but Not Sema III. *Neuron*, *19*(3), 547–559. https://doi.org/10.1016/S0896-6273(00)80371-2

Chen, H., He, Z., Bagri, A., & Tessier-Lavigne, M. (1998). Semaphorin–Neuropilin Interactions Underlying Sympathetic Axon Responses to Class III Semaphorins. *Neuron*, *21*(6), 1283–1290. https://doi.org/10.1016/S0896-6273(00)80648-0

Chen, L., & Chisholm, A. D. (2011). Axon regeneration mechanisms: insights from C. elegans. *Trends in Cell Biology*, *21*(10), 577. https://doi.org/10.1016/J.TCB.2011.08.003

Chen, L., Wang, Z., Ghosh-Roy, A., Hubert, T., Yan, D., O'Rourke, S., Bowerman, B., Wu, Z., Jin, Y., & Chisholm, A. D. (2011). Axon regeneration pathways identified by systematic genetic screening in C. elegans. *Neuron*, *71*(6), 1043–1057. https://doi.org/10.1016/j.neuron.2011.07.009

Chin-Sang, I. D., George, S. E., Ding, M., Moseley, S. L., Lynch, A. S., & Chisholm, A. D. (1999). The Ephrin VAB-2/EFN-1 Functions in Neuronal Signaling to Regulate Epidermal Morphogenesis in C. elegans. *Cell*, *99*(7), 781–790. https://doi.org/10.1016/S0092-8674(00)81675-X

Chisholm, A. D., Hutter, H., Jin, Y., & Wadsworth, W. G. (2016). The Genetics of Axon Guidance and Axon Regeneration in *Caenorhabditis elegans*. *Genetics*, *204*(3), 849 LP – 882. https://doi.org/10.1534/genetics.115.186262

Chung, S. H., Clark, D. A., Gabel, C. V., Mazur, E., & Samuel, A. D. T. (2006a). The role of the AFD neuron in *C. elegans* thermotaxis analyzed using femtosecond laser ablation. *BMC Neuroscience*, *7*(1), 1–11. https://doi.org/10.1186/1471-2202-7-30/FIGURE S/4

Chung, S. H., Clark, D. A., Gabel, C. V, Mazur, E., & Samuel, A. D. T. (2006b). The role of the AFD neuron in *C. elegans* thermotaxis analyzed using femtosecond laser ablation. *BMC Neuroscience*, *7*(1), 30. https://doi.org/10.1186/1471-2202-7-30

Chung, S. H., & Mazur, E. (2009). Femtosecond laser ablation of neurons in *C. elegans* for behavioral studies. *Applied Physics A*, *96*(2), 335–341. https://doi.org/10.1007/s00339-009-5201-7

Chung, S. H., Schmalz, A., Ruiz, R. C. H., Gabel, C. V, & Mazur, E. (2013). Femtosecond laser ablation reveals antagonistic sensory and neuroendocrine signaling that underlie *C. elegans* behavior and development. *Cell Reports*, *4*(2), 316–326. https://doi.org/10.1016/j.celrep.2013.06.027

Cook, S. J., Jarrell, T. A., Brittin, C. A., Wang, Y., Bloniarz, A. E., Yakovlev, M. A., Nguyen, K. C. Q., Tang, L. T.-H., Bayer, E. A., Duerr, J. S., Bülow, H. E., Hobert, O., Hall, D. H., & Emmons, S. W. (2019). Whole-animal connectomes of both *Caenorhabditis elegans* sexes. *Nature*, *571*(7763), 63–71. https://doi.org/10.1038/s41586-019-1352-7

Cooke, P., Janowitz, H., & Dougherty, S. E. (2022). Neuronal Redevelopment and the Regeneration of Neuromodulatory Axons in the Adult Mammalian Central Nervous System. *Frontiers in Cellular Neuroscience*, *16*. https://doi.org/10.3389/fncel.2022.872501

Corsi, A. K., Wightman, B., & Chalfie, M. (2015). A transparent window into biology: A primer on *Caenorhabditis elegans*. *Genetics*, *200*(2). https://doi.org/10.1534/genetics.115.176099

Cox, G. N., Laufer, J. S., Kusch, M., & Edgar, R. S. (1980). Genetic and phenotypic characterization of roller mutants of *Caenorhabditis elegans*. *Genetics*, *95*(2). https://doi.org/10.1093/genetics/95.2.317

Crow, S., & Smith, J. H. (1995). Gas Plasma Sterilization: Application of Space-Age Technology. *Infection Control and Hospital Epidemiology*, *16*(8). https://doi.org/10.2307/30141085

Cummings A.I, & Childers R.W. (1990). *Hydrogen peroxide sterilization method.*

Curley, P. F., Ferguson, A. I., White, J. G., & Amos, W. B. (1992). Application of a femtosecond self-sustaining mode-locked Ti:sapphire laser to the field of laser scanning confocal microscopy. *Optical and Quantum Electronics*, *24*(8), 851–859. https://doi.org/10.1007/BF00620198

Dalpé, G., Brown, L., & Culotti, J. G. (2005). Vulva morphogenesis involves attraction of plexin 1-expressing primordial vulva cells to semaphorin 1a sequentially expressed at the vulva midline. *Development*, *132*(6), 1387–1400. https://doi.org/10.1242/DEV.01694

Dalpé, G., Zhang, L., Zheng, H., & Culotti, J. (2004). Conversion of cell movement responses to Semaphorin-1 and Plexin-1 from attraction to repulsion by lowered levels of specific RAC GTPases in C. elegans. *Development (Cambridge, England)*, *131*(9), 2073–2088. https://doi.org/10.1242/DEV.01063

Dalpe, G., Zheng, H., Brown, L., & Culotti, J. (2012). Semaphorin-1 and netrin signal in parallel and permissively to position the male ray 1 sensillum in *Caenorhabditis elegans*. *Genetics*, *192*(3), 959–971. https://doi.org/10.1534/genetics.112.144253

Danelon, V., Goldner, R., Martinez, E., Gokhman, I., Wang, K., Yaron, A., & Tran, T. S. (2020). Modular and Distinct Plexin-A4/FARP2/Rac1 Signaling Controls Dendrite Morphogenesis. *Journal of Neuroscience*, *40*(28), 5413–5430. https://doi.org/10.1523/JNEUROSCI.2730-19.2020

De Winter, F., Oudega, M., Lankhorst, A. J., Hamers, F. P., Blits, B., Ruitenberg, M. J., Pasterkamp, R. J., Gispen, W. H., & Verhaagen, J. (2002). Injury-induced class 3 semaphorin expression in the rat spinal cord. *Experimental Neurology*, *175*(1), 61–75. https://doi.org/10.1006/exnr.2002.7884

DiLoreto, E. M., Chute, C. D., Bryce, S., & Srinivasan, J. (2019). Novel Technological Advances in Functional Connectomics in C. elegans. *Journal of Developmental Biology*, *7*(2). https://doi.org/10.3390/jdb7020008

Dixon, S. J., & Roy, P. J. (2005). Muscle arm development in *Caenorhabditis elegans*. *Development*, *132*(13). https://doi.org/10.1242/dev.01883

Edelstein, A. D., Tsuchida, M. A., Amodaj, N., Pinkard, H., Vale, R. D., & Stuurman, N. (2014). Advanced methods of microscope control using μManager software. *Journal of Biological Methods*, *1*(2), e10. https://doi.org/10.14440/jbm.2014.36

Eisenberg, C., Subramanian, D., Afrasiabi, M., Ziobro, P., Delucia, J., Hirschberg, P. R., Shiflett, M. W., Santhakumar, V., & Tran, T. S. (2021). *Reduced hippocampal inhibition and enhanced autism-epilepsy comorbidity in mice lacking neuropilin 2*. https://doi.org/10.1038/s41398-021-01655-6

Eto, H., Ono, Y., Ogino, A., & Nagatsu, M. (2008). Low-temperature sterilization of wrapped materials using flexible sheet-type dielectric barrier discharge. *Applied Physics Letters*, *93*(22). https://doi.org/10.1063/1.3039808

Fan, J., Mansfield, S. G., Redmond, T., Gordon-Weeks, P. R., & Raper, J. A. (1993). The organization of F-actin and microtubules in growth cones exposed to a brain-derived collapsing factor. *The Journal of Cell Biology*, *121*(4), 867–878. https://doi.org/10.1083/jcb.121.4.867

Fang-Yen, C., Gabel, C. V, Samuel, A. D. T., Bargmann, C. I., & Avery, L. (2012). Chapter 6 - Laser Microsurgery in *Caenorhabditis elegans*. *Methods in Cell Biology*, *Volume 107*, 177–206. https://doi.org/10.1016/B978-0-12-394620-1.00006-0

Fard, D., & Tamagnone, L. (2021). Semaphorins in health and disease. *Cytokine & Growth Factor Reviews*, *57*, 55–63. https://doi.org/10.1016/J.CYTOGFR.2020.05.006

Faumont, S., Lindsay, T. H., & Lockery, S. R. (2012). Neuronal microcircuits for decision making in C. elegans. In *Current Opinion in Neurobiology* (Vol. 22, Issue 4). https://doi.org/10.1016/j.conb.2012.05.005

Félix, M.-A., & Duveau, F. (2012). Population dynamics and habitat sharing of natural populations of *Caenorhabditis elegans* and C. briggsae. *BMC Biology*, *10*(1), 59. https://doi.org/10.1186/1741-7007-10-59

Fies, J., Gemmell, B. J., Fogerson, S. M., Morgan, J. R., Tytell, E. D., & Colin, S. P. (2021). Swimming kinematics and performance of spinal transected lampreys with different levels of axon regeneration. *Journal of Experimental Biology*, *224*(21). https://doi.org/10.1242/jeb.242639

Fire, A., Xu, S., Montgomery, M. K., Kostas, S. A., Driver, S. E., & Mello, C. C. (1998). Potent and specific genetic interference by double-stranded RNA in *Caenorhabditis elegans*. *Nature*, *391*(6669). https://doi.org/10.1038/35888

Fridman, G., Peddinghaus, M., Ayan, H., Fridman, A., Balasubramanian, M., Gutsol, A., Brooks, A., & Friedman, G. (2006). Blood coagulation and living tissue sterilization by floating-electrode dielectric barrier discharge in air. *Plasma Chemistry and Plasma Processing*, *26*(4). https://doi.org/10.1007/s11090-006-9024-4

Fujii, T., Nakao, F., Shibata, Y., Shioi, G., Kodama, E., Fujisawa, H., & Takagi, S. (2002). *Caenorhabditis elegans* PlexinA, PLX-1, interacts with transmembrane semaphorins and regulates epidermal morphogenesis. *Development*, *129*(9), 2053 LP – 2063. http://dev.biologists.org/content/129/9/2053.abstract

Gabel, C. V., Antoine, F., Chuang, C.-F., Samuel, A. D. T., & Chang, C. (2008). Distinct cellular and molecular mechanisms mediate initial axon development and adult-stage axon regeneration in C. elegans. *Development*, *135*(6), 1129–1136. https://doi.org/10.1242/dev.013995

Gabel, C. V., Gabel, H., Pavlichin, D., Kao, A., Clark, D. A., & Samuel, A. D. T. (2007). Neural Circuits Mediate Electrosensory Behavior in *Caenorhabditis elegans*. *The Journal of Neuroscience*, *27*(28), 7586–7596. https://doi.org/10.1523/JNEUROSCI.0775-07.2007

Gattass, R. R., Cerami, L. R., & Mazur, E. (2006). Micromachining of bulk glass with bursts of femtosecond laser pulses at variable repetition rates. *Optics Express*, *14*(12), 5279–5284. https://doi.org/10.1364/OE.14.005279

Gherardi, E., Love, C., Esnouf, R., & Jones, E. Y. (2004). The sema domain. *Current Opinions in Structural Biology*, *14*(6), 669–678. https://doi.org/10.1016/j.sbi.2004.10.010.

Ghosh, S., & Hui, S. P. (2018). Axonal regeneration in zebrafish spinal cord. *Regeneration*, *5*(1). https://doi.org/10.1002/reg2.99

Ghosh-Roy, A., & Chisholm, A. D. (2010). *Caenorhabditis elegans*: a new model organism for studies of axon regeneration. *Developmental Dynamics: An Official Publication of the American Association of Anatomists*, *239*(5), 1460–1464. https://doi.org/10.1002/dvdy.22253

Ghosh-Roy, A., Wu, Z., Goncharov, A., Jin, Y., & Chisholm, A. D. (2010). Calcium and cyclic AMP promote axonal regeneration in *Caenorhabditis elegans* and require DLK-1 kinase. *Journal of Neuroscience*, *30*(9). https://doi.org/10.1523/JNEUROSCI.5464-09.2010

Gibalov, V. I., & Pietsch, G. J. (2000). Development of dielectric barrier discharges in gas gaps and on surfaces. *Journal of Physics D: Applied Physics*, *33*(20). https://doi.org/10.1088/0022-3727/33/20/315

Giger, R. J., Hollis 2nd, E. R., & Tuszynski, M. H. (2010). Guidance molecules in axon regeneration. *Cold Spring Harbor Perspectives in Biology*, *2*(7), a001867–a001867. https://doi.org/10.1101/cshperspect.a001867

Ginzburg, V. E., Roy, P. J., & Culotti, J. G. (2002). Semaphorin 1a and semaphorin 1b are required for correct epidermal cell positioning and adhesion during morphogenesis in C. elegans. *Development*, *129*(9), 2065 LP – 2078. http://dev.biologists.org/content/129/9/2065.abstract

Girard, P. M., Arbabian, A., Fleury, M., Bauville, G., Puech, V., Dutreix, M., & Sousa, J. S. (2016). Synergistic Effect of H2O2 and NO2 in Cell Death Induced by Cold Atmospheric He Plasma. *Scientific Reports*, *6*. https://doi.org/10.1038/srep29098

Golkowski, M., Golkowski, C., Leszczynski, J., Plimpton, S. R., Maslowski, P., Foltynowicz, A., Ye, J., & McCollister, B. (2012). Hydrogen-peroxide-enhanced nonthermal plasma effluent for biomedical applications. *IEEE Transactions on Plasma Science*, *40*(8). https://doi.org/10.1109/TPS.2012.2200910

Goodman, C. S., Kolodkin, A. L., Luo, Y., Püschel, A. W., & Raper, J. A. (1999). Unified Nomenclature for the Semaphorins/Collapsins. *Cell*, *97*(5), 551–552. https://doi.org/10.1016/S0092-8674(00)80766-7

Gorbanev, Y., Golda, J., Schulz-von der Gathen, V., & Bogaerts, A. (2019). Applications of the COST Plasma Jet: More than a Reference Standard. In *Plasma* (Vol. 2, Issue 3). https://doi.org/10.3390/plasma2030023

Govaert, M., Smet, C., Verheyen, D., Walsh, J. L., & Van Impe, J. F. M. (2019). Combined Effect of Cold Atmospheric Plasma and Hydrogen Peroxide Treatment on Mature Listeria monocytogenes and Salmonella Typhimurium Biofilms. *Frontiers in Microbiology*, *10*. https://doi.org/10.3389/fmicb.2019.02674

Gray, J. M., Hill, J. J., & Bargmann, C. I. (2005). A circuit for navigation in *Caenorhabditis elegans*. *Proceedings of the National Academy of Sciences*, *102*(9), 3184–3191. https://doi.org/10.1073/pnas.0409009101

Gu, C., Rodriguez, E. R., Reimert, D. V., Shu, T., Fritzsch, B., Richards, L. J., ... & Ginty, D. D. (2003). Neuropilin-1 conveys semaphorin and VEGF signaling during neural and cardiovascular development. Developmental cell, 5(1), 45-57.

Guo, L., Xu, R., Gou, L., Liu, Z., Zhao, Y., Liu, D., Zhang, L., Chen, H., & Kong, M. G. (2018). Mechanism of virus inactivation by cold atmospheric-pressure plasma and plasmaactivated water. *Applied and Environmental Microbiology*, *84*(17). https://doi.org/10.1128/AEM.00726-18

Gurrapu, S., & Tamagnone, L. (2016). Transmembrane semaphorins: Multimodal signaling cues in development and cancer. *Cell Adhesion & Migration*, *10*(6), 675. https://doi.org/10.1080/19336918.2016.1197479

Harreguy, M. B., Marfil, V., Grooms, N. W. F., Gabel, C. V., Chung, S. H., & Haspel, G. (2020). Ytterbium-doped fibre femtosecond laser offers robust operation with deep and precise microsurgery of *C. elegans* neurons. *Scientific Reports*, *10*(1), 1–7. https://doi.org/10.1038/s41598-020-61479-0

Harreguy, M. B., Tanvir, Z., Shah, E., Simprevil, B., Tran, T. S., & Haspel, G. (2022). Semaphorin signaling restricts neuronal regeneration in C. elegans. *Frontiers in Cell and Developmental Biology*, *10*. https://doi.org/10.3389/fcell.2022.814160

Harreguy, M. B., Tran, T. S., & Haspel, G. (2021). Neuronal microsurgery with an Yb-doped fiber femtosecond laser. In *C. elegans Methods and Applications.* (3rd ed.). Springer Nature. https://doi.org/10.1007/978-1-0716-2180-6_17

Hashimoto, M., Ino, H., Koda, M., Murakami, M., Yoshinaga, K., Yamazaki, M., & Moriya, H. (2004). Regulation of semaphorin 3A expression in neurons of the rat spinal cord and cerebral cortex after transection injury. *Acta Neuropathologica*, *107*(3), 250–256. https://doi.org/10.1007/s00401-003-0805-z

Haspel, G., Deng, L., Harreguy, M. B., & Tanvir, Z. (2020). *Elegantly* (P. J. Whelan & S. A. B. T.-T. N. C. of M. Sharples, Eds.; pp. 3–29). Academic Press. https://doi.org/https://doi.org/10.1016/B978-0-12-816477-8.00001-6

Haspel, G., & O'Donovan, M. J. (2011). A Perimotor Framework Reveals Functional Segmentation in the Motoneuronal Network Controlling Locomotion in *Caenorhabditis elegans*. *The Journal of Neuroscience*, *31*(41), 14611–14623. https://doi.org/10.1523/JNEUROSCI.2186-11.2011

Haspel, G., & O'Donovan, M. J. (2012). A connectivity model for the locomotor network of *Caenorhabditis elegans*. *Worm*, *1*(2), 125–128. https://doi.org/10.4161/worm.19392

Haspel, G., O'Donovan, M. J., & Hart, A. C. (2010). Motoneurons Dedicated to Either Forward or Backward Locomotion in the Nematode *Caenorhabditis elegans*. *The Journal of Neuroscience*, *30*(33), 11151–11156. https://doi.org/10.1523/JNEUROSCI.2244-10.2010

Haspel, G., Severi, K. E., Fauci, L. J., Cohen, N., Tytell, E. D., & Morgan, J. R. (2021). Resilience of neural networks for locomotion. *The Journal of Physiology*, *599*(16), 3825–3840. https://doi.org/10.1113/JP279214

He, Z., & Jin, Y. (2016). Intrinsic Control of Axon Regeneration. *Neuron*, *90*(3), 437–451. https://doi.org/10.1016/j.neuron.2016.04.022

He, Z., & Tessier-Lavigne, M. (1997). Neuropilin Is a Receptor for the Axonal Chemorepellent Semaphorin III. *Cell*, *90*(4), 739–751. https://doi.org/10.1016/S0092-8674(00)80534-6

Herndon, L. A., Wolkow, C., & Hall, D. H. (2018). WormAtlas Aging Handbook - Introduction to Aging in C. elegans. *WormAtlas*. https://doi.org/10.3908/wormatlas.8.4

Hilton, B. J., & Bradke, F. (2017). Can injured adult CNS axons regenerate by recapitulating development? *Development (Cambridge, England)*, *144*(19), 3417–3429. https://doi.org/10.1242/dev.148312

Ho, J., Tumkaya, T., Aryal, S., Choi, H., & Claridge-Chang, A. (2019). Moving beyond P values: data analysis with estimation graphics. In *Nature Methods*. https://doi.org/10.1038/s41592-019-0470-3

Hobson, R. J., Yook, K. J., & Jorgensen, E. M. (2017). *Chapter 06 - Genetics of Neurotransmitter Release in Caenorhabditis elegans*. https://doi.org/10.1016/B978-0-12-809633-8.06787-X

Huebner, E. A., & Strittmatter, S. M. (2009). Axon regeneration in the peripheral and central nervous systems. *Results and Problems in Cell Differentiation*, *48*, 339–351. https://doi.org/10.1007/400_2009_19

Hung, R.-J., & Terman, J. R. (2011). Extracellular inhibitors, repellents, and semaphorin/plexin/MICAL-mediated actin filament disassembly. *Cytoskeleton*, n/a-n/a. https://doi.org/10.1002/cm.20527

Husson, S. J., Gottschalk, A., & Leifer, A. M. (2013). Optogenetic manipulation of neural activity in C. elegans: from synapse to circuits and behaviour. *Biology of the Cell*, *105*(6), 235–250. https://doi.org/10.1111/BOC.201200069

Ikegami, R., Simokat, K., Zheng, H., Brown, L., Garriga, G., Hardin, J., & Culotti, J. (2012). Semaphorin and Eph receptor signaling guide a series of cell movements for ventral enclosure in C. elegans. *Current Biology: CB*, *22*(1), 1–11. https://doi.org/10.1016/j.cub.2011.12.009

Ikegami, R., Zheng, H., Ong, S.-H., & Culotti, J. (2004). Integration of semaphorin-2A/MAB-20, ephrin-4, and UNC-129 TGF-beta signaling pathways regulates sorting of distinct sensory rays in C. elegans. *Developmental Cell*, *6*(3), 383–395. https://doi.org/10.1016/s1534-5807(04)00057-7

Iwanir, S., Ruach, R., Itskovits, E., Pritz, C. O., Bokman, E., & Zaslaver, A. (2019). Irrational behavior in *C. elegans* arises from asymmetric modulatory effects within single sensory neurons. *Nature Communications*, *10*(1), 3202. https://doi.org/10.1038/s41467-019-11163-3

Javer, A., Ripoll-Sánchez, L., & Brown, A. E. X. (2018). Powerful and interpretable behavioural features for quantitative phenotyping of *Caenorhabditis elegans*. *Philosophical Transactions of the Royal Society of London. Series B, Biological Sciences*, *373*(1758), 20170375. https://doi.org/10.1098/rstb.2017.0375

Jongbloets, B. C., & Jeroen Pasterkamp, R. (2014). Semaphorin signalling during development. *Development (Cambridge)*, *141*(17). https://doi.org/10.1242/dev.105544

Joshi, S. G., Cooper, M., Yost, A., Paff, M., Ercan, U. K., Fridman, G., Friedman, G., Fridman, A., & Brooks, A. D. (2011). Nonthermal dielectric-barrier discharge plasma-induced inactivation involves oxidative DNA damage and membrane lipid peroxidation in Escherichia coli. *Antimicrobial Agents and Chemotherapy*, *55*(3). https://doi.org/10.1128/AAC.01002-10

Junqueira Alves, C., Yotoko, K., Zou, H., & Friedel, R. H. (2019). Origin and evolution of plexins, semaphorins, and Met receptor tyrosine kinases. *Scientific Reports 2019 9:1*, *9*(1), 1–14. https://doi.org/10.1038/s41598-019-38512-y

Kahnert, A., Seiler, P., Stein, M., Aze, B., McDonnell, G., & Kaufmann, S. H. E. (2005). Decontamination with vaporized hydrogen peroxide is effective against Mycobacterium tuberculosis. *Letters in Applied Microbiology*, *40*(6). https://doi.org/10.1111/j.1472-765X.2005.01683.x

Kaletta, T., & Hengartner, M. O. (2006). Finding function in novel targets: *C. elegans* as a model organism. *Nature Reviews Drug Discovery*, *5*(5), 387–399. https://doi.org/10.1038/nrd2031

Kaneko, S., Iwanami, A., Nakamura, M., Kishino, A., Kikuchi, K., Shibata, S., Okano, H. J., Ikegami, T., Moriya, A., Konishi, O., Nakayama, C., Kumagai, K., Kimura, T., Sato, Y., Goshima, Y., Taniguchi, M., Ito, M., He, Z., Toyama, Y., & Okano, H. (2006). A selective Sema3A inhibitor enhances regenerative responses and functional recovery of the injured spinal cord. *Nature Medicine 2006 12:12*, *12*(12), 1380–1389. https://doi.org/10.1038/nm1505

Kang, H., & Lichtman, J. W. (2013). Motor axon regeneration and muscle reinnervation in young adult and aged animals. *Journal of Neuroscience*, *33*(50). https://doi.org/10.1523/JNEUROSCI.4067-13.2013

Khaitin, A. (2021). Calcium in Neuronal and Glial Response to Axotomy. *International Journal of Molecular Sciences*, *22*(24). https://doi.org/10.3390/IJMS222413344

Kikuchi, K., Kishino, A., Konishi, O., Kumagai, K., Hosotani, N., Saji, I., Nakayama, C., & Kimura, T. (2003). In Vitro and in Vivo Characterization of a Novel Semaphorin 3A Inhibitor, SM-216289 or Xanthofulvin. *Journal of Biological Chemistry*, *278*(44), 42985–42991. https://doi.org/10.1074/jbc.M302395200

Kim, D.-G., Jung, S., & Lee, S. (2018). Flexible Electronics Technologies for the Fabrication of Surface Dielectric Barrier Discharge Devices. *Clinical Plasma Medicine*, *9*. https://doi.org/10.1016/j.cpme.2017.12.008

Kimble, J., & Hirsh, D. (1979). The postembryonic cell lineages of the hermaphrodite and male gonads in *Caenorhabditis elegans*. *Developmental Biology*, *70*(2), 396–417. https://doi.org/10.1016/0012-1606(79)90035-6

Kolodkin, A. L., Levengood, D. V, Rowe, E. G., Tai, Y.-T., Giger, R. J., & Ginty, D. D. (1997). Neuropilin Is a Semaphorin III Receptor. *Cell*, *90*(4), 753–762. https://doi.org/10.1016/S0092-8674(00)80535-8

Kolodkin, A. L., Matthes, D. J., & Goodman, C. S. (1993). The semaphorin genes encode a family of transmembrane and secreted growth cone guidance molecules. *Cell*, *75*(7), 1389–1399. https://doi.org/10.1016/0092-8674(93)90625-Z

Kolodkin, A. L., Matthes, D. J., O'Connor, T. P., Patel, N. H., Admon, A., Bentley, D., & Goodman, C. S. (1992). Fasciclin IV: Sequence, expression, and function during growth cone guidance in the grasshopper embryo. *Neuron*, *9*(5), 831–845. https://doi.org/10.1016/0896-6273(92)90237-8

Kolodkin, A., & Tessier-Lavigne, M. (2011). Mechanisms and molecules of neuronal wiring: a primer. *Cold Spring Harbor Perspectives in Biology*, *3*(6), 1–14. https://doi.org/10.1101/CSHPERSPECT.A001727

Koropouli, E., & Kolodkin, A. L. (2014). Semaphorins and the dynamic regulation of synapse assembly, refinement, and function. *Current Opinion in Neurobiology*, *27*, 1–7. https://doi.org/10.1016/J.CONB.2014.02.005

Kovačević, V. V., Dojčinović, B. P., Jović, M., Roglić, G. M., Obradović, B. M., & Kuraica, M. M. (2017). Measurement of reactive species generated by dielectric barrier discharge in direct contact with water in different atmospheres. *Journal of Physics D: Applied Physics*, *50*(15). https://doi.org/10.1088/1361-6463/aa5fde

Krebs, M. C., Bécasse, P., Verjat, D., & Darbord, J. C. (1998). Gas-plasma sterilization: Relative efficacy of the hydrogen peroxide phase compared with that of the plasma phase. *International Journal of Pharmaceutics*, *160*(1). https://doi.org/10.1016/S0378-5173(97)00296-2

Kruger, R. P., Aurandt, J., & Guan, K.-L. (2005). Semaphorins command cells to move. *Nature Reviews Molecular Cell Biology*, *6*(10), 789–800. https://doi.org/10.1038/nrm1740

Lai, C.-H., Chou, C.-Y., Ch'ang, L.-Y., Liu, C.-S., & Lin, W. (2000). Identification of Novel Human Genes Evolutionarily Conserved in *Caenorhabditis elegans* by Comparative Proteomics. *Genome Research*, *10*(5), 703–713. https://doi.org/10.1101/gr.10.5.703

Laroussi, M. (2002). Nonthermal decontamination of biological media by atmospheric-pressure plasmas: Review, analysis, and prospects. In *IEEE Transactions on Plasma Science* (Vol. 30, Issue 4 I). https://doi.org/10.1109/TPS.2002.804220

Laroussi, M. (2005). Low temperature plasma-based sterilization: Overview and state-of-the-art. In *Plasma Processes and Polymers* (Vol. 2, Issue 5). https://doi.org/10.1002/ppap.200400078

Laroussi, M., & Akan, T. (2007). Arc-free atmospheric pressure cold plasma jets: A review. In *Plasma Processes and Polymers* (Vol. 4, Issue 9). https://doi.org/10.1002/ppap.200700066

Li, W., Feng, Z., Sternberg, P. W., & Shawn Xu, X. Z. (2006). A *C. elegans* stretch receptor neuron revealed by a mechanosensitive TRP channel homologue. *Nature*, *440*(7084), 684–687. https://doi.org/10.1038/nature04538

Limoni, G. (2021). Modelling and Refining Neuronal Circuits with Guidance Cues: Involvement of Semaphorins. *International Journal of Molecular Sciences*, *22*(11). https://doi.org/10.3390/IJMS22116111

Limpert, J., Schreiber, T., Clausnitzer, T., Zöllner, K., Fuchs, H.-J., Kley, E.-B., Zellmer, H., & Tünnermann, A. (2002). High-power femtosecond {Yb}-doped fiber amplifier. *Optics Express*, *10*(14), 628. https://doi.org/10.1364/OE.10.000628

Liu, J. M. (1982). Simple technique for measurements of pulsed Gaussian-beam spot sizes. *Optics Letters*, *7*(5), 196. https://doi.org/10.1364/OL.7.000196

Liu, Z., Fujii, T., Nukazuka, A., Kurokawa, R., Suzuki, M., Fujisawa, H., & Takagi, S. (2005). *C. elegans* PlexinA PLX-1 mediates a cell contact-dependent stop signal in vulval precursor cells. *Developmental Biology*, *282*(1), 138–151. https://doi.org/10.1016/j.ydbio.2005.03.002

Lobato, R. D. (2008). Historical vignette of Cajal's work "Degeneration and regeneration of the nervous system" with a reflection of the author. *Neurocirugía*, *19*(5), 456–468. https://doi.org/10.1016/S1130-1473(08)70215-X

Lu, X., Naidis, G. V., Laroussi, M., Reuter, S., Graves, D. B., & Ostrikov, K. (2016). Reactive species in non-equilibrium atmospheric-pressure plasmas: Generation, transport, and biological effects. In *Physics Reports* (Vol. 630). https://doi.org/10.1016/j.physrep.2016.03.003

Lukes, P., Dolezalova, E., Sisrova, I., & Clupek, M. (2014). Aqueous-phase chemistry and bactericidal effects from an air discharge plasma in contact with water: Evidence for the formation of peroxynitrite through a pseudo-second-order post-discharge reaction of H2O 2 and HNO2. *Plasma Sources Science and Technology*, *23*(1). https://doi.org/10.1088/0963-0252/23/1/015019

Luo, Y., Raible, D., & Raper, J. A. (1993). Collapsin: A protein in brain that induces the collapse and paralysis of neuronal growth cones. *Cell*, *75*(2), 217–227. https://doi.org/10.1016/0092-8674(93)80064-L

Lyons, L. C., & Hecht, R. M. (1997). Acute ethanol exposure induces nondisjunction of the X chromosome during spermatogenesis. *Worm Breeders Gazette*, *14*, 52.

Manevich, Y., Held, K. D., & Biaglow, J. E. (1997). Coumarin-3-carboxylic acid as a detector for hydroxyl radicals generated chemically and by gamma radiation. *Radiation Research*, *148*(6). https://doi.org/10.2307/3579734

Masuda, T., & Taniguchi, M. (2016). Contribution of semaphorins to the formation of the peripheral nervous system in higher vertebrates. In *Cell Adhesion and Migration* (Vol. 10, Issue 6). https://doi.org/10.1080/19336918.2016.1243644

McIntire, S. L., Jorgensen, E., Kaplan, J., & Horvitz, H. R. (1993). The GABAergic nervous system of *Caenorhabditis elegans*. *Nature*, *364*(6435), 337–341. https://doi.org/10.1038/364337a0

Mecollari, V., Nieuwenhuis, B., & Verhaagen, J. (2014). A perspective on the role of class III semaphorin signaling in central nervous system trauma. *Frontiers in Cellular Neuroscience*, *8*. https://doi.org/10.3389/fncel.2014.00328

Melentijevic, I., Toth, M. L., Arnold, M. L., Guasp, R. J., Harinath, G., Nguyen, K. C., Taub, D., Parker, J. A., Neri, C., Gabel, C. V, Hall, D. H., & Driscoll, M. (2017). *C. elegans* neurons jettison protein aggregates and mitochondria under neurotoxic stress. *Nature*, *542*(7641), 367–371. https://doi.org/10.1038/nature21362

Mizumoto, K., & Shen, K. (2013). Interaxonal interaction defines tiled presynaptic innervation in C. elegans. *Neuron*, *77*(4), 655–666. https://doi.org/10.1016/j.neuron.2012.12.031

Mlechkovich, G., Peng, S.-S., Shacham, V., Martinez, E., Gokhman, I., Minis, A., Tran, T. S., & Yaron, A. (2014). Distinct cytoplasmic domains in Plexin-A4 mediate diverse responses to semaphorin 3A in developing mammalian neurons. *Science Signaling*, *7*(316), ra24. https://doi.org/10.1126/scisignal.2004734

Montolio, M., Messeguer, J., Masip, I., Guijarro, P., Gavin, R., Antonio del Río, J., Messeguer, A., & Soriano, E. (2009). A Semaphorin 3A Inhibitor Blocks Axonal Chemorepulsion and Enhances Axon Regeneration. *Chemistry & Biology*, *16*(7), 691–701. https://doi.org/10.1016/j.chembiol.2009.05.006

Nakamura, F., Tanaka, M., Takahashi, T., Kalb, R. G., & Strittmatter, S. M. (1998). Neuropilin-1 Extracellular Domains Mediate Semaphorin D/III-Induced Growth Cone Collapse. *Neuron*, *21*(5), 1093–1100. https://doi.org/10.1016/S0896-6273(00)80626-1

Nakao, F., Hudson, M. L., Suzuki, M., Peckler, Z., Kurokawa, R., Liu, Z., Gengyo-Ando, K., Nukazuka, A., Fujii, T., Suto, F., Shibata, Y., Shioi, G., Fujisawa, H., Mitani, S., Chisholm, A. D., & Takagi, S. (2007). The PLEXIN PLX-2 and the ephrin EFN-4 have distinct roles in MAB-20/Semaphorin 2A signaling in *Caenorhabditis elegans* morphogenesis. *Genetics*, *176*(3), 1591–1607. https://doi.org/10.1534/genetics.106.067116

Negishi, M., Oinuma, I., & Katoh, H. (2005). Review Plexins: axon guidance and signal transduction. *CMLS, Cell. Mol. Life Sci*, *62*, 1363–1371. https://doi.org/10.1007/s00018-005-5018-2

Neumann, B., Nguyen, K. C. Q., Hall, D. H., Ben-Yakar, A., & Hilliard, M. A. (2011). Axonal regeneration proceeds through specific axonal fusion in transected *C. elegans* neurons. *Developmental Dynamics*, *240*(6), 1365–1372. https://doi.org/10.1002/dvdy.22606

Nukazuka, A., Fujisawa, H., Inada, T., Oda, Y., & Takagi, S. (2008). Semaphorin controls epidermal morphogenesis by stimulating mRNA translation via eIF2α in *Caenorhabditis elegans*. *Genes and Development*, *22*(8). https://doi.org/10.1101/gad.1644008

Ohta, K., Takagi, S., Asou, H., & Fujisawa, H. (1992). Involvement of neuronal cell surface molecule B2 in the formation of retinal plexiform layers. *Neuron*, *9*(1), 151–161. https://doi.org/10.1016/0896-6273(92)90230-B

Oikonomou, G., & Shaham, S. (2011). The Glia of *Caenorhabditis elegans*. *Glia*, *59*(9), 1253–1263. https://doi.org/10.1002/GLIA.21084

Oliphint, P. A., Alieva, N., Foldes, A. E., Tytell, E. D., Lau, B. Y.-B., Pariseau, J. S., Cohen, A. H., & Morgan, J. R. (2010). Regenerated Synapses in Lamprey Spinal Cord Are Sparse and Small Even After Functional Recovery From Injury. *The Journal of Comparative Neurology*, *518*(14), 2854. https://doi.org/10.1002/CNE.22368

Pai, K., Timmons, C., Roehm, K. D., Ngo, A., Narayanan, S. S., Ramachandran, A., Jacob, J. D., Ma, L. M., & Madihally, S. V. (2018). Investigation of the Roles of Plasma Species Generated by Surface Dielectric Barrier Discharge. *Scientific Reports*, *8*(1). https://doi.org/10.1038/s41598-018-35166-0

Pascoe, H. G., Wang, Y., & Zhang, X. (2015). Structural mechanisms of plexin signaling. In *Progress in Biophysics and Molecular Biology* (Vol. 118, Issue 3). https://doi.org/10.1016/j.pbiomolbio.2015.03.006

Pasterkamp, R., Anderson, P., & Verhaagen, J. (2001). Peripheral nerve injury fails to induce growth of lesioned ascending dorsal column axons into spinal cord scar tissue expressing the axon repellent Semaphorin3A. *The European Journal of Neuroscience*, *13*(3), 457–471. https://doi.org/10.1046/J.0953-816X.2000.01398.X

Pasterkamp, R. J. (2012). Getting neural circuits into shape with semaphorins. *Nature Reviews. Neuroscience*, *13*(9), 605–618. https://doi.org/10.1038/nrn3302

Pasterkamp, R. J., & Giger, R. J. (2009). Semaphorin function in neural plasticity and disease. In *Current Opinion in Neurobiology* (Vol. 19, Issue 3, pp. 263–274). Curr Opin Neurobiol. https://doi.org/10.1016/j.conb.2009.06.001

Pasterkamp, R. J., & Verhaagen, J. (2001). Emerging roles for semaphorins in neural regeneration. *Brain Research. Brain Research Reviews*, *35*(1), 36–54.

Pavlovich, M. J., Clark, D. S., & Graves, D. B. (2014). Quantification of air plasma chemistry for surface disinfection. *Plasma Sources Science and Technology*, *23*(6), 065036. https://doi.org/10.1088/0963-0252/23/6/065036

Pons, J., Moreau, E., & Touchard, G. (2005). Asymmetric surface dielectric barrier discharge in air at atmospheric pressure: Electrical properties and induced airflow characteristics. *Journal of Physics D: Applied Physics*, *38*(19). https://doi.org/10.1088/0022-3727/38/19/012

Ramon y Cajal, S. (1930). Degeneration and Regeneration of the Nervous System. *Nature*, *125*(3146), 230–231. https://doi.org/10.1038/125230a0

Refai, O., Rohs, P., Mains, P. E., & Gaudet, J. (2013). Extension of the *Caenorhabditis elegans* pharyngeal M1 neuron axon is regulated by multiple mechanisms. *G3: Genes, Genomes, Genetics*, *3*(11). https://doi.org/10.1534/g3.113.008466

Ribas, V. T., Koch, J. C., Michel, U., Bähr, M., & Lingor, P. (2017). Attenuation of Axonal Degeneration by Calcium Channel Inhibitors Improves Retinal Ganglion Cell Survival and Regeneration After Optic Nerve Crush. *Molecular Neurobiology*, *54*(1), 72–86. https://doi.org/10.1007/S12035-015-9676-2/METRICS

Riccomagno, M., & Kolodkin, A. (2015). Sculpting neural circuits by axon and dendrite pruning. *Annual Review of Cell and Developmental Biology*, *31*, 779–805. https://doi.org/10.1146/ANNUREV-CELLBIO-100913-013038

Riccomagno, M. M., Hurtado, A., Wang, H., MacOpson, J. G. J., Griner, E. M., Betz, A., Brose, N., Kazanietz, M. G., & Kolodkin, A. L. (2012). The RacGAP β2-Chimaerin Selectively Mediates Axonal Pruning in the Hippocampus. *Cell*, *149*(7), 1594–1606. https://doi.org/10.1016/J.CELL.2012.05.018

Rohm, B., Ottemeyer, A., Lohrum, M., & Püschel, A. W. (2000). Plexin/neuropilin complexes mediate repulsion by the axonal guidance signal semaphorin 3A. *Mechanisms of Development*, *93*(1–2), 95–104. https://doi.org/10.1016/S0925-4773(00)00269-0

Roy, P. J., Zheng, H., Warren, C. E., & Culotti, J. G. (2000). mab-20 encodes Semaphorin-2a and is required to prevent ectopic cell contacts during epidermal morphogenesis in *Caenorhabditis elegans*. *Development*, *127*(4), 755–767. https://doi.org/10.1242/DEV.127.4.755

Sakudo, A., Yagyu, Y., & Onodera, T. (2019). Disinfection and sterilization using plasma technology: Fundamentals and future perspectives for biological applications. In *International Journal of Molecular Sciences* (Vol. 20, Issue 20). https://doi.org/10.3390/ijms20205216

Schindelin, J., Arganda-Carreras, I., Frise, E., Kaynig, V., Longair, M., Pietzsch, T., Preibisch, S., Rueden, C., Saalfeld, S., Schmid, B., Tinevez, J. Y., White, D. J., Hartenstein, V., Eliceiri, K., Tomancak, P., & Cardona, A. (2012). Fiji: An open-source platform for biological-image analysis. In *Nature Methods*. https://doi.org/10.1038/nmeth.2019

Schneider, C. A., Rasband, W. S., & Eliceiri, K. W. (2012). NIH Image to ImageJ: 25 years of image analysis. In *Nature Methods*. https://doi.org/10.1038/nmeth.2089

Shen, K., & Cowan, C. (2010). Guidance molecules in synapse formation and plasticity. *Cold Spring Harbor Perspectives in Biology*, *2*(4). https://doi.org/10.1101/CSHPERSPECT.A001842

Shen, N., Datta, D., Schaffer, C. B., LeDuc, P., Ingber, D. E., & Mazur, E. (2005). Ablation of cytoskeletal filaments and mitochondria in live cells using a femtosecond laser nanoscissor. *Mechanics & Chemistry of Biosystems: MCB*, *2*(1), 17–25.

Shirvan, A., Kimron, M., Holdengreber, V., Ziv, I., Ben-Shaul, Y., Melamed, S., Melamed, E., Barzilai, A., & Solomon, A. S. (2002). Anti-semaphorin 3A antibodies rescue retinal ganglion cells from cell death following optic nerve axotomy. *Journal of Biological Chemistry*, *277*(51), 49799–49807.

Spinelli, E. D., McPhail, L. T., Oschipok, L. W., Teh, J., & Tetzlaff, W. (2007). Class A plexin expression in axotomized rubrospinal and facial motoneurons. *Neuroscience*, *144*(4), 1266–1277. https://doi.org/10.1016/J.NEUROSCIENCE.2006.10.057

Stiernagle, T. (2006). Maintenance of C. elegans. *WormBook : The Online Review of C. Elegans Biology*, *1999*, 1–11. https://doi.org/10.1895/wormbook.1.101.1

Stone, M. C., Seebold, D. Y., Shorey, M., Kothe, G. O., & Rolls, M. M. (2022). Dendrite regeneration in the vertebrate spinal cord. *Developmental Biology*, *488*. https://doi.org/10.1016/j.ydbio.2022.05.014

Sulston, J. E., & Horvitz, H. R. (1977). Post-embryonic cell lineages of the nematode, *Caenorhabditis elegans*. *Developmental Biology*, *56*(1), 110–156. https://doi.org/10.1016/0012-1606(77)90158-0

Sulston, J. E., Schierenberg, E., White, J. G., & Thomson, J. N. (1983). The embryonic cell lineage of the nematode *Caenorhabditis elegans*. *Developmental Biology*, *100*(1), 64–119. https://doi.org/10.1016/0012-1606(83)90201-4

Sulston, J. E., & White, J. G. (1980). Regulation and cell autonomy during postembryonic development of *Caenorhabditis elegans*. *Developmental Biology*, *78*(2), 577–597. https://doi.org/https://doi.org/10.1016/0012-1606(80)90353-X

Sun, L., Shay, J., McLoed, M., Roodhouse, K., Chung, S. H., Clark, C. M., Pirri, J. K., Alkema, M. J., & Gabel, C. V. (2014). Neuronal regeneration in *C. elegans* requires subcellular calcium release by ryanodine receptor channels and can be enhanced by optogenetic stimulation. *The Journal of Neuroscience: The Official Journal of the Society for Neuroscience*, *34*(48), 15947–15956. https://doi.org/10.1523/JNEUROSCI.4238-13.2014

Suzuki, M., Nukazuka, A., Kamei, Y., Yuba, S., Oda, Y., & Takagi, S. (2022). Mosaic gene expression analysis of semaphorin-plexin interactions in *Caenorhabditis elegans* using the IR-LEGO single-cell gene induction system. *Development, Growth & Differentiation*, *64*(5), 230–242. https://doi.org/10.1111/DGD.12793

Takagi, S., Tsuji, T., Amagai, T., Takamatsu, T., & Fujisawa, H. (1987). Specific cell surface labels in the visual centers of Xenopus laevis tadpole identified using monoclonal antibodies. *Developmental Biology*, *122*(1), 90–100. https://doi.org/10.1016/0012-1606(87)90335-6

Takahashi, T., Fournier, A., Nakamura, F., Wang, L.-H., Murakami, Y., Kalb, R. G., Fujisawa, H., & Strittmatter, S. M. (1999). Plexin-Neuropilin-1 Complexes Form Functional Semaphorin-3A Receptors. *Cell*, *99*(1), 59–69. https://doi.org/10.1016/S0092-8674(00)80062-8

Takahashi, T., Nakamura, F., Jin, Z., Kalb, R. G., & Strittmatter, S. M. (1998). Semaphorins A and E act as antagonists of neuropilin-1 and agonists of neuropilin-2 receptors. *Nature Neuroscience*, *1*(6), 487–493. https://doi.org/10.1038/2203

Tamagnone, L., Artigiani, S., Chen, H., He, Z., Ming, G. L., Song, H. J., Chedotal, A., Winberg, M. L., Goodman, C. S., Poo, M. M., Tessier-Lavigne, M., & Comoglio, P. M. (1999). Plexins Are a Large Family of Receptors for Transmembrane, Secreted, and GPI-Anchored Semaphorins in Vertebrates. *Cell*, *99*(1), 71–80. https://doi.org/10.1016/S0092-8674(00)80063-X

Teoh, J. S., Wong, M., Vijayaraghavan, T., & Neumann, B. (2018). Bridging the gap: Axonal fusion drives rapid functional recovery of the nervous system. In *Neural Regeneration Research* (Vol. 13, Issue 4). https://doi.org/10.4103/1673-5374.230271

Timmons, L., Court, D. L., & Fire, A. (2001). Ingestion of bacterially expressed dsRNAs can produce specific and potent genetic interference in *Caenorhabditis elegans*. *Gene*, *263*(1–2). https://doi.org/10.1016/S0378-1119(00)00579-5

Tran, T. S., Rubio, M. E., Clem, R. L., Johnson, D., Case, L., Tessier-Lavigne, M., Huganir, R. L., Ginty, D. D., & Kolodkin, A. L. (2009). Secreted semaphorins control spine distribution and morphogenesis in the postnatal CNS. *Nature*, *462*(7276), 1065–1069. https://doi.org/10.1038/nature08628

Traylor, M. J., Pavlovich, M. J., Karim, S., Hait, P., Sakiyama, Y., Clark, D. S., & Graves, D. B. (2011). Long-term antibacterial efficacy of air plasma-activated water. *Journal of Physics D: Applied Physics*, *44*(47). https://doi.org/10.1088/0022-3727/44/47/472001

Tsai, P. S., Blinder, P., Migliori, B. J., Neev, J., Jin, Y., Squier, J. A., & Kleinfeld, D. (2009). Plasma-mediated ablation: an optical tool for submicrometer surgery on neuronal and vascular systems. *Current Opinion in Biotechnology*, *20*(1), 90–99. https://doi.org/10.1016/j.copbio.2009.02.003

Tsalik, E. L., & Hobert, O. (2003). Functional mapping of neurons that control locomotory behavior in *Caenorhabditis elegans*. *Journal of Neurobiology*, *56*(2), 178–197. https://doi.org/10.1002/neu.10245

Ueno, M., Nakamura, Y., Nakagawa, H., Niehaus, J. K., Maezawa, M., Gu, Z., Kumanogoh, A., Takebayashi, H., Lu, Q. R., Takada, M., & Yoshida, Y. (2020). Olig2-Induced Semaphorin Expression Drives Corticospinal Axon Retraction After Spinal Cord Injury. *Cerebral Cortex*, *30*(11), 5702–5716. https://doi.org/10.1093/cercor/bhaa142

Verlackt, C. C. W., Van Boxem, W., & Bogaerts, A. (2018). Transport and accumulation of plasma generated species in aqueous solution. *Physical Chemistry Chemical Physics*, *20*(10). https://doi.org/10.1039/c7cp07593f

Vidal-Gadea, A., Ward, K., Beron, C., Ghorashian, N., Gokce, S., Russell, J., Truong, N., Parikh, A., Gadea, O., Ben-Yakar, A., & Pierce-Shimomura, J. (2015). Magnetosensitive neurons mediate geomagnetic orientation in *Caenorhabditis elegans*. *ELife*, *4*. https://doi.org/10.7554/eLife.07493

Vogel, A., Noack, J., Hüttmann, G., & Paltauf, G. (2005). Mechanisms of Femtosecond Laser Nanosurgery of Cells and Tissues. In *Applied Physics B* (Vol. 81). https://doi.org/10.1007/s00340-005-2036-6

Wang, X., Roy, P. J., Holland, S. J., Zhang, L. W., Culotti, J. G., & Pawson, T. (1999). Multiple ephrins control cell organization in *C. elegans* using kinase-dependent and-independent functions of the VAB-1 Eph receptor. *Cell.ComX Wang, PJ Roy, SJ Holland, LW Zhang, JG Culotti, T PawsonMolecular Cell, 1999•cell. Com*, *4*, 903–913. https://www.cell.com/molecular-cell/pdf/S1097-2765(00)80220-8.pdf

Ward, A., Liu, J., Feng, Z., & Xu, X. Z. S. (2008). Light-sensitive neurons and channels mediate phototaxis in C. elegans. *Nature Neuroscience*, *11*(8), 916–922. https://doi.org/10.1038/nn.2155

Weber, J. T. (2012). Altered Calcium Signaling Following Traumatic Brain Injury. *Frontiers in Pharmacology*, *3*. https://doi.org/10.3389/FPHAR.2012.00060

White, J. G., Southgate, E., Thomson, J. N., & Brenner, S. (1976). The structure of the ventral nerve cord of *Caenorhabditis elegans*. *Philosophical Transactions of the Royal Society of London. B, Biological Sciences*, *275*(938), 327–348. https://doi.org/10.1098/RSTB.1976.0086

White, J. G., Southgate, E., Thomson, J. N., & Brenner, S. (1986). The structure of the nervous system of the nematode *Caenorhabditis elegans*. *Philosophical Transactions of the Royal Society of London. Series B, Biological Sciences*, *314*(1165), 1–340. https://doi.org/10.1098/rstb.1986.0056

Williams, W., Nix, P., & Bastiani, M. (2011). Constructing a Low-budget Laser Axotomy System to Study Axon Regeneration in C. elegans. *Journal of Visualized Experiments*, *57*. https://doi.org/10.3791/3331

Winter, C. C., He, Z., & Jacobi, A. (2022). Axon Regeneration: A Subcellular Extension in Multiple Dimensions. *Cold Spring Harbor Perspectives in Biology*, *14*(3). https://doi.org/10.1101/CSHPERSPECT.A040923

Winter, J., Brandenburg, R., & Weltmann, K. D. (2015). Atmospheric pressure plasma jets: An overview of devices and new directions. *Plasma Sources Science and Technology*, *24*(6). https://doi.org/10.1088/0963-0252/24/6/064001

Witvliet, D., Mulcahy, B., Mitchell, J. K., Meirovitch, Y., Berger, D. R., Wu, Y., Liu, Y., Koh, W. X., Parvathala, R., Holmyard, D., Schalek, R. L., Shavit, N., Chisholm, A. D., Lichtman, J. W., Samuel, A. D. T., & Zhen, M. (2021). Connectomes across development reveal principles of brain maturation. *Nature*, *596*(7871). https://doi.org/10.1038/s41586-021-03778-8

Wolfe, R. L., Stewart, M. H., Liang, S., & McGuire, M. J. (1989). Disinfection of model indicator organisms in a drinking water pilot plant by using PEROXONE. *Applied and Environmental Microbiology*, *55*(9). https://doi.org/10.1128/aem.55.9.2230-2241.1989

Wu, Z., Ghosh-Roy, A., Yanik, M. F., Zhang, J. Z., Jin, Y., & Chisholm, A. D. (2007). *Caenorhabditis elegans* neuronal regeneration is influenced by life stage, ephrin signaling, and synaptic branching. *Proceedings of the National Academy of Sciences of the United States of America*, *104*(38), 15132–15137. https://doi.org/10.1073/pnas.0707001104

Xie, J., Chen, Q., Suresh, P., Roy, S., White, J. F., & Mazzeo, A. D. (2017). Paper-based plasma sanitizers. *Proceedings of the National Academy of Sciences of the United States of America*, *114*(20), 5119–5124. https://doi.org/10.1073/PNAS.1621203114/SUPPL_FILE/PNAS.1621203114.SM05.MP4

Xu, K., Tavernarakis, N., & Driscoll, M. (2001). Necrotic Cell Death in *C. elegans* Requires the Function of Calreticulin and Regulators of Ca 2 Release from the Endoplasmic Reticulum. *Neuron*, *31*, 957–971.

Yamamoto, M., Nishioka, M., & Sadakata, M. (2002). Sterilization by H2O2 droplets under corona discharge. *Journal of Electrostatics*, *55*(2). https://doi.org/10.1016/S0304-3886(01)00195-4

Yanik, M. F., Cinar, H. N. H., Cinar, H. N. H., Chisholm, A. D., Jin, Y., & Ben-Yakar, A. (2004). Functional regeneration after laser axotomy. *Nature*, *432*(7019), 822. https://doi.org/10.1038/432822a https://www.nature.com/articles/432822a#supplementary-information

Yaron, A., Huang, P., Cheng, H., & Tessier-Lavigne, M. (2005). Differential requirement for Plexin-A3 and -A4 in mediating responses of sensory and sympathetic neurons to distinct class 3 Semaphorins. *Neuron*, *45*(4), 513–523. https://doi.org/10.1016/J.NEURON.2005.01.013

Yazdani, U., & Terman, J. R. (2006). The semaphorins. *Genome Biology*, *7*(3), 211. https://doi.org/10.1186/gb-2006-7-3-211

Yemini, E., Lin, A., Nejatbakhsh, A., Varol, E., Sun, R., Mena, G. E., Samuel, A. D. T., Paninski, L., Venkatachalam, V., & Hobert, O. (2021). NeuroPAL: A Multicolor Atlas for Whole-Brain Neuronal Identification in C. elegans. *Cell*, *184*(1), 272-288.e11. https://doi.org/10.1016/j.cell.2020.12.012

Yoshida, Y. (2012). Semaphorin signaling in vertebrate neural circuit assembly. *Frontiers in Molecular Neuroscience*, *5*, 71. https://doi.org/10.3389/fnmol.2012.00071

Yu, H.-H., Araj, H. H., Ralls, S. A., & Kolodkin, A. L. (1998). The Transmembrane Semaphorin Sema I Is Required in Drosophila for Embryonic Motor and CNS Axon Guidance. *Neuron*, *20*(2), 207–220. https://doi.org/10.1016/S0896-6273(00)80450-X

Yu, H.-H., & Kolodkin, A. L. (1999). Semaphorin Signaling. *Neuron*, *22*(1), 11–14. https://doi.org/10.1016/S0896-6273(00)80672-8

Yu, L., Zhou, Y., Cheng, S., & Rao, Y. (2010). Plexin A-Semaphorin-1a Reverse Signaling Regulates Photoreceptor Axon Guidance in Drosophila. *The Journal of Neuroscience*, *30*(36), 12151. https://doi.org/10.1523/JNEUROSCI.1494-10.2010

Zhou, R., Zhang, X., Bi, Z., Zong, Z., Niu, J., Song, Y., Liu, D., & Yang, S. (2015). Inactivation of Escherichia coli cells in aqueous solution by atmospheric-pressure N2, He, air, and O2 microplasmas. *Applied and Environmental Microbiology*, *81*(15). https://doi.org/10.1128/AEM.01287-15

Zhou, X., Wahane, S., Friedl, M.-S., Kluge, M., Friedel, C. C., Avrampou, K., Zachariou, V., Guo, L., Zhang, B., He, X., Friedel, R. H., & Zou, H. (2020). Microglia and macrophages promote corralling, wound compaction and recovery after spinal cord injury via Plexin-B2. *Nature Neuroscience 2020 23:3*, *23*(3), 337–350. https://doi.org/10.1038/s41593-020-0597-7